Power scaling of ultrafast mid-IR source enabled by high-power fiber laser technology

by

Gengji Zhou

B.S., Electronic Science and Technology

Huazhong University of Science and Technology, 2009

M.E., Electronics and Communication Engineering

Peking University, 2013

Dissertation

zur Erlangung des Doktorgrades

an der Fakultät für Mathematik, Informatik und Naturwissenschaften

Fachbereich Physik

der Universität Hamburg

Hamburg, October 2017

Gutachter der Dissertation	Prof. Dr. Franz X. Kärtner Dr. Guoqing Chang
Mitglieder der Prüfungskommission	Prof. Dr. Franz X. Kärtner Dr. Guoqing Chang Prof. Dr. Roman Schnabbel Prof. Dr. Nils Huse Dr. Ingmar Hartl
Vorsitzender des Promotionsausschusses	Prof. Dr. Ludwig Mathey
Datum der Disputation	26.10.2017

Dedicated to my family

Declaration

I hereby declare that this dissertation and the work presented in it are my own and has been generated by me as the result of my own original research. The content of this dissertation has neither been accepted nor graded ‘failed’ in a previous doctoral procedure. Any help that I have received in my research work and the preparation of the thesis itself has been acknowledged.

Gengji Zhou

Hamburg, October 2017

Abstract

Ultrafast laser sources with high repetition-rate (>10 MHz) and tunable in the mid-infrared (IR) wavelength range of 7-18 μm hold promise for many important spectroscopy applications. Currently, these ultrafast mid- to longwavelength-IR sources can most easily be achieved via difference-frequency generation (DFG) between a pump beam and a signal beam. However, current ultrafast mid- to longwavelength-IR sources feature a low average power, which limits their applications. In this thesis, we propose and demonstrate a novel approach to power scaling of DFG-based ultrafast mid-IR laser sources. The essence of this novel approach is the generation of a high-energy signal beam. Both the pump beam and the signal beam are derived from a home-built Yb-fiber laser system that emits 165-fs pulses centered at 1035 nm with 30-MHz repetition rate and 14.5-W average power (corresponding to 483-nJ pulse energy). We employ fiber-optic self-phase modulation (SPM) to broaden the laser spectrum and generate isolated spectral lobes. Filtering the rightmost spectral lobe leads to femtosecond pulses with >10 nJ pulse energy. Tunable between 1.1 – 1.2 μm, this SPM-enabled ultrafast source exhibits ~100 times higher pulse energy than can be obtained from Raman soliton sources in this wavelength range. We use this SPM-enabled source as the signal beam and part of the Yb-fiber laser output as the pump beam. By performing DFG in GaSe crystals, we demonstrate that power scaling of a DFG-based mid-IR source can be efficiently achieved by increasing the signal energy. The resulting mid-IR source is tunable from 7.4 μm to 16.8 μm. Up to 5.04-mW mid-IR pulses centered at 11 μm are achieved. The corresponding pulse energy is 167 pJ, representing nearly one order of magnitude improvement compared with other reported DFG-based mid-IR sources at this wavelength.

Despite of low pulse energy, Raman soliton sources have become a popular choice as the signal source. We carry out a detailed study on the Raman soliton noise. We found that the relative intensity noise of an excitation pulse causes center-wavelength fluctuations of the resulting Raman soliton and then translates into a relative timing jitter (RTJ) between the Raman soliton and the excitation pulse by fiber dispersion. Our experimental results suggest that RTJ can be significantly reduced by minimizing the accumulated fiber dispersion experienced by the Raman soliton using fibers with less dispersion and shorter length.

Zusammenfassung

Ultrakurzpulslaser mit hohen Pulswiederholraten (>10 MHz), die im mittleren bis langem Infrarot (IR)-Bereich von 7 bis 18 μm durchstimmbar sind, sind vielversprechend für spektroskopische Anwendungen. Solche Kurzpuls-Lichtquellen im mittleren .... IR Spektrum werden durch Differenzfrequenzerzeugung (difference-frequency-generation, DFG) zwischen einer Pumpwelle und einer Signal-Strahlung realisiert. Heutige ultrakurze IR-Quellen sind jedoch begrenzt in der niedrigen Durchschnittsleistung und daher nur bedingt anwendbar. Die vorliegende Arbeit zeigt einen neuen Ansatz zur Leistungsskalierung von DFG-basierten ultrakurzen Lasern im IR Spektrum. Im Kern des Forschungsansatzes steht die Erzeugung eines Signalstrahls von hoher Energie. Sowohl der Pumpstrahl als auch der Signalstrahl stammen von einem selbst gebauten Yb-Faser-Lasersystem, das Pulse mit einer Dauer von 165-fs und einer mittleren Wellenlänge von 1035 nm bei einer Pulswiederholrate von 30-MHz und 14.5-W Durchschnittsleistung (entsprechend einer Puls-Energie von 483-nJ) emittiert.

Durch Selbstphasenmodulation in einer optischen Faser wird das Spektrum verbreitert bis ausgeprägte Maxima am Rand des Spektrums ausbilden. Die spektrale Filterung durch einen optischen Tiefpassfilter ermöglicht die Selektion des Maximums im infraroten Bereich und führt zu Laserpulsen mit einer Dauer im femtosekunden Bereich und einer Energie >10 nJ. Abstimmbar zwischen 1.1 – 1.2 μm erzeugt diese auf SPM basierende Lichtquelle ~100 mal höhere Pulsenenergien als in diesem Wellenlängenbereich mit auf Raman Solitonen basierenden Quellen erreicht werden kann. Der spektral gefilterte Puls aus dem SPM verbreiterten Spektrum wird als Signalstrahl genutzt, während ein Teil des Yb-Faser Lasers als Pumpstrahl dient. Durch den DFG Prozess in einem GaSe-Kristall wird gezeigt, dass die Leistungsskalierung einer DFG-basierten IR-Quelle durch Erhöhung der Energie der Signalwelle erreicht werden kann. Das Spektrum kann von 7.4 μm bis 16.8 μm durchgestimmt werden und es werden Pulse mit bis zu 5.04-mW mittlerer Leistung um bei 11 μm Wellenlänge erreicht. Die entsprechende Pulsenergie liegt bei 167 pJ und übertrifft damit bisherige Lichtquellen im mittleren IR-Bereich um nahezu eine Größenordnung.

Trotz niedriger Pulsenergie sind Raman Solitonen eine beliebte Wahl für die Signalwelle. Deshalb wird in der vorliegenden Arbeit eine detaillierte Untersuchung des Rauschens von Raman Solitonen durchgeführt. Dabei stellt sich heraus, dass das relative Intensitätsrauschen eines Anregungsimpulses Fluktutationen der mittleren Wellenlänge im resultierenden Raman Soliton hervorruft und durch die Faserdispersion in relative Ankunftszeitfluktuationen (relative timing jitter, RTJ) zwischen dem Raman Soliton und dem Anregungspuls übersetzt wird. Die Experimente legen nahe, dass der RTJ durch eine Minimierung der akkumulierten Faserdispersion signifikant reduziert werden kann, so wie es bei Raman Solitonen in Fasern geringer Dispersion und kürzerer Länge festgestellt wurde.

Acknowledgement

I wish to express my sincere gratitude to my advisor Prof. Franz X. Kärtner for offering me the great opportunity to pursue my PhD in Germany. Thanks for his continuous support, patience, motivation, interest, mentoring and creation of supporting environment for this work.

Special acknowledgement goes to Dr. Guoqing (Noah) Chang, my supervisor, for his insightful comments and encouragement. His guidance helped me during my whole PhD journey, not only in the scientific research work, but also on living a meaningful life. I would also like to appreciate for his opening supervision, setting a start point, pointing out a direction, and leaving me a great freedom and independence to my research work. My research capability could not be dramatically improved without his free style environment. Last but not least, I wish to thank him for being both a friend and a supervisor.

Many thanks to Ms Christine Berber, our group secretary, for her dedicating work for taking care of me both in working and living in Germany. I also owe big thanks to the IMPRS-UFAST graduate school, its coordinators Ms Anja Bleidorn, Ms Sonia Utermann, and Ms Julia Quante for offering me a great opportunity to exchange knowledge and experience.

During four years of PhD work, it has been a great honor for me to work with many elite researchers all around the world. First of all, I wish to express my appreciation to Dr. Ming Xin for his kind help and professional knowledge on RIN and RTJ measurement. Fruitful results could not be achieved without his assistance. Many other colleagues offered great help on my research projects. Dr. Hung-Wen Chen and Dr. Jinkang Lim provided me with valuable guidance on the 3-GHz laser project. Dr. Tao Chen and Roland Mainz helped on constructing high-power CPA system. Dr. Axel Ruehl, Dr. Peng Li, Vinicius Silva de Oliveira, and Dr. Chenchen Wan offered me a lot of help on low rep-rate oscillator, high-power amplifier development, and DFG based mid-IR source generation and characterization. Dr. Chun Zhou, Dr. Xiaojun Wu, Biaolong Liu, and Dr. Liwei Song loaned me the mid-IR equipment and valuable advice. Fabian Scheiba and Kemal Shafak helped me for German translation and thesis submission guidance. Special acknowledgement goes to Dr. Michaël Hemmer for his constructive suggestion and extensive experience on building high-power laser, and mid-IR generation and detection. My horizon could not be expanded so rapidly without his valuable suggestion. I would also thank the Zapatas—Luis E. Zapata and Kelly Zapata, for their kind help on both research discussion and colorful life. I wish to thank all members in our group for the nice and friendly working environment.

In the end, I am grateful to my Master Supervisor Prof. Zhigang Zhang for his systematic guidance and kind recommendation. I would also deeply appreciate Ms. Lan Jin for her wholehearted support at the beginning of my PhD journey. I would not start my PhD without her and I wish her a happy life ever after. I would also like to thank my parents, my two elder sisters, and my brother in-law for believing in me and supporting me as always. I would not have made this far without your support. Love you all now and always.

Publication List

Journal publications

[1] **G. Zhou**, F. X. Kaertner, and G. Chang, “High-power, widely tunable mid-IR pulses enabled by SESS fiber approach,” manuscript in preparation.

[2] **G. Zhou**, M. Xin, F. X. Kaertner, and G. Chang, “Timing jitter of Raman solitons,” *Opt. Lett.* ***40(21)****, 5105–5108 (2015)*.

Conference Proceedings

[1] **G. Zhou**, M. Xin, Y. Liu, F. X. Kärtner, and G. Chang, " SPM-enabled fiber laser source beyond 1.2 μm," in *Advanced Solid State Lasers:2016*, OSA Technical Digest (online) (Optical Society of America, 2016), paper ATh1A.4.

[2] Y. Hua, W. Liu, M. Hemmer, L. E. Zapata, **G. Zhou**, D. N. Schimpf, T. Eidam, J. Limpert, A. Tünnermann, F. X. Kaertner, and G. Chang, "87-W, 1018-nm Yb-fiber ultrafast seeding source for cryogenic Yb:YLF amplifier," in *CLEO:2016*, OSA Technical Digest (online) (Optical Society of America, 2016), paper SM4Q.5.

[3] **G. Zhou**, M. Xin, F. Kaernter, and G. Chang, “Timing jitter optimization of Raman solitons," in *Ultrafast Optics 2015*, paper UFO0055.

[4] **G. Zhou**, M. Xin, F. Kaernter, and G. Chang, "Relative Timing Jitter of Raman Soliotns and its Effect on Nonlinear Wavelength Conversion," in *CLEO: 2015*, OSA Technical Digest (online) (Optical Society of America, 2015), paper SF2D.4.

[5] **G. Zhou**, M. Xin, W. Liu, F. X. Kärtner, and G. Chang, "Relative intensity noise and timing jitter of Raman soliotns," in *Advanced Solid State Lasers: 2014*, OSA Technical Digest (online) (Optical Society of America, 2014), paper AM5A.36.

[6] **G. Zhou**, W. Liu, J. Lim, H. Chen, F. Kärtner, and G. Chang, "Relative intensity noise of Raman solitons," in *6th EPS-QEOD EUROPHOTON CONFERENCE: 2014*, paper ThC-T2-O-03.

[7] W. Liu, **G. Zhou**, J. Lim, H. Chen, F. Kärtner, and G. Chang, "Relative intensity noise of Raman solitons: which one is more noisy?," in *CLEO: 2014*, OSA Technical Digest (online) (Optical Society of America, 2014), paper SM4N.7.

Contents

List of figures

List of tables

List of abbreviations

AC	auto-correlation
AR	anti-reflection
BBO	beta barium borate
BD	Beam dumping
BOC	balanced optical cross-correlator
BPD	balanced photodetector
CCD	charge-coupled device
CEP	carrier-envelope phase
CPA	chirped-pulse amplification
DE	delay element
DFG	difference-frequency generation
DM	dichroic mirror
EUV	extreme ultraviolet
FTL	Fourier transform-limited
FWHM	full width at half maximum
GDD	group-delay dispersion
GNLSE	generalized nonlinear Schrödinger equation
GVD	group-velocity dispersion
HWP	half-wave plate
ISO	Isolator
LMA	large-mode-area
MFD	mode-field diameter
mid-R/MIR	mid-infrared
MM	multi-mode
NPE	nonlinear polarization evolution
OPO	Optical parametric oscillator
OSA	optical spectrum analyzer
PBS	polarization beam splitter
PCF	photonic crystal fiber
PER	polarization extinction ratio

PM	polarization-maintaining
QWP	quarter-wave plate
RIN	relative intensity noise
RS	Raman soliton
RTJ	relative timing jitter
SESS	SPM-enabled spectral selection
SFG	sum-frequency generation
SNR	signal-to-noise ratio
SPM	self-phase modulation
SRS	stimulated Raman scattering
SSFS	soliton self-frequency shift
TEC	Temperature Controller
TOD	third-order dispersion
TPA	two-photon absorption
UV	ultraviolet
WDM	wavelength division multiplexer
Yb	ytterbium
ZDW	zero-dispersion wavelength

Chapter 1

Introduction

1.1 Ultrafast mid-IR laser source and frequency comb

Ultrafast lasers that generate femtosecond pulses have revolutionized many aspects of both fundamental research and industrial applications. Limited by laser gain medium, ultrafast lasers typically operate in 0.6–2 μm of visible and near-infrared wavelength range. However, many scientific and industrial applications require the femtosecond pulses in the mid-infrared (mid-IR) wavelength range (2–20 μm) [1, 2]. Because a large number of molecules undergo strong vibration transitions in the mid-IR region (see Fig. 1.1), mid-IR spectroscopy becomes a reliable method to detect and distinguish these molecules (including isotopes). The wavelength range of 6.6–20 μm is known as the molecular 'fingerprint' region, where many molecules possess unique absorption lines. It is noteworthy that the mid-IR spectral region contains two important windows, i.e., 3–5 μm and 8–13 μm, where the Earth atmosphere is relatively transparent. Ultrafast mid-IR laser sources working in this window become an indispensable tool for atmospheric remote sensing, including to detect small traces of environmental and toxic vapors [2].

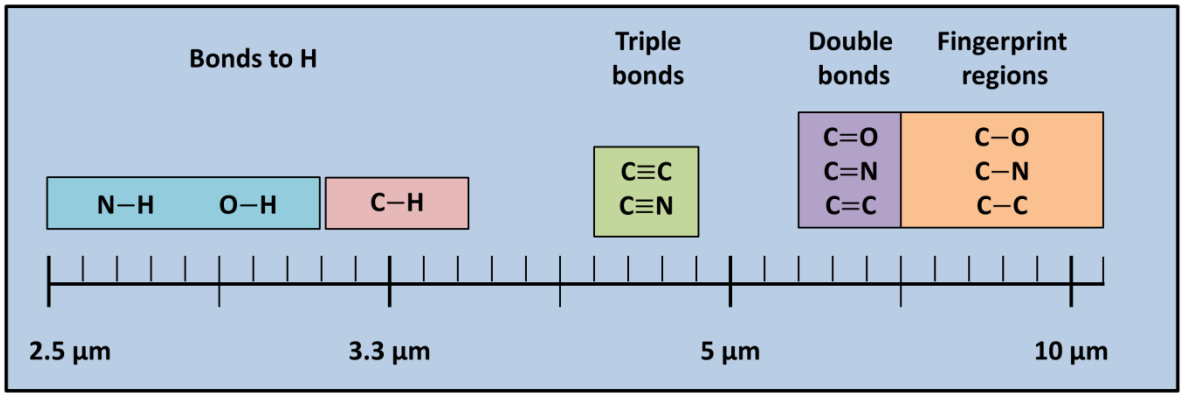

Fig. 1. 1. Molecular vibration transitions in the mid-IR region for different chemical bonds.

Ultrafast mid-IR spectroscopy is also a powerful tool to investigate novel quantum materials [3]. In the past decade, the most prominent quantum materials in condensed matter physics are graphene, topological insulator, iron-based superconductor, etc. They continue to form the frontier of current condensed matter physics. One of the most powerful techniques to investigate the electronic and optical properties of these quantum materials is ultrafast laser spectroscopy. Since the intrinsic dynamics of a condensed matter (with the atomic distance at the order of 1 angstrom) is characteristically at the scale of femtosecond/picosecond, ultrafast spectroscopy is the only practical way to time-resolve this evolution process [3]. There are various quantum phases along this dynamical process since photons can interact with condensed matters in all four known degrees of freedom: charge, lattice, spin, and orbital. According to the existed study on topological insulator, the bandgap and characteristic band structure of three-dimensional topological insulator are around 100 meV, which corresponds to the photon energy of pulses centered at 5–15 μm. The rapid development of ultrafast mid-IR laser sources will significantly advance the research on novel topological materials.

In the past two decades, the advent of the optical frequency comb undoubtedly becomes the most important advances in ultrafast optics [4]. A passive mode-locked ultrafast laser with a typical repetition rate of 30 MHz -1 GHz is the core part of the traditional optical frequency comb, which produces equally spaced femtosecond pulse sequences in the time domain. If the pulse repetition rate f_R and carrier envelope offset f_{CE} are stabilized, the pulse sequences emerge as frequency lines with the same equal interval in the frequency domain, which is known as optical frequency comb. The interval between adjacent comb line is identical to the repetition frequency f_R, and any comb line can be expressed as $f = N \times f_R + f_{CE}$, where N is a positive integer. An optical frequency comb generally contains hundreds of thousands of stabilized comb lines. Due to the advantages of high precision comb lines, frequency comb has been widely used in applications, such as high precision absolute distance measurement, ultra-low noise microwave extraction, spectroscopy, time-frequency standard transfer, and atomic optical clock. An important potential application of optical frequency comb is detection of certain diseases by spectroscopic analysis of specific type of gases exhaled by the patient. For instance, with the help of enhancement cavity and an optical frequency comb operating at 1.5 μm, Thorpe et al. has realized the spectroscopic analysis of human breath in 30-second measurement. However, due to the small absorption cross-section in the near infrared spectra range for most gas molecules, the sensitivity of this technology can only achieve 0.002% [5]. Fortunately, the gas absorption cross-section in the mid-IR range is three

or four orders of magnitude higher than the one in the near infrared range. Therefore, the detection sensitivity could be dramatically improved by utilizing a laser frequency comb in the mid-IR wavelength range along with an enhancement cavity, constituting a fast, convenient, and accurate disease diagnosis technology.

1.2 Approaches for development of mid-IR laser sources

Due to the absence of proper gain medium in the mid-IR spectral range, ultrafast mid-IR laser sources with the wavelength beyond 3 μm have to be derived from an ultrafast near-IR laser via nonlinear frequency conversion [6]. Usually two methods are utilized to implement an ultrafast mid-IR source: (1) optical parametric oscillator (OPO) pumped by an ultrafast near-IR laser and (2) difference-frequency generation (DFG) between two synchronized pulse trains with different central wavelength.

OPO-based ultrafast mid-IR sources can emit femtosecond pulses with 10s of milli-Watt average power [6]. However, due to the limitation of available crystals, the typical operating wavelength is below 7 μm and the generated mid-IR spectrum has a narrower tuning range compared with the DFG method. Furthermore, the OPO cavity needs to be synchronized with the near-IR pump laser. To obtain an OPO-based mid-IR frequency comb, the pump laser has to be a frequency comb source and the carrier-envelope offset f_{CE} of the generated mid-IR pulses needs to be additional locked.

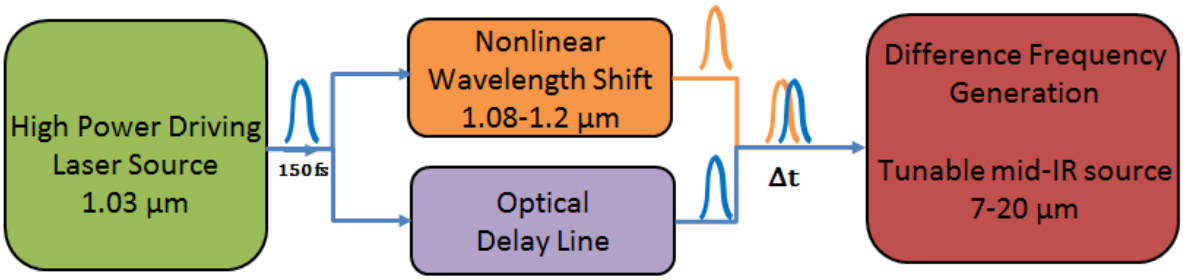

Fig. 1. 2. Schematic of a DFG-based ultrafast mid-IR laser source.

DFG-based ultrafast mid-IR laser sources exhibit much simpler structure without additional resonant cavity, which enormously reduces the complexity of the whole system. As shown in Fig. 1.2, the major component is a high power femtosecond laser. The output pulse trains are

split into two portions. One portion serves as the pump pulses and the other portion is used to generate signal pulses with the center wavelength broadly tunable. The pump and signal pulses are then combined together both spatially and temporally, and superimposed on a nonlinear crystal to generate wavelength tunable mid-IR pulses via DFG. For instance, mid-IR pulses continuously tunable from 6.6 μm to 20 μm can be achieved using DFG between a pump pulse at 1.03 μm and a signal pulse that is tunable from 1.08 μm to 1.22 μm. Normally the signal pulse is derived from the same ultrafast laser that provides the pump pulse. A well-established technique is to use fiber-optic nonlinearities to broaden the optical spectrum of the ultrafast source laser; the newly generated spectral component at the longer wavelength side serves as the signal for DFG. Fiber-optic nonlinearities arise from the third-order susceptibility of the fiber glass and preserve the carrier-envelope offset f_{CE} during the nonlinear spectral broadening. Consequently the signal pulse and the pump pulse share the same f_{CE}, which cancels out during DFG; that is, the f_{CE} of the resulting mid-IR source is automatically set to zero. If the source laser's repetition rate is stabilized, the mid-IR source becomes a mid-IR frequency comb. Indeed, DFG is the only means to implement mid-IR frequency comb covering the whole 'fingerprint' region.

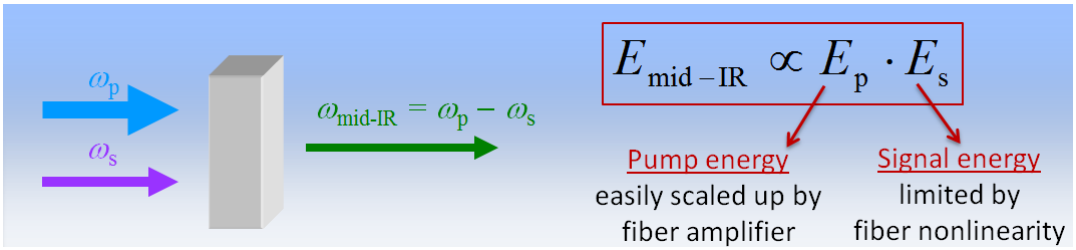

Fig. 1. 3. Ultrafast mid-IR laser source based on DFG between a pump beam and a signal beam. The resulting mid-IR pulse energy is proportional to the pulse energy product between the pump and the signal.

DFG involves mixing of three waves in a nonlinear crystal with non-zero 2nd-order susceptibility (Fig. 1.3). Under the slowly varying amplitude approximation and neglecting the effects such as diffraction, group-velocity mismatch, and group-velocity dispersion (GVD), DFG in a lossless nonlinear crystal can be modeled by the following coupled amplitude steady-state equations (1.1-1.3):

$$\frac{dA_{MIR}(z)}{dz} = i\frac{2\omega_{MIR}d_{eff}}{n_{MIR}c}A_P(z)A_S^*(z)e^{i\Delta kz} \tag{1.1}$$

$$\frac{dA_S(z)}{dz} = i\frac{2\omega_S d_{eff}}{n_S c}A_P(z)A^*_{MIR}(z)e^{i\Delta kz} \tag{1.2}$$

$$\frac{dA_P(z)}{dz} = i\frac{2\omega_P d_{eff}}{n_P c}A_{MIR}(z)A^*_S(z)e^{-i\Delta kz} \tag{1.3}$$

A(z) denotes the propagating pulse envelope and the subscripts refer to pump beam (*P*), signal beam (*S*), and generated mid-IR beam (*MIR*). d_{eff} is the effective nonlinearity. $\Delta k = k_P - k_S - k_{MIR}$ represents the wave-vector mismatch, which is a scalar for the collinear arrangement of the three optical beams. Nonlinear frequency conversion becomes more efficient when the phase-matching condition is satisfied, i.e., $\Delta k = 0$. For the DFG process with simple collinear interaction, the phase-matching condition is equivalent to $n_{MIR}\omega_{MIR} = n_P\omega_P - n_S\omega_S$. The most popular means to achieve phase-matching is to utilize a nonlinear crystal with birefringence and set three optical beams at different polarizations. The refractive index of the corresponding e-wave can be adjusted by tuning the incident angle of the optical beams on the crystal. If at the input only the pump beam and signal beam exist and the pump beam is undepleted, Eq. (1.1-1.3) can be solved analytically leading to the following expression for the mid-IR beam intensity:

$$I_{MIR} = \frac{8\pi^2 d_{eff}^2 L^2 I_S I_P}{\varepsilon_0 c n_{MIR} n_S n_P \lambda_{MIR}^2} sinc^2\left(\frac{|\Delta k|L}{2}\right), \tag{1.4}$$

where *L* is the crystal thickness [7].

1.3 Widely tunable ultrafast signal source enabled by fiber-optic nonlinearities

When a femtosecond pulse propagates in an optical fiber, the light-matter nonlinear interaction gives rise to many nonlinear effects, such as self-phase modulation (SPM), self-steepening, and stimulated Raman scattering (SRS) [8]. Fiber dispersion plays an important role as well. For example, negative GVD provides negative chirp to the pulse while SPM adds positive chirp. The cancellation of negative chirp and positive chirp during pulse propagation results in soliton pulse formation in the fiber.

Soliton was first reported by John Russell who found that the stable water wave traveled over a large distance whereas normal water wave would flatten out quickly [9]. This unique

phenomenon inspired him to carry out a detailed investigation on such a water wave. He found out that the stable wave maintained its shape while traveling a long distance; the speed depends on the size of the wave and the width on the water depth. In 1870s Joseph Boussinesq and Lord Rayleigh published a theoretical treatment to explain the physics behind the solitary wave formation. After efforts of several generations, soliton becomes an intriguing phenomenon in nonlinear fiber optics.

Raman soliton—first discovered in 1986—is associated with Raman scattering effect inside optical fibers [10]. The interplay between intra-pulse Raman scattering and soliton formation results in soliton self-frequency shift (SSFS) [11]; that is, the center wavelength of the resulting Raman soliton redshifts continuously with an increased propagation distance. Meanwhile the Raman soliton maintains its hyperbolic secant profile. SSFS has been widely used to implement wavelength tunable ultrafast sources because it is compatible with currently rapidly developed ultrafast fiber laser. Especially ultrafast Yb-fiber lasers exhibit superior power scalability and electric-optical conversion efficiency. Thanks to the prompt development of fiber technology, all-fiber high-power femtosecond fiber lasers with extremely high stability become possible.

Ultrafast Yb-fiber lasers emit femtosecond pulses with the center wavelength at ~1.03 μm. Standard single-mode fibers exhibit positive GVD and therefore cannot support SSFS that requires negative GVD. In contrast, photonic crystal fibers (PCFs) allow their dispersion flexibly engineered such that SSFS in suitable PCFs pumped by an Yb-fiber laser can lead to a Raman soliton tunable in the wavelength range of 1.05-1.30 μm [12]; a careful optimization of the SSFS process extends the tuning range to cover 1.05-1.70 μm [13]. The resulting Raman soliton source is synchronized and shares the same the f_{CE} with the Yb-fiber laser source. Yb-fiber laser based DFG sources normally employ SSFS to obtain the signal pulses. More specific, the ultrafast Yb-fiber laser output is split into two copies, one copy serving as the pump pulses and the other copy coupled into a PCF to generate wavelength tunable signal pulses. DFG in a nonlinear crystal between the pump pulses and signal pulses result in wavelength tunable mid-IR femtosecond pulses with the f_{CE} passively stabilized.

A combination of an ultrafast fiber laser and fiber-optic Raman soliton source becomes a widely adopted configuration to construct ultrafast mid-IR sources and mid-IR frequency combs [14-20]. To make the full use of the excellent power scalability of Yb-fiber laser technology, PCFs with negative GVD at ~1.03 μm are fabricated to accommodate Raman

soliton. With a much smaller mode-field diameter, these PCFs exhibit nonlinearity about one order of magnitude higher than standard single-mode fibers. Such strong nonlinearity in PCFs limits the pulse energy of the Raman soliton source to <1 nJ; in the wavelength range of 1070-1200 nm, the pulse energies are typically less than 0.2 nJ. SSFS in higher order-mode fibers pumped by Yb-fiber lasers can result in >1 nJ pulse energies; however the generated Raman soliton pulses are propagating in the higher-order mode. Mode converting them back to the fundamental mode—a necessary beam profile for subsequent DFG—is challenging [21, 22].

Among many quantities that characterize a femtosecond source, timing jitter and relative intensity noise (RIN) are of particular importance and determine whether the femtosecond source is "quiet" enough for our DFG-based mid-IR source. Since the amount of SSFS depends on the excitation pulse's energy, the RIN of the excitation pulse causes the Raman soliton's center-wavelength fluctuations, which is then converted to timing jitter by fiber dispersion. Minimizing the relative timing jitter of a Raman soliton with respect to its excitation pulse is of particular importance for realizing a low-noise mid-IR DFG source.

1.4 High power and high repetition-rate ultrafast mid-IR laser sources

The mid-IR wavelength range between 6 and 20 μm, in particular, has been known as the fingerprint region. Spectroscopic information of these vibrational bands reveals the molecular structure and, in turn, identifies the ingredients of the sample under test. In this scenario, a high power, low noise, tunable mid-IR femtosecond source is highly desired from the viewpoint of rapid high-resolution sensing and spectroscopy. High average power can improve the signal-to-noise ratio and shorten measuring time; low noise improves the measurement sensitivity. To implement a frequency comb with proper comb line spacing, the repetition rate of the mid-IR pulse train should be 10s-100s of MHz.

Limited by the damage threshold and relative low optical conversion efficiency in DFG, the average power of DFG-based mid-IR source rapidly decrease with the mid-IR source moving toward longer wavelength. For example, a mid-IR frequency comb tunable in 8–14 μm was obtained by DFG inside a GaSe crystal [18]. The source laser is a 250-MHz Er-fiber laser

that generates both the pump pulses and Raman-soliton-based signal pulses. The resulting mid-IR source outputs 4-mW average power at 8 μm and <1 mW at 10 μm; the output power at 13.6 μm is only 0.11 mW, which corresponds to 0.006 μW per comb line. Another disadvantage of DFG based mid-IR frequency comb is the large intensity noise. According to existed experimental results, the intensity noise of generated mid-IR comb is four orders of magnitude higher than the employed pump and signal sources [18]. In this experiment, the pump pulse has ~2-nJ energy limited by the available Er-fiber laser and the signal pulse has <1-nJ energy limited by the Raman soliton source [18].

Equation (1.4) suggests that the mid-IR beam intensity is proportional to the pump beam intensity. Therefore the average power of the mid-IR source can be increased if a more powerful fiber laser is used to generate the pump pulse. For example, it is quite straightforward to construct an ultrafast Yb-fiber laser with 10s of Watt average power without active cooling. At 10s of MHz repetition rate, such an Yb-fiber laser can produce femtosecond pulses with uJ level pulse energy. One might intuitively speculate that using such uJ-level pulses as the pump for DFG can generate ~100-mW mid-IR pulses at ~10 um. In fact, other limitations arise from the properties of nonlinear crystals. To date, $AgGaSe_2$ (AGSe) and GaSe are the most popular nonlinear crystals that can generate DFG-based ultrafast mid-IR source covering the entire fingerprint region of 6.6-20 um [6, 23]. Unfortunately both AGSe and GaSe have low damage threshold that limits the pulse energy of the pump beam in DFG. Our experimental results show that even for a loosely focused beam with ~150-um spot diameter, 30-MHz 200-fs pulses at 1.03 um with ~200-nJ pulses energy can damage a GaSe crystal.

In the conventional design, the pump pulse and the signal pulse differ in energy (or power) by orders of magnitude. For example, the pump pulse derived from an Yb-fiber laser system may have a pulse energy of >100 nJ while the signal pulse has an energy of ~100 pJ limited by Raman soliton pulse energy. Indeed Eq. (1.4) shows that the mid-IR beam intensity is proportional to the intensity product between the pump beam and the signal beam, implying that energy doubling either the pump pulse or the signal pulse will result in the same mid-IR pulse energy. This immediately suggests that energy scaling a DFG-based mid-IR source by increasing the signal pulse energy rather than increasing the pump pulse energy constitutes a more efficient avenue. In fact, the pump pulse energy has to be kept below a certain value to prevent crystal damage. Therefore increasing the signal pulse energy becomes a powerful and practical solution to achieve high-power mid-IR pulses. Since Raman soliton source exhibit

low pulse energy (e.g., normally <1 nJ in the wavelength range of 1070-1200 nm), new type of energetic fiber-optic source is highly desired. This ultrafast source should emit nearly transform-limited femtosecond pulses featuring low noise and superior energy scalability.

1.5 Structure of the thesis

In Chapter 2 we study the RIN and timing jitter of a Raman soliton. We demonstrate that the RIN of an excitation pulse causes center-wavelength fluctuations of the resulting Raman soliton, which translates by fiber dispersion into relative timing jitter (RTJ) between the Raman soliton and the excitation pulse. The Raman soliton's absolute timing jitter is dominated by the excitation pulse's timing jitter at low frequency and by the RTJ at high frequency. The experimental study reveals that RTJ can be significantly reduced by reducing the accumulated fiber dispersion (e.g., using less dispersive fibers with shorter length) experienced by the Raman soliton.

As we have discussed in section 1.4, high-power mid-IR source replies on power/energy scaling both the pump beam and the signal beam involved in DFG. Therefore a powerful ultrafast laser source is a must. Chapter 3 presents the detailed implementation of a high power Yb-fiber laser system that serves as the driving source, from which both the pump and the signal are derived. Enabled by the chirped-pulse amplification technique, the constructed Yb-fiber laser system operates at 30-MHz repetition rate and emits 165-fs pulses with 14.5-W average power.

In Chapter 4, we demonstrate a new type of fiber-optic ultrafast source, which is derived from the high-power Yb-fiber laser developed in Chapter 3. The laser's output is spectrally broadened largely due to SPM, leading to the formation of well-separated spectral lobes. We then use optical bandpass filters to select the rightmost spectral lobe and generate ~100-fs (nearly transform-limited) pulses. Such an SPM-enabled spectral selection (SESS) in a short large-mode-area fiber allows generation of high-energy and widely tunable femtosecond pulses. In Chapter 4, we investigate the energy scalability of SESS source in the wavelength range of 1200-1300 nm. Up to 16.5-nJ pulses at 1225 nm are obtained, representing two orders of magnitude energy improvement over a Raman soliton source in this wavelength range.

Chapter 5 is dedicated to the development of a DFG-based high-power mid-IR source enabled by the high-power Yb-fiber laser system developed in Chapter 3. The SESS technique presented in Chapter 4 is employed to produce high-energy (up to 20 nJ) signal pulses. The resulting ultrafast mid-IR source can be wavelength tuned from 7.4 um to 17 um. We carefully study the power dependence of the mid-IR source on the pump beam and the signal beam. The experimental results clearly indicate that increasing the signal pulse energy can efficiently improve the power yield of the resulting mid-IR source. Using 2-mm thick GaSe as the DFG crystal, we obtain >5-mW mid-IR pulses at 11 um. The corresponding ~170-pJ pulse energy represents nearly one order of magnitude improvement over current DFG sources at 11 um that employ Raman soliton source as the signal pulse.

Finally Chapter 6 concludes the thesis.

Chapter 2

Relative Intensity Noise and Timing Jitter of Raman Solitons

2.1 Introduction

Caused by stimulated Raman scattering (SRS) in an optical fiber with negative group-velocity dispersion (GVD), soliton self-frequency shift (SSFS) continuously red-shifts a soliton pulse's center wavelength under increasing the input power, thus enabling a red-shifted, continuously tunable Raman soliton source. Capable of providing femtosecond pulses at desired wavelengths that cannot be directly obtained from fundamental mode-locked ultrafast lasers, Raman soliton sources have found many important applications in spectroscopy and microscopy [24-27]. As a particular example of nonlinear wavelength conversion, difference-frequency generation (DFG) between a Raman soliton and the pulse that generates the Raman soliton has been widely used in obtaining femtosecond pulses in the mid-infrared (mid-IR) range [14-20]. Since the Raman soliton and the excitation pulse share the same repetition rate and carrier-envelope phase (CEP) offset, the resulting DFG source—if the excitation pulse's repetition rate is stabilized—becomes a mid-IR frequency comb with its CEP offset automatically set at zero. Such a mid-IR frequency comb constitutes an enabling tool for molecular spectroscopic applications because many molecules have their fingerprints in the mid-IR wavelength range. However, timing jitter and relative intensity noise (RIN) of a Raman soliton source will be transferred to the mid-IR frequency comb via DFG. In this chapter, we systematically study the noise performance of Raman soliton source.

2.2 Numerical simulation on Raman soliton timing jitter and RIN

The timing jitter and the RIN of a Raman soliton source are connected by soliton formation and subsequent SSFS, which can be accurately modeled by the generalized nonlinear Schrödinger equation (GNLSE) taking into account GVD, self-phase modulation (SPM), self-steepening, and SRS [11].

We solve the GNLSE to simulate a 50-fs, hyperbolic-secant pulse centered at 1.035 μm propagating inside a photonic crystal fiber (PCF), which is commercially available from NKT Photonics A/S. The fiber exhibits zero-dispersion at 0.945 μm with a mode field diameter of 2.8 μm at 1.035 μm, corresponding to a fiber nonlinearity of 23 $W^{-1}km^{-1}$. We denote this fiber as PCF-945 in this thesis. In the simulation, we fit the experimental dispersion curve provided by the manufacturer with a 12th-order polynomial (inset of Fig. 2.1(a)).

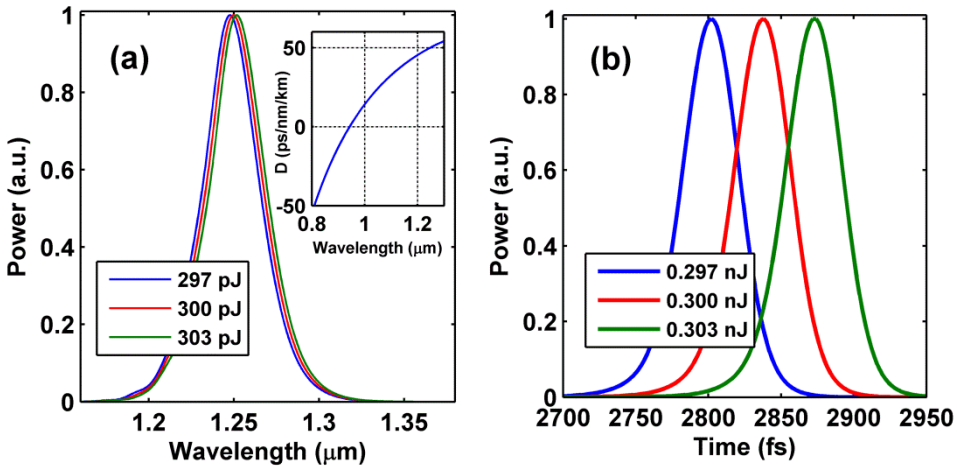

Fig. 2. 1. Simulation results for propagating a 50-fs pulse (initial center wavelength at 1035 nm) through 53-cm PCF-945 with the zero-dispersion wavelength at 945 nm. Three input pulse energies are chosen representing a ±1% energy variation with respect to 300 pJ. (a) Raman soliton spectra and (b) Raman soliton pulses corresponding to different excitation pulse energies: 297 pJ (blue), 300 pJ (red), and 303 pJ (green). Inset of (a) shows the dispersion curve of PCF-945.

Figure 2.1(a) shows the simulated Raman soliton spectra for three different excitation pulse energies (297 pJ, 300 pJ, and 303 pJ) after propagating through 53-cm PCF-945. The corresponding three Raman solitons have a pulse energy of 178.0 pJ, 179.2 pJ, and 180.4 pJ, respectively—a smaller relative energy fluctuation than the excitation pulses (0.67% versus

1%), which implies that a Raman soliton could exhibit lower RIN than the excitation pulse. As Fig. 2.1(a) shows, these three Raman solitons are centered at different wavelengths (i.e., 1.248 μm, 1.250 μm, and 1.252 μm at the fiber's output); therefore during SSFS, they propagate at different group velocities due to the fiber dispersion. Propagating in the anomalous dispersion region of the PCF, a Raman soliton with longer center wavelength travels slower than one with shorter center wavelength, and accumulates a larger temporal delay with respect to the excitation pulse at 1.035 μm. Figure 2.1(b) plots the three Raman soliton pulses corresponding to the excitation pulse energy of 297 pJ (blue), 300 pJ (right), and 303 pJ (green) in the time domain; they peak at 2802 fs, 2838 fs, and 2874 fs, respectively. Note that we solve the GNLSE using a frame of reference moving with the group velocity at 1.035 μm defined by the PCF's dispersion. The temporal peaking position of a Raman soliton therefore indicates the relative delay experienced by the Raman soliton with respect to a virtual pulse linearly propagating through the fiber with the center wavelength at 1.035 μm.

The results in Fig. 2.1(b) show that 1% change in the excitation pulse energy leads to 36-fs change of temporal delay. It suggests that the excitation pulse's RIN will be converted into relative timing jitter (RTJ) between the Raman soliton and the excitation pulse. This RTJ differs from the Raman soliton's absolute timing jitter with respect to the laboratory, which should include contribution from the excitation pulse's timing jitter. However, RTJ is of particular importance for nonlinear wavelength conversion that involves both spatially and temporally overlapping a Raman soliton and its excitation pulse in a nonlinear crystal. For example, DFG between these two pulses will transfer their RTJ to the derived mid-IR comb source manifesting as broadened comb lines and increased RIN. Minimizing RTJ of a Raman soliton is crucial for realizing a low-noise mid-IR frequency comb desired by molecular precision spectroscopy. To study how to minimize this RTJ of generated Raman soliton, we perform another simulation in which we fix the generated Raman soliton at 1.25 μm and vary the input excitation pulse parameters.

Raman soliton centered at a desired wavelength can be achieved by different combinations of fiber length, and excitation pulse energy and pulse duration. Figure 2.2 shows—by solving the GNLSE—nine possible parameter-combinations that result in a Raman soliton at the same wavelength of 1.25 μm using a PCF with its zero-dispersion wavelength (ZDW) at 0.945 μm. The excitation pulse's center wavelength is fixed at 1.03 μm. We vary the excitation pulse energy by 0.2% and record the corresponding timing change of the Raman

soliton. As Fig. 2 illustrates, increasing excitation pulse energy (with duration fixed at 100 fs, blue squares) or reducing the pulse's duration (with energy fixed at 0.5 nJ, red circles) both lead to (1) a shorter required PCF length to generate a Raman soliton centered at 1.25 μm, and (2) a decreased timing change. It suggests that a combination of shorter excitation pulse, higher excitation pulse energy, and shorter fiber length can reduce the relative timing jitter between a Raman soliton and its excitation pulse.

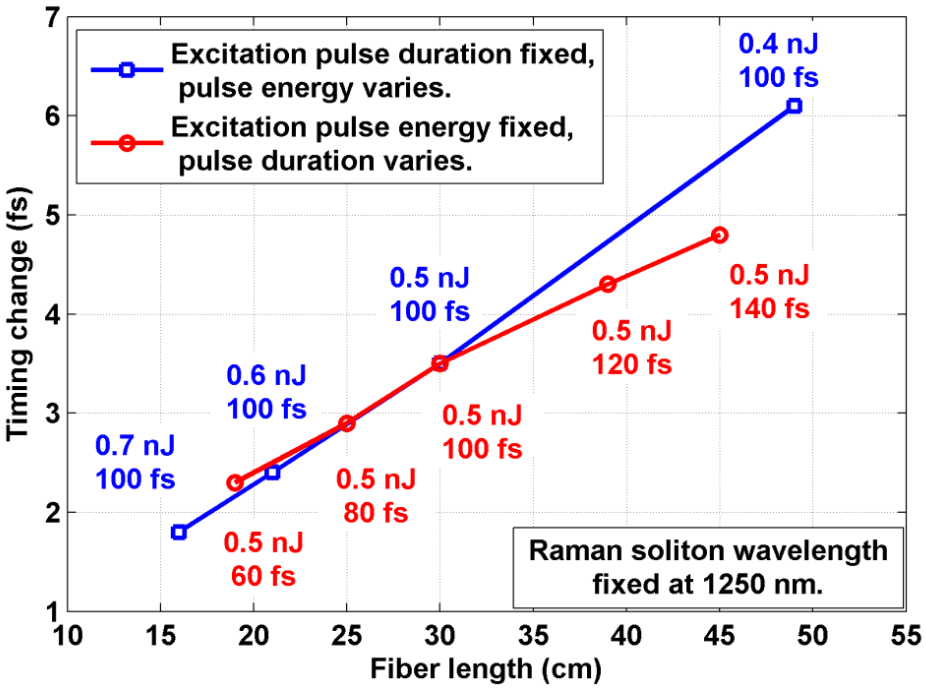

Fig. 2. 2. Simulation results for Raman soliton's timing change due to 0.2% change of the excitation pulse energy. A 1.03 μm excitation pulse propagates in a piece of PCF with zero-dispersion wavelength at 0.945 μm and the resulting Raman soliton's center wavelength is fixed at 1.25 μm.

2.3 Experimental setup

Guided by numerical simulation, we carry out a detailed experimental study on how to optimize such a parameter combination. Figure 2.3 illustrates the experimental setup.

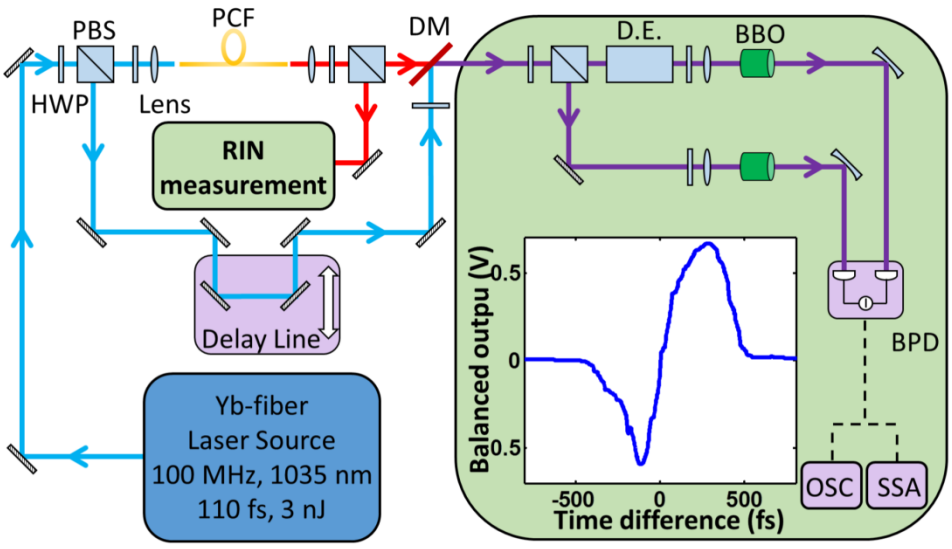

Fig. 2. 3 Schematic setup to characterize RIN and RTJ of Raman soliton source. PBS: polarization beam splitter, PCF: photonic crystal fiber, HWP: Half-wave plate, DM: dichroic mirror, D.E.: delay element, BBO: beta-BaB2O4 crystal, BPD: balanced photodetector, OSC: oscilloscope, SSA: signal source analyzer.

The home-built Yb-fiber laser system includes a 100-MHz Yb-fiber oscillator centered at 1035 nm, a single-mode Yb-fiber amplifier, and a pulse compressor. The 3-nJ, 110-fs pulses provided by the Yb-fiber laser system are then split into two arms using a half-wave plate and a polarization beam splitter (PBS). The pulses at one arm are coupled into a piece of PCF. By rotating the half-wave plate, we can continuously vary the optical power coupled into the PCF, and hence obtain a Raman soliton at a desired wavelength. The pulses at the other arm are used as a reference pulse. An optical delay line is added to the reference pulse arm. By fine tuning the delay line, we can temporally overlap the Raman soliton and the reference pulse. At the fiber output, a dichroic mirror (DM) is used to spatially combine the Raman soliton pulse and the reference pulse before sending them into a balanced optical cross-correlator (BOC) [28] to measure their RTJ. More specific, the power of the input pulse pair is first separated into two branches by a polarization beam splitter (PBS). In each branch, the pulse pair is focused into a 10-mm Type-I phase-matched beta-BaB_2O_4 (BBO) crystal (cutting angle: 21.9°) for sum-frequency generation (SFG). A delay element (DE) that consists of two half-inch cubes made of N-SF1 glass is inserted into one branch to provide a 150-fs delay offset. The two SFG signals are then filtered out by band pass filters (centered at 555 nm, bandwidth 40 nm) and finally detected by a balanced photodetector (BPD). The BOC curve—the BPD output voltages with respect to the time delay of the two input pulses at the DM—is measured and shown as the inset of Fig. 2.3. Apparently, BOC converts the

timing fluctuation between the two pulses to voltage fluctuation at the BPD output. In each BPD channel, the RIN of the Raman soliton or the excitation pulse also contributes to the voltage change, which as the common-mode noise is cancelled out in the balance detection. The delay line in the reference arm before the DM guarantees that the timing fluctuation falls within the detection range of the BOC. BOCs have been widely used in ultra-low timing jitter characterization [29, 30], timing error detection in timing distribution systems [31, 32], and pulse synthesis from independent mode-locked lasers [33].

2.4 RIN of Raman soliton

We optimize both the mode-locking state and net cavity-dispersion to minimize the oscillator's RIN, which is shown as the green curve in Fig. 2.4. The oscillator exhibits an integrated RIN of 0.018% from 10 Hz to 10 MHz. The Yb-fiber amplifier is optimized as well such that it only slightly degrades the RIN of the amplified pulses (red curve in Fig. 2.4). The measured RIN in the frequency range of 10 Hz to 2 kHz is buried under the instrument noise floor represented by the blue curve.

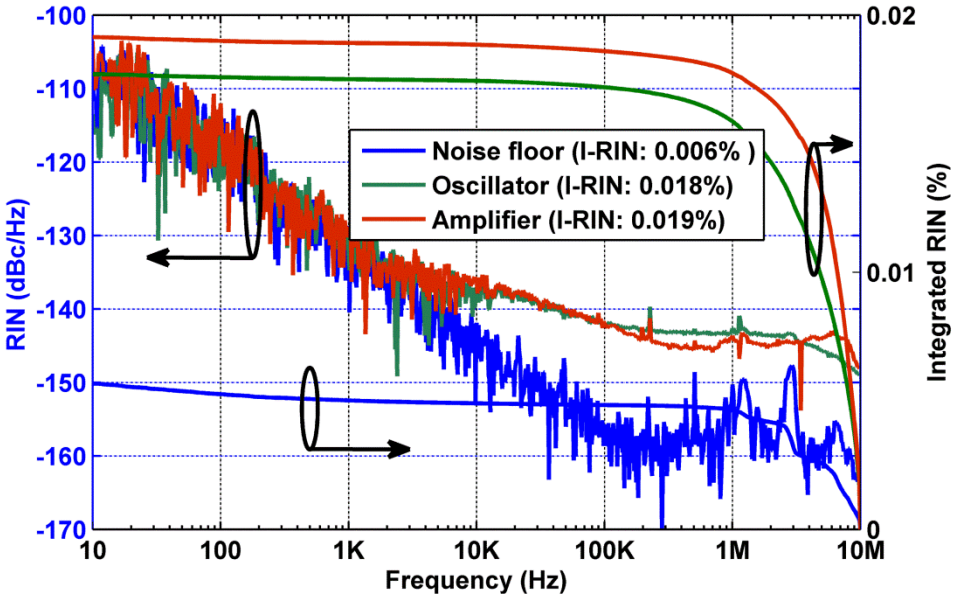

Fig. 2. 4. RIN spectra of oscillator (green curve) and amplifier (red curve). Instrument noise floor is shown as blue curve. The corresponding integrated RIN curves are obtained by integrating the RIN spectra from 10 MHz to 10 Hz, I-RIN: integrated RIN.

PCFs with different length and different zero-dispersion wavelength (ZDW) are used to generate tunable Raman soliton sources. We filter the Raman soliton and measure its RIN. First, we use a 3-m PCF-945 to obtain tunable Raman soliton pulses.

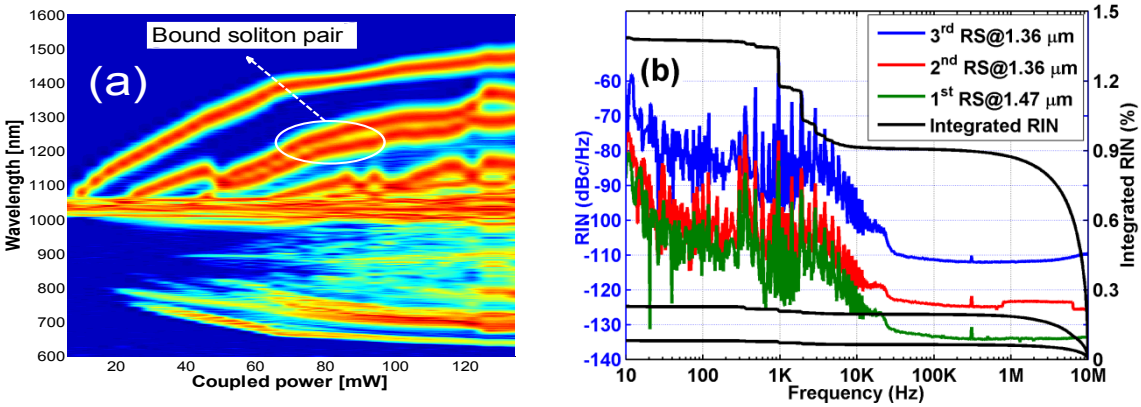

Fig. 2. 5. Experimental results from the 100-MHz Yb-fiber laser system. (a) Measured output spectra versus coupled average power into 3-m PCF-945. Spectral intensity shown on a logarithm scale. (b) RIN measurement of the 1st (green line), 2nd (red line), and 3rd (blue line) Raman solitons centered at 1.47 μm, 1.36 μm, and 1.27 μm, respectively. These three Raman solitons are generated using 3-m PCF with 134 mW coupled average power. The three black curves represent the corresponding integrated RIN for the 3 Raman solitons.

Figure 2.5(a) illustrates the output spectrum as a function of the coupled average power. At 10-mW average power, the first Raman soliton appears; it then red shifts continuously to 1.47 μm as the coupled power is increased to 134-mW. At 22-mW average power, the second Raman soliton emerges and the third one appears at 46-mW average power. They form a bound soliton pair at 134-mW average power; that is, two fundamental solitons interact with each other forming a pair right after the soliton fission. Although SRS red shifts the center wavelength of the bound solitons, the time delay between them remains constant during propagation. Bound soliton has been studied recently using Ti: sapphire laser (peaking at 0.8 μm) pumping PCFs [34]. However it is the first experimental observation that such a bound Raman soliton pair exists in such a large power range—from 50 mW to 120 mW. Beyond 120-mW average power, the bound soliton pair breaks. At 134-mW average power, we filter the 1st (at 1.47 μm), 2nd (at 1.36 μm) and 3rd (at 1.27 μm) Raman soliton and then measure their RIN separately. As Fig. 2.5(b) shows, the 1st Raman soliton has the lowest RIN (green line); depending on the center wavelength, it can be nearly one order of magnitude lower than the input pulse's RIN. The integrated RINs (black curves) corresponding to the 1st, 2nd, and 3rd Raman soliton are 0.075%, 0.23%, and 1.22%, respectively.

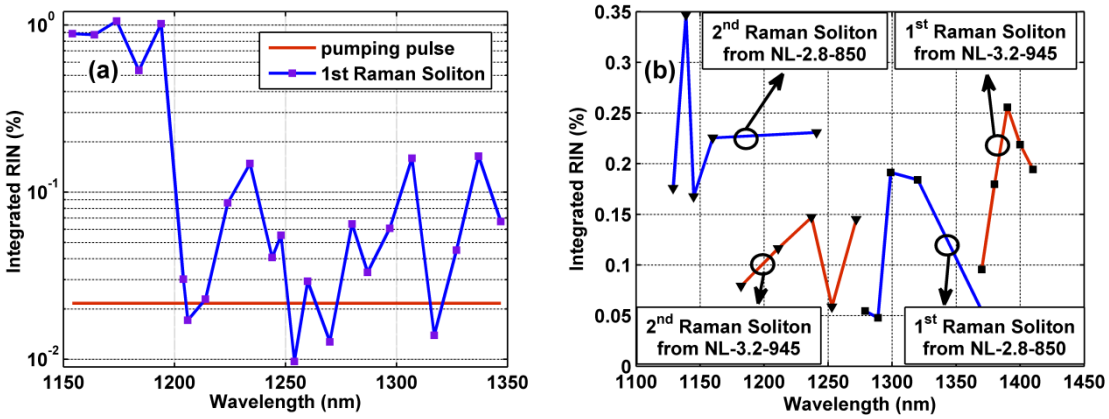

Fig. 2. 6. RIN of Raman soliton. (a) RIN of Raman soliton peaking shifted to different wavelength from 3-m PCF-945. (b)) RIN measurement (integrated RIN from 10 Hz to 10 MHz) of the 1st (labeled by triangles) and the 2nd Raman solitons (labeled by squares) generated by two PCFs: PCF-850 (blue solid curve) and PCF-945 (red solid curve). For each fiber, we vary the input pulse energy, and for each input pulse energy, we record the corresponding 1st Raman soliton and 2nd Raman soliton. RINs of five such Raman soliton pairs from each fiber are measured and shown as a function of Raman soliton's center wavelength.

As shown in Fig. 2.6(a), we also measured RIN (integrated from 10 Hz to 10 MHz) as a function the center wavelength of the first Raman soliton (i.e., the earliest ejected Raman soliton with the largest wavelength shift) generated from 3-m PCF-945. Also plotted in the figure is the Yb-fiber laser's RIN. The Raman soliton's RIN varies more than two orders of magnitude, and can be below the pumping pulse's RIN at some specific center wavelength. To study the RIN relationship between the first Raman soliton and the second Raman soliton, two different types of PCFs—PCF-850 and PCF-945 with the ZDW at 850 nm and 945 nm—are used in the experiments. One might speculate that the first Raman soliton has a lower RIN because it has shorter temporal overlap with other un-ejected fundamental solitons; therefore the shorter nonlinear interaction leads to less RIN, implying that the first Raman soliton—earliest ejected Raman soliton with the largest wavelength shift—has the lowest RIN. However, our study disproves this simple conjecture. Figure 2.6(b) summarizes the RIN measurement (integrated RIN from 10 Hz to 10 MHz) of the 1st and the 2nd Raman solitons generated by 1-m PCF-850 and 1-m PCF-945. As shown in the figure, the 1st Raman soliton's RIN can be higher or lower than the 2nd Raman soliton's RIN. There is not obvious relation between the RIN of 1st and 2nd Raman soliton.

2.5 RTJ of Raman soliton

Raman soliton centered at desired wavelength can be achieved by different combinations of fiber length, fiber dispersion, and the excitation pulse's duration and energy. To study the connection between RIN and RTJ of Raman soliton source, we intentionally shift the Raman soliton pulse to five specific wavelengths, covering 1200 nm to 1300 nm wavelength range, evenly spaced by 25 nm. Then we investigate the dependence of their RTJ on fiber length and fiber dispersion.

2.5.1 Dependence of RTJ on fiber length

We use PCF-945 at different lengths (i.e., 205 cm, 100 cm, and 28 cm) to generate Raman solitons centered at 1200 nm, 1225 nm, 1250 nm, 1275 nm, and 1300 nm. Figure 2.7 plots the RIN spectra of these Raman solitons obtained from 205-cm PCF-945. It is noteworthy that the RIN of Raman soliton at 1275 nm can be lower than the excitation pulse's RIN.

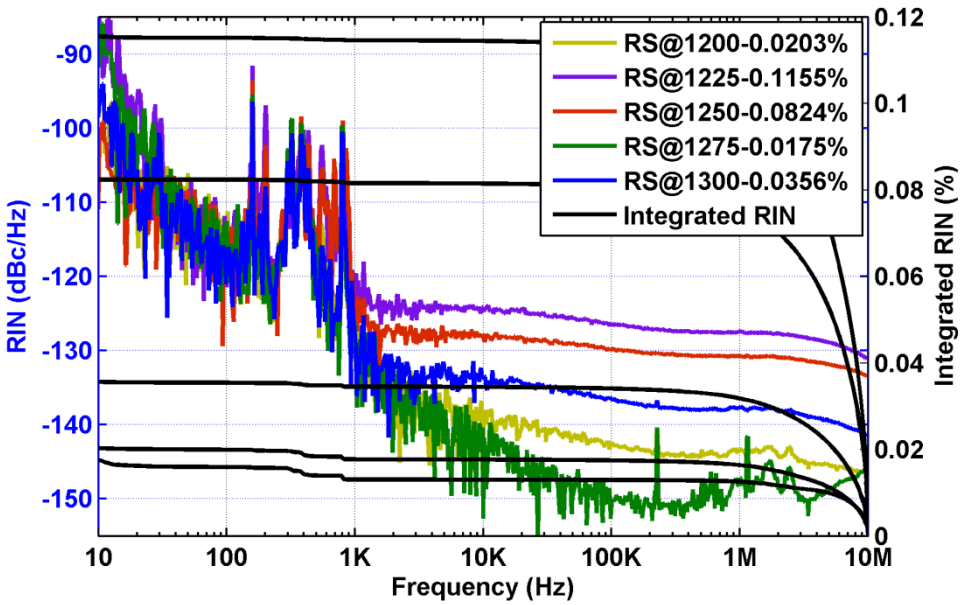

Fig. 2. 7. RIN spectra of Raman solitons generated from 205-cm PCF-945. Black curves: integrated RIN (Integrated from 10 MHz to 10 Hz). Curves in other colors: RIN spectra of Raman solitons centered at different wavelengths.

We also measure the RIN of SFG signal between the Raman soliton and the excitation pulse. Figure 2.8 shows the measured RIN spectra with the integrated RIN varying between 1% and 5%, which represents one order of magnitude higher than Raman soliton's RIN.

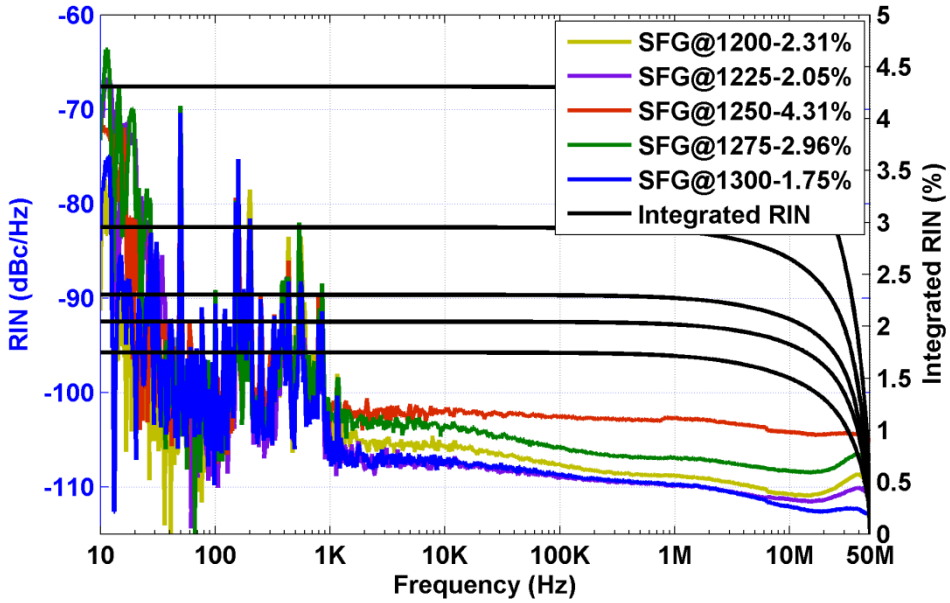

Fig. 2. 8. RIN spectra of SFG signal between Raman solitons generated by 205-cm PCF-945 and the excitation pulse. Black curves: integrated RIN (Integrated from 50 MHz to 10 Hz). Curves in other colors: RIN spectra.

We use the BOC to measure the RTJ between a Raman soliton and the excitation pulse. Figure 2.9 plots the jitter spectra of Raman soliton from 205-cm PCF-945. As we can see from the spectra, it is obvious that larger RTJ of Raman soliton results into larger SFG's RIN. The lowest RTJ between the Raman soliton and the excitation pulse is 33.8 fs.

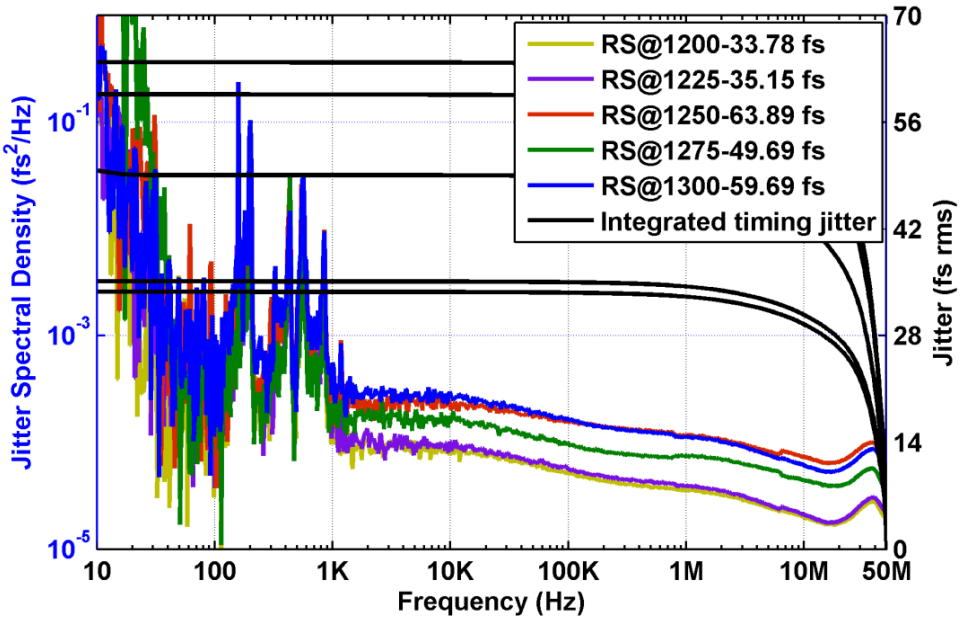

Fig. 2. 9. RTJ spectra for Raman solitons generated by 205-cm PCF-945. Black curves: show the corresponding integrated RTJ (Integrated from 50 MHz to 10 Hz). Curves in other colors: RTJ spectra of different Raman solitons.

To decrease the Raman soliton RTJ, we reduce the fiber length from 205 cm to 100 cm. Figure 2.10 shows the output spectra with the five Raman solitons peaking at 1200 nm, 1225 nm, 1250 nm, 1275 nm, and 1300 nm.

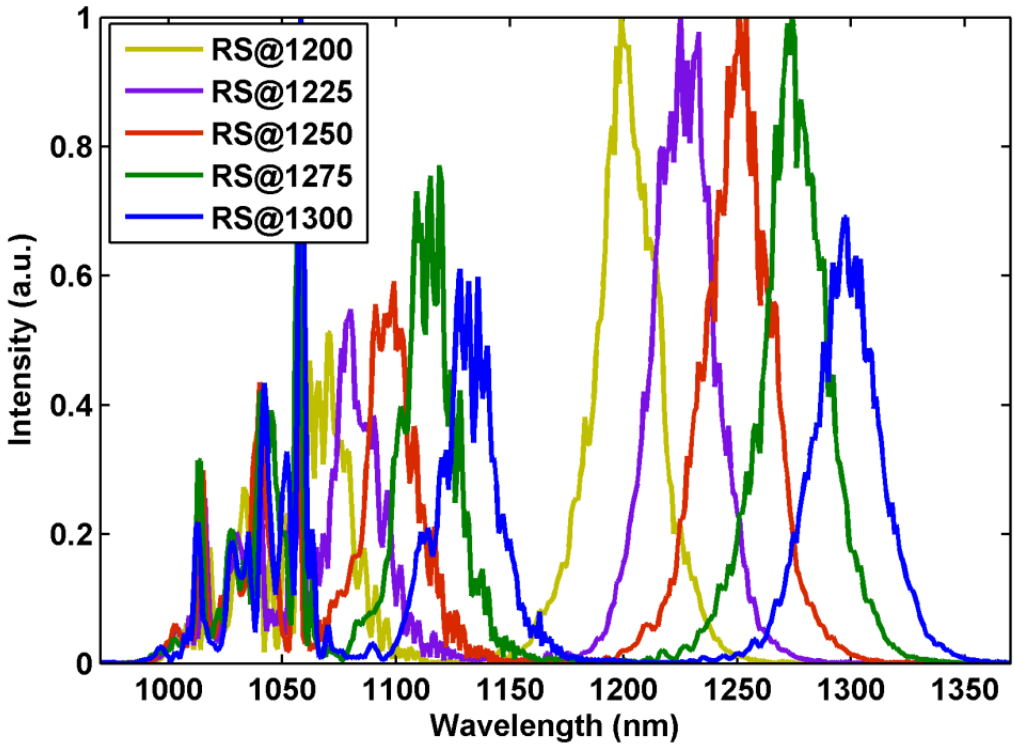

Fig. 2. 10. Raman solitons generated by 100-cm PCF-945.

We then spectrally filter the Raman solitons and measure their RIN (Fig. 2.11(a)) and the RIN of the SFG signal (Fig. 2.11(b)). The Raman soliton centered at 1275 nm exhibits lower RIN than the excitation pulse. The RIN of SFG signals is also one order of magnitude higher than the Raman solitons' RIN.

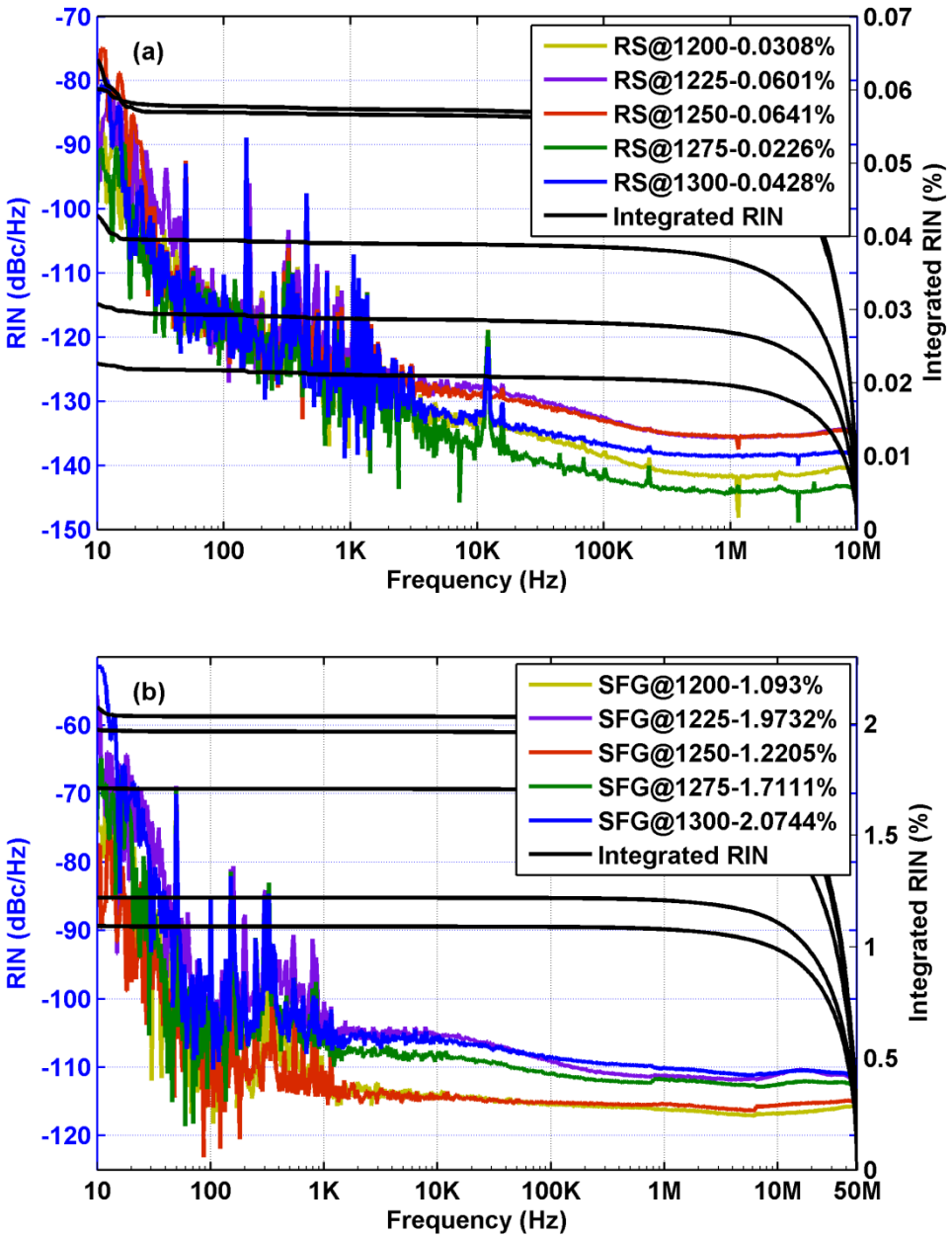

Fig. 2. 11. (a) RIN spectra of Raman soliton generated by 100-cm PCF-945. Black curves: integrated RIN (Integrated from 10 MHz to 10 Hz). Curves in other colors: RIN spectra of Raman solitons centered at different wavelengths. (b) RIN spectra of SFG signal between Raman solitons and the excitation pulse. Black curves: integrated RIN (Integrated from 50 MHz to 10 Hz). Curves in other colors: RIN spectra of SFG signal resulting from Raman solitons centered at different wavelengths.

We also measure the RTJ between the Raman solitons and the excitation pulses and plot them in Fig. 2.12. The lowest RTJ is 10.02 fs for the Raman soliton centered at 1225 nm and the highest is 39.93 fs for the Raman soliton centered at 1300 nm. Apparently the RTJ of Raman solitons obtained from 100-cm PCF-945 is much lower than the RTJ results corresponding to

205-cm PCF-945, suggesting that shortening fiber length is an effective way to decrease the RTJ.

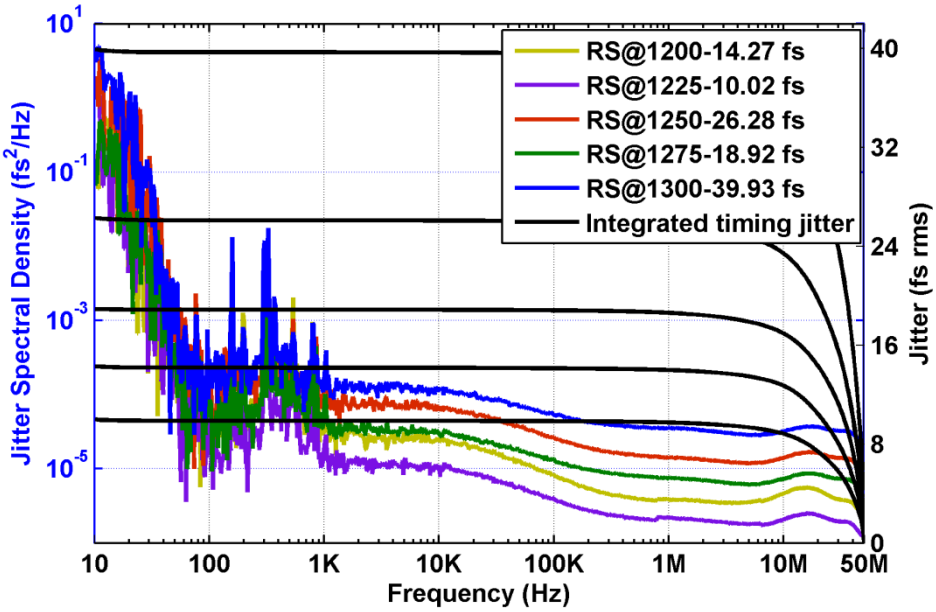

Fig. 2. 12. RTJ spectra for Raman solitons generated from 100-cm PCF-945. Black curves: integrated RTJ (Integrated from 50 MHz to 10 Hz). Curves in other colors: RTJ spectra of different Raman solitons.

To further reduce the RTJ, we shorten fiber PCF-945 to 28 cm. We expect the resulting RTJ of Raman soliton will exhibit around 1 fs or less. We first measure the RIN of Raman solitons (Fig. 2.13(a)). The integrated RIN is almost one order of magnitude higher than the RIN of Raman solitons generated by previous two fibers, with the length of 205 cm and 100 cm. This is because the fiber length of 28 cm is too short and the resulting Raman solitons are spectrally overlapping though they are well temporally separated. Therefore, the measured RIN is not the exact RIN of an individual Raman soliton. To verify our conjecture, we measure the generated SFG signals' RIN. SFG requires temporally overlapping a Raman soliton and the excitation pulse. We can adjust the relative delay between these two pulses such that the excitation pulse only overlaps with the first Raman soliton that has the largest wavelength shift. As a result, the contamination effect from other Raman solitons is prevented. Presumably the actual RIN of Raman solitons generated by 28-cm PCF-945 is close to that of Raman solitons generated by 100-cm PCF-945, we expect that the corresponding SFG signals should exhibit the same level of RIN.

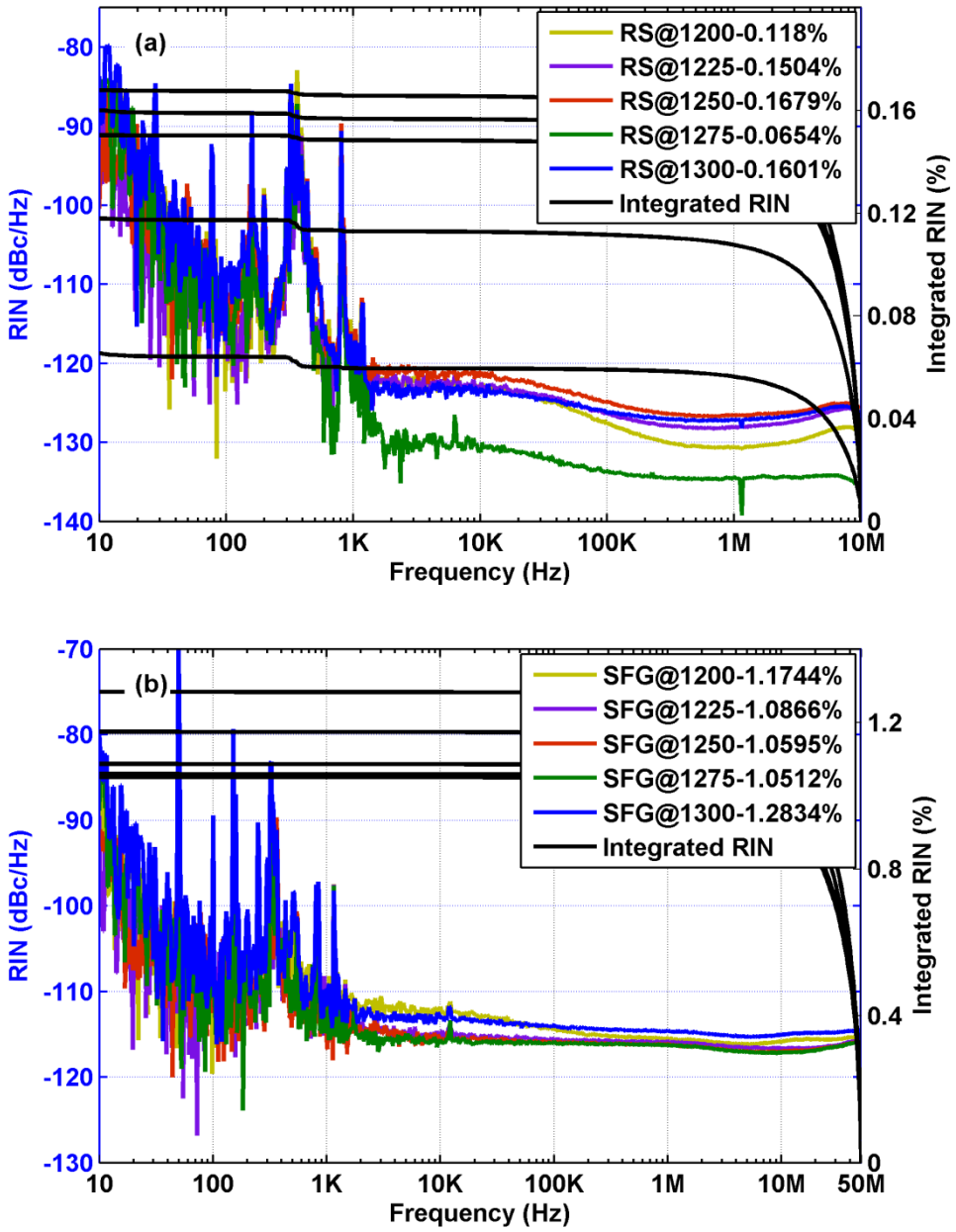

Fig. 2. 13. (a) RIN spectra of Raman soliton generated by 28-cm PCF-945. Black curves: integrated RIN (Integrated from 10 MHz to 10 Hz). Curves in other colors: RIN spectra of Raman solitons centered at different wavelengths. (b) RIN spectra of SFG signal between Raman solitons and the excitation pulse. Black curves: integrated RIN (Integrated from 50 MHz to 10 Hz). Curves in other colors: RIN spectra of SFG signal resulting from Raman solitons centered at different wavelengths.

Figure 2.13(b) plots the RIN spectra of SFG signals generated by mixing the excitation pulses and Raman solitons generated by 28-cm PCF-945. The integrated RIN is indeed at the same level as SFG's RIN using Raman solitons generated by 100-cm PCF-945, which proves our conjecture. Figure 2.14 shows the measured RTJ of Raman solitons obtained by 28-cm PCF-945. The Raman solitons have much lower RTJ compared with those results from longer fibers (i.e., 205 cm and 100 cm). The highest RTJ is 11.3 fs and the lowest 3.3 fs.

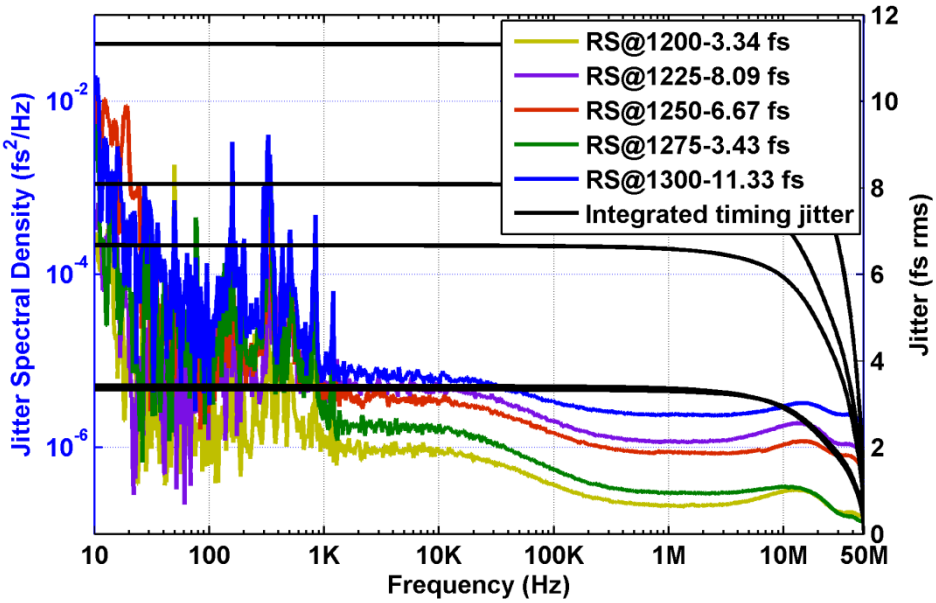

Fig. 2. 14. RTJ spectra between Raman solitons generated from 28-cm PCF-945 and the excitation pulse. Black curves: integrated RTJ (Integrated from 50 MHz to 10 Hz). Curves in other colors: RTJ spectra of different Raman solitons.

Table 2.1 summarizes the experimental results obtained from the same fiber (PCF-945) at different lengths (205 cm, 100 cm, and 28 cm). It shows that shorter fibers lead to lower RTJ. SFG signals' RIN is always at least one order of magnitude higher than Raman solitons' RIN, which is caused by the RTJ between the Raman solitons and excitation pulses.

Table 2. 1. Summary of PCF-945

		1200 nm	1225 nm	1250 nm	1275 nm	1300 nm
205 cm PCF-945	RIN	0.0203%	0.1155%	0.0824%	0.0175%	0.0356%
	SFG RIN	2.31%	2.05%	4.31%	2.96%	1.75%
	RTJ	33.78 fs	35.21 fs	63.89 fs	49.68 fs	59.67 fs
100 cm PCF-945	RIN	0.0308%	0.0601%	0.0641%	0.0226%	0.0428%
	SFG RIN	1.093%	1.9732%	1.2205%	1.7111%	2.0744%
	RTJ	14.27 fs	10.02 fs	26.28 fs	18.92 fs	39.93 fs
28 cm PCF-945	RIN	0.118%	0.1504%	0.1679%	0.0654%	0.1601%
	SFG RIN	1.1744%	1.0866%	1.0595%	1.0512%	1.2834%
	RTJ	3.34 fs	8.09 fs	6.67 fs	3.43 fs	11.33 fs

2.5.2 Dependence of RTJ on fiber dispersion

We also investigate the dependence of Raman soliton's RIN and RTJ on fiber dispersion. Three types of fibers are used in the experiment. We fix the fiber length at 28 cm, and couple the excitation pulse into the PCFs to generate tunable Raman solitons centered at 1200 nm, 1225 nm, 1250 nm, 1275 nm, and 1300 nm. The fibers— PCF-710, PCF-825, and PCF-945—have different ZDWs located at 710 nm, 825 nm, and 945 nm, respectively. Figure 2.15 shows their dispersion curves. At the excitation wavelength of 1.03 μm, PCF-945 has the smallest dispersion while PCF-710 has the largest dispersion.

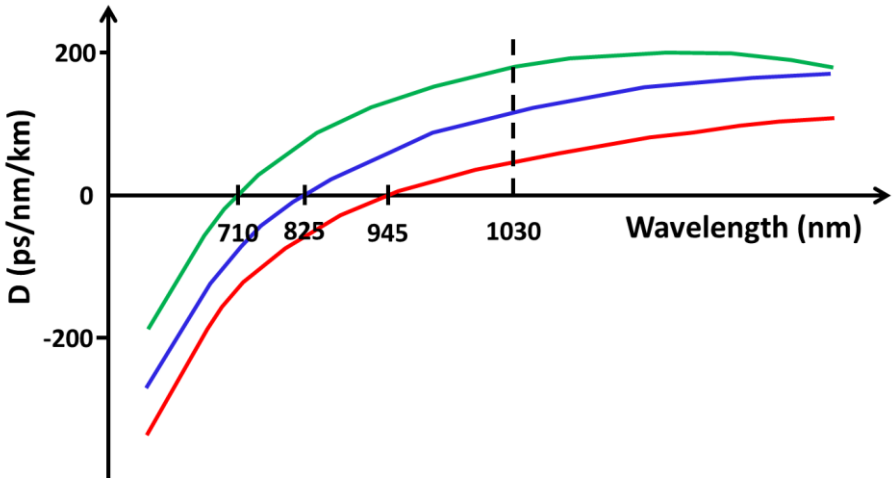

Fig. 2. 15. Dispersion curves for PCF-945 (red), PCF-825 (blue), and PCF-710 (green)

First we couple the excitation pulse into 28-cm PCF-825 and measure the Raman soliton's RIN and RTJ. The excitation pulse is coupled into the fiber by an aspheric lens (3.1-mm focal length) with 52% coupling efficiency. Figure 2.16 shows the Raman soliton spectra covering 1200-1300 nm. The Raman solitons' average powers are all ~10 mW.

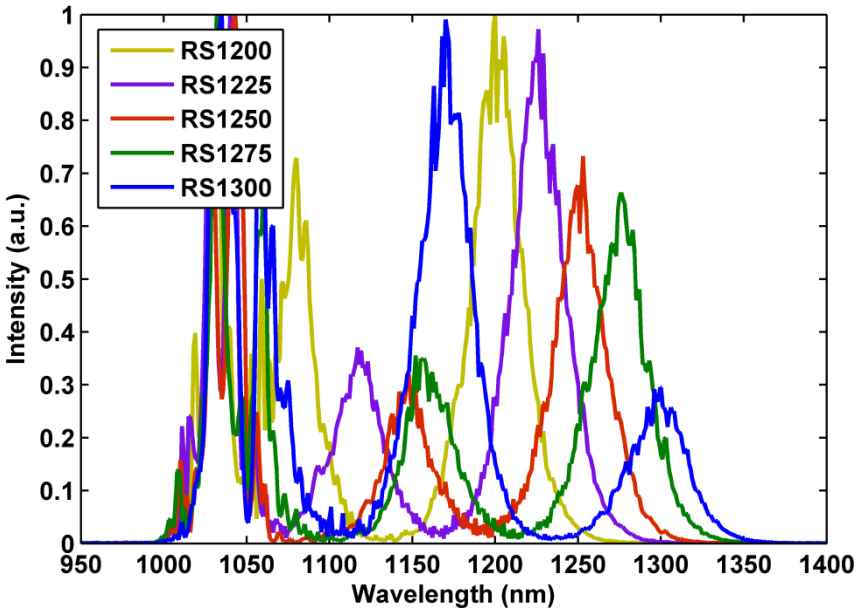

Fig. 2. 16. Spectrum of Raman solitons generated by 28-cm PCF-825.

Figure 2.17 plots the RIN spectra of Raman solitons generated by 28-cm PCF-825. It is worth noting that the RIN of Raman solitons centered at 1200 nm and 1300 nm is lower than the excitation pulse's RIN. All the Raman solitons' RIN are within the level of 0.05%.

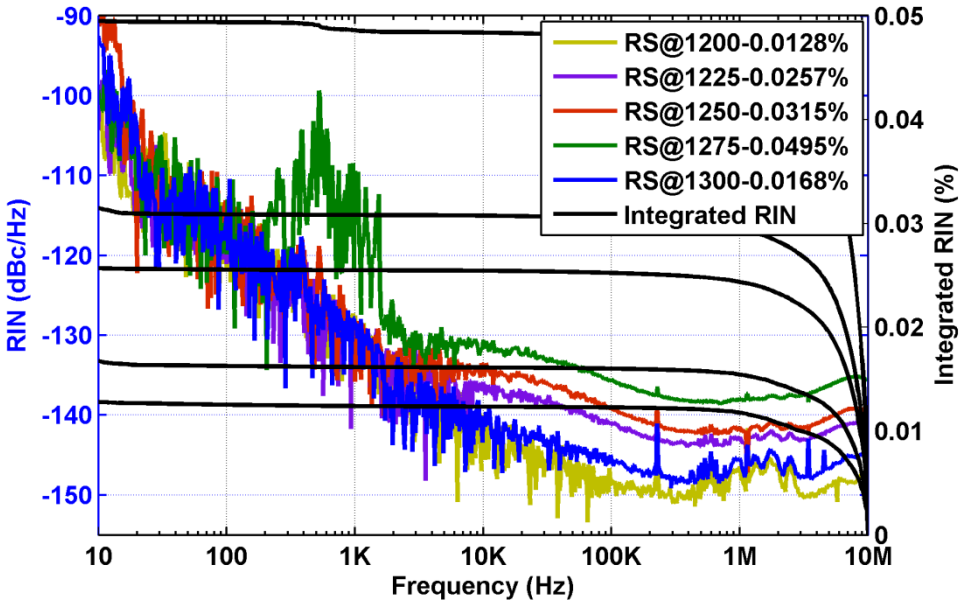

Fig. 2. 17. RIN spectra of Raman solitons generated by 28-cm PCF-825. The color curves show the RIN spectrum of Raman soliton centered at different wavelengths. Black curves: integrated RIN (Integrated from 10 MHz to 10 Hz).

We then use the same BOC to measure the RTJ between the excitation pulse and the Raman solitons generated by 28-cm PCF-825. The jitter spectra plotted in Fig. 2.18 shows that all the RTJs are 10-20 fs.

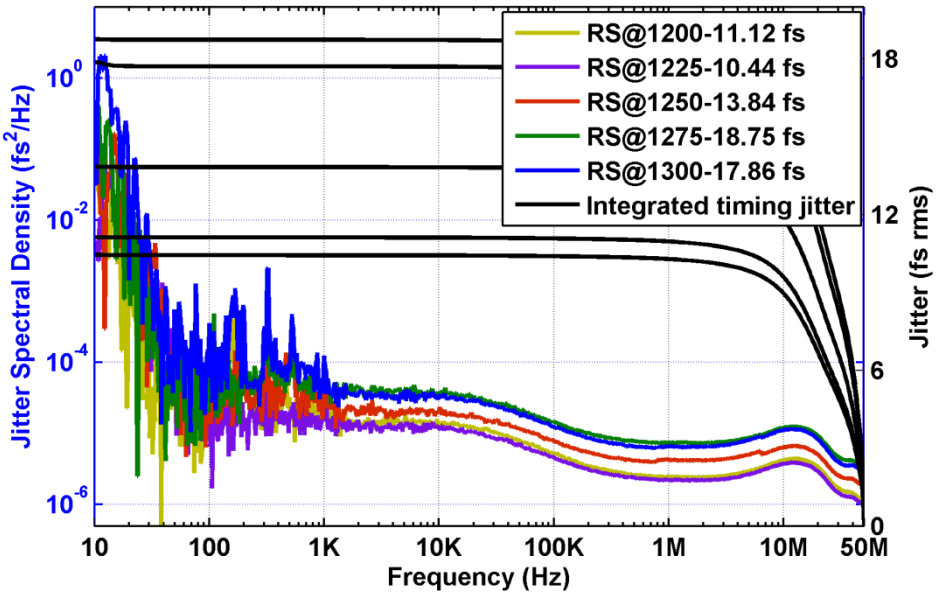

Fig. 2. 18. RTJ spectra between Raman solitons generated from 28-cm PCF-825 and the excitation pulse. Black curves: integrated timing jitter (Integrated from 50 MHz to 10 Hz). Curves in other colors: RTJ spectra for Raman solitons centered at different wavelengths.

For comparison, we also investigate the RIN and RTJ of Raman solitons obtained from 28-cm PCF-710, which has only 1.8-μm core diameter. An aspheric lens with 2-mm focal length is used to couple the excitation pulses into the fiber with 46% coupling efficiency, a reasonable value for power coupling into a PCF with such a small core. We can shift the Raman soliton to cover the wavelength range from 1200 nm to 1300 nm. Figure 2.19 plots the optical spectra of Raman solitons generated by 28-cm PCF-710. The first Raman soliton is clearly isolated from the main part of the spectrum. When the coupled power is increased, the first Raman soliton red shifts to longer wavelength and the second Raman soliton begins to separate from the residual spectral component at 1030 nm.

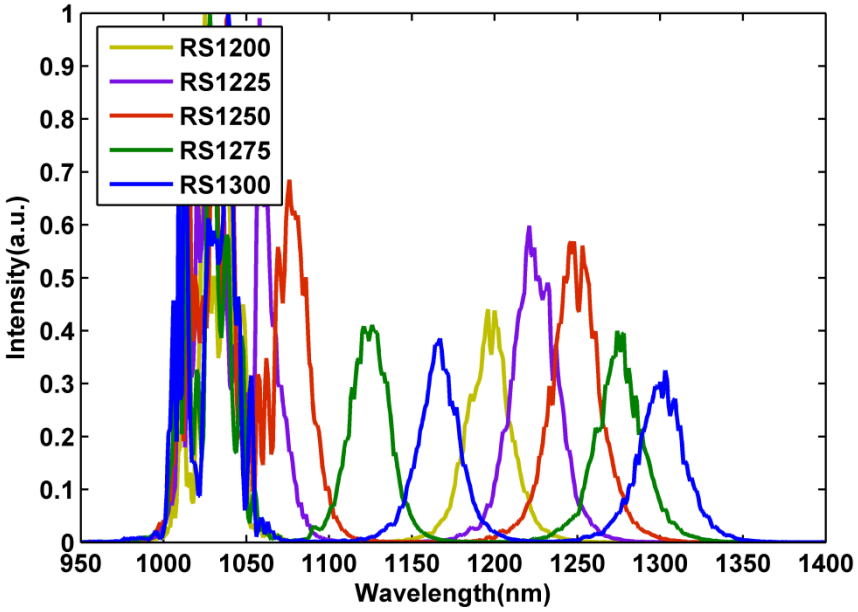

Fig. 2. 19. Optical spectra of Raman solitons generated from 28-cm PCF-710.

We filter the first Raman soliton and measure its RIN and RTJ, respectively. Figure 2.20 shows the RIN spectra of the Raman solitons generated from 28-cm PCF-710. Raman solitons at 1200 nm and 1225 nm have the RIN lower than the excitation pulses.

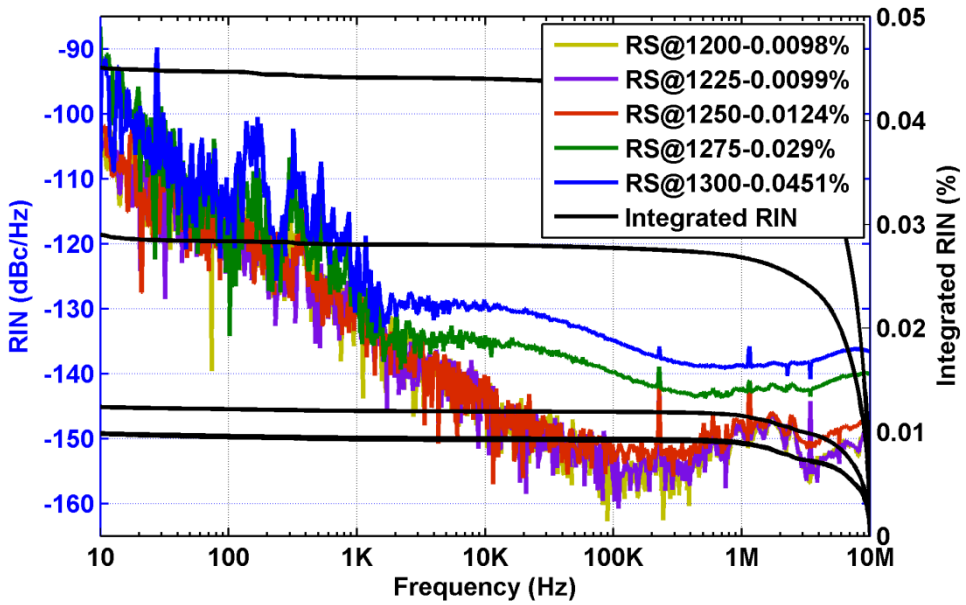

Fig. 2. 20. RIN spectra of Raman solitons generated from 28-cm PCF-710. Black curves: integrated RIN (Integrated from 10 MHz to 10 Hz). Curves in other colors: RIN spectra of Raman solitons centered at different wavelengths.

We also use the BOC to measure the RTJ between the Raman solitons generated by 28-cm PCF-710 and the excitation pulse (Fig. 2.21). All RTJs are slightly larger than those obtained from 28-cm PCF-825.

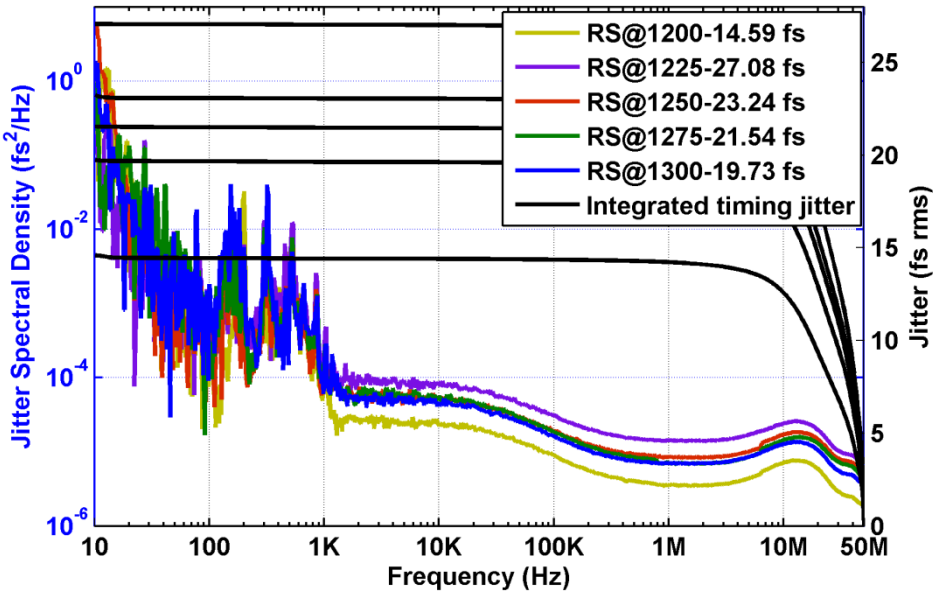

Fig. 2. 21. Jitter spectra between Raman solitons generated from 28-cm PCF-710 and the excitation pulse. Black curves: integrated timing jitter (Integrated from 50 MHz to 10 Hz). Curves in other colors: jitter spectra between Raman soliton and excitation pulse.

Figure 2.22(a) summarizes the integrated RTJ of Raman solitons generated by PCF-945 at different fiber lengths, demonstrating that shorter fiber length leads to less RTJ at all Raman soliton wavelengths. Figure 2.22(b) presents the integrated RTJs corresponding to different PCFs all at the same fiber length of 28 cm, showing that fiber with less dispersion results in less RTJ for Raman solitons centered at the same wavelength.

The results presented in Fig. 2.22 suggest that substantial reduction of RTJ of a Raman soliton can be achieved by minimizing the accumulated dispersion in a PCF. In practice, however, we have to keep the accumulated dispersion beyond a certain value. For an excitation pulse at a given duration, shifting a Raman soliton to a desired wavelength using less dispersive fiber with shorter length necessitates increasing the excitation pulse energy. With enough pulse energy, the excitation pulse forms a higher-order soliton at the beginning and then breaks into N fundamental solitons mainly caused by higher-order dispersion. These N fundamental solitons experience different amount of Raman self-frequency shift, leading to multiple Raman solitons appearing at different center wavelengths. If the accumulated

dispersion is too small, these N Raman solitons spectrally merge together manifesting as a supercontinuum. Consequently access to a specific Raman soliton using an optical bandpass filter becomes impractical. Furthermore, increased excitation pulse energy causes stronger nonlinearity during soliton fission, which is more sensitive to the excitation pulse's RIN. As a result, a resulting Raman soliton may suffer from higher RIN, which offsets the benefit of reducing the accumulated dispersion. Indeed, we have measured the RIN and RTJ of Raman solitons generated from 18-cm PCF-945; these Raman solitons have RTJs ~2 times larger than their counterparts obtained from 28-cm PCF-945 due to the increased RIN.

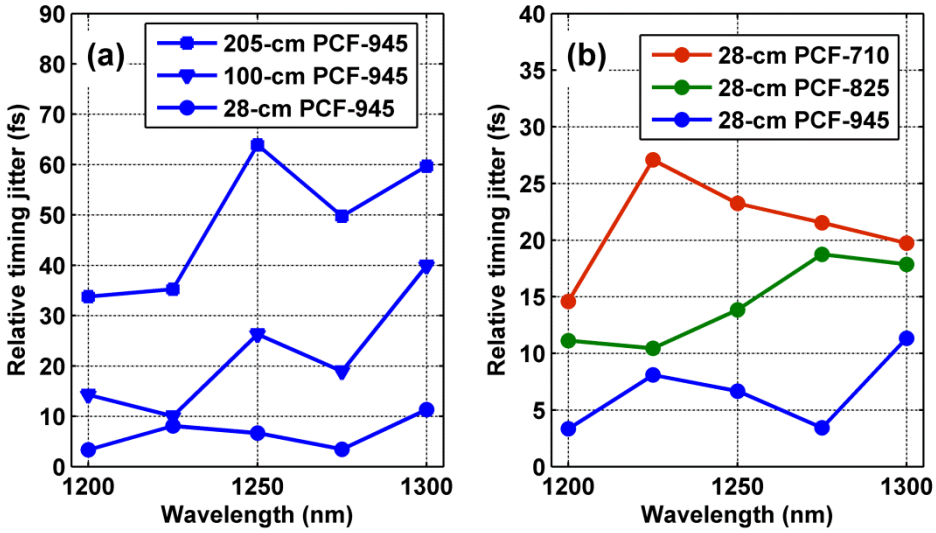

Fig. 2. 22. Integrated RTJ of Raman solitons generated by (a) PCF-945 with different fiber lengths: 28 cm (blue circles), 100-cm PCF-945 (blue triangles), 205-cm PCF-945 (blue squares) and by (b) 28-cm of PCF-945 (blue circles), PCF-825 (green circles), and PCF-710 (red circles).

The limitation imposed by increased excitation-pulse energy can be mitigated using shorter excitation pulses. For fixed excitation-pulse energy, short pulse duration leads to a soliton with smaller order (i.e., smaller N); the resulting Raman solitons also have shorter duration and red shift with a much faster rate. For example, for a 10-fs excitation pulse centered at 800 nm with 325 pJ pulse energy, 15-cm PCF-710 causes >300 nm wavelength shift, generating a spectrally well-isolated Raman soliton at 1120 nm [35].

2.6 Conclusion

We demonstrate that the RIN of an excitation pulse causes center-wavelength fluctuations of the resulting Raman soliton and then translates into the RTJ between the Raman soliton and the excitation pulse by fiber dispersion. A Raman soliton's absolute timing jitter is dominated at low frequency by the excitation pulse's timing jitter and at high frequency by the RTJ. Our experimental results suggest that RTJ can be significantly reduced by minimizing the accumulated fiber dispersion experienced by the Raman soliton using fibers with less dispersion and shorter length. Further optimization of the Raman soliton source may reduce the RTJ to attosecond-level, which is crucial for implementing a low noise mid-IR frequency comb via DFG between the Raman soliton and the excitation pulse.

Chapter 3

High-Power Yb-fiber laser system based on chirped-pulse amplification

3.1 Introduction

High power ultrafast Yb-fiber lasers are versatile tools for a variety of industrial and scientific applications such as laser machining using burst pulses generated by all fiber lasers [36] and cavity-enhanced high harmonic generation to dramatically increase the photon flux of generated extreme ultraviolet (EUV) pulses [37-39]. Although high power Yb-fiber laser system is becoming an attractive alternative to conventional solid-state lasers, there are also some limitations caused by the tight optical confinement of fibers. The accumulated nonlinear phase inside a high-power Yb-fiber amplifier may distort the amplified pulses. Chirped-pulse amplification (CPA) [40] technique has been introduced to linearly amplify pulses to avoid the nonlinear pulse distortion. In this chapter, we develop an ultrafast Yb-fiber CPA system—as schematically shown in Fig. 3.1—which consists of five parts: an Yb-fiber oscillator, a fiber stretcher, a single-mode pre-amplifier, a power amplifier, and a grating-pair based compressor. The 30-MHz Yb-fiber oscillator is mode-locked by nonlinear polarization evolution (NPE). The output spectrum is centered at 1030 nm with 24-nm bandwidth. The oscillator pulse is stretched from 2.9 ps to 54 ps by a fiber stretcher. A polarization-maintaining (PM) fiber pre-amplifier amplifies the stretched pulse from 9.4 mW to 390 mW. The amplified pulses are then further amplified to 20 W by a power amplifier. With a pair of transmission-gratings as the pulse compressor, the laser system eventually delivers 14.5-W (corresponding to 480–nJ pulse energy). This powerful laser source will be

used in Chapter 5 to provide both the pump pulses and the signal pulses to generate high power mid-IR pulses via difference-frequency generation. Next, we will present a detailed description of the fiver parts that comprise the whole Yb-fiber laser CPA system.

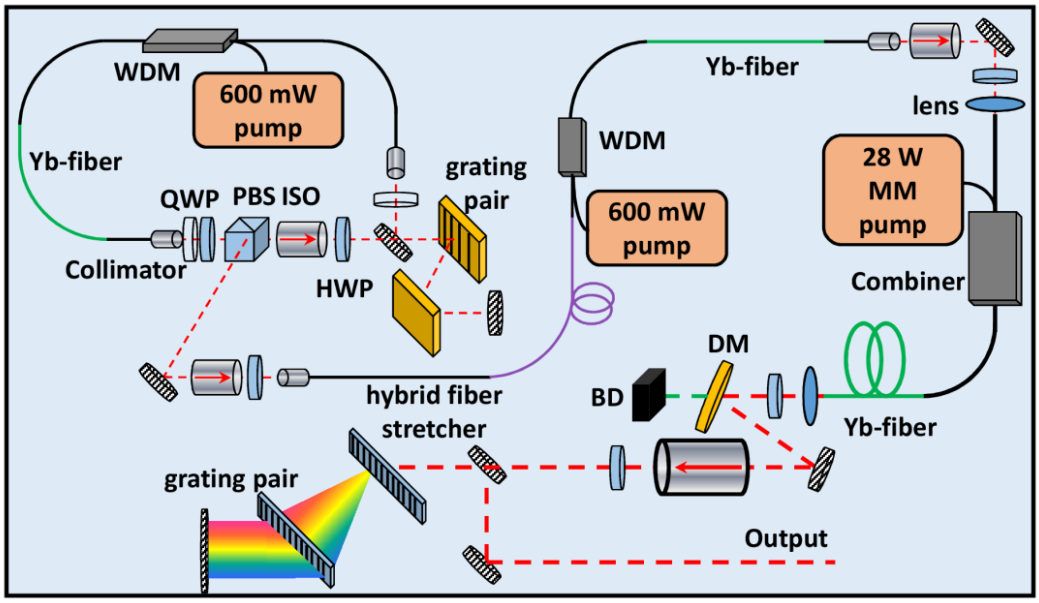

Fig. 3. 1. Schematic setup of Yb-fiber CPA system. WDM: wavelength division multiplexer, QWP: quarter-wave plate, PBS: polarization beam splitter, ISO: isolator, HWP: half-wave plate, MM: multi-mode, DM: dichroic mirror, BD: beam dumping.

3.2 Design of Yb-fiber oscillator

A well-functioned Yb-fiber oscillator is crucial for the whole laser system. For Yb-fiber lasers mode-locked by NPE, the lowest repetition rate reported is 12 MHz [41] while the highest repetition rate is 1 GHz [42]. Given a fixed average power, lower repetition rate means higher pulse energy. However, lower repetition rate leads to less stable mode-locked status because the intra-cavity pulse travels in the longer fiber and suffers more from 'environmental noise' such as temperature variation and mechanical vibration, which may disturb and even destroy the mode-locking.

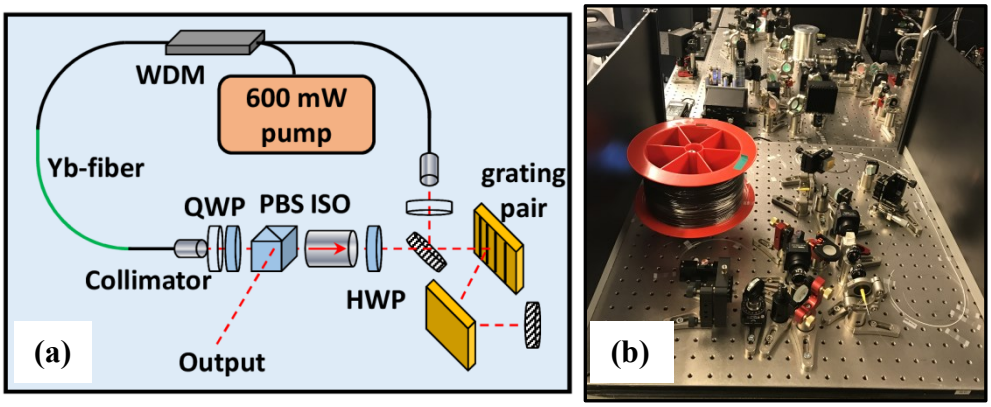

Fig. 3. 2. (a) Schematic setup of the Yb-fiber oscillator mode-locked by NPE. WDM: wavelength division multiplexer, QWP: quarter-wave plate, PBS: polarization beam splitter, ISO: isolator, HWP: half-wave plate. (b) Photo image of the Yb-fiber oscillator.

The repetition rate of our first Yb-fiber oscillator is set at 20 MHz. As Fig. 3.2(a) shows, the oscillator is constructed using both fiber devices and free-space elements. A wavelength division multiplexer (WDM) is used to couple pump light—provided by a single-mode laser diode at 976 nm—into the oscillator cavity. The gain medium is 60-cm Yb-fiber (YB 401 from CorActive). Two fiber-pigtailed collimators (from OZ Optics) are used for collimating the laser beam at the fiber exit. These two collimators provide 60 dB back reflection loss, which improves the laser stability. The free-space elements include two quarter-wave plates (QWPs), two half-wave plates (HWPs), a polarization beam splitter (PBS), an isolator (ISO), a pair of diffraction gratings, and two dielectric mirrors. The first QWP, HWP, the last QWP, and the PBS constitute the NPE mode-locking element [43-47]. The isolator ensures the unidirectional operation of the cavity. A HWP right after the isolator rotates the polarization back to horizontal to maximize the efficiency of the diffraction grating pair and thus reduces the total loss of the whole cavity. The grating pair provides negative group-delay dispersion (GDD) that compensates for the positive GDD introduced by the passive single mode fiber and the gain fiber. The second grating is mounted on a 1-dimensional translation stage with 50-mm travel range. Varying the grating-pair separation distance, the oscillator can be mode-locked in different net-cavity-dispersion regions. As we slightly increase the separation distance, the laser can be mode-locked in large normal dispersion region (i.e. dissipative soliton with 'Batman ear' on the spectrum), in close-to-zero dispersion region (stretched-pulse with relative smooth and broad spectrum), and in large negative dispersion region (soliton with Kelly sidebands on the spectrum). Figure 3.3 shows the oscillator spectrum, output pulse duration, and compressed pulse duration. The red curve in Fig. 3.3(c) plots the calculated autocorrelation trace for the transform-limited pulses.

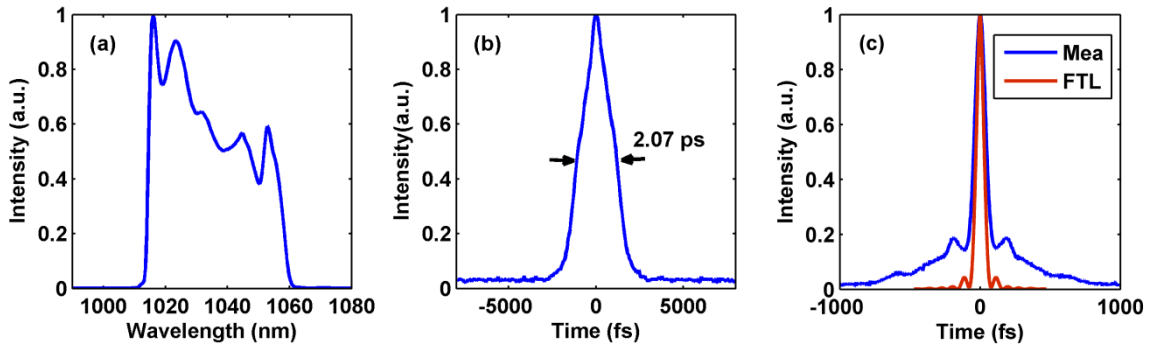

Fig. 3. 3. Characterization of 20-MHz Yb-fiber oscillator. (a) Spectrum of the mode-locked oscillator; (b) Measured auto-correlation trace of output pulses; and (c) Blue curve: measured auto-correlation trace of the compressed pulses, Red curve: calculated auto-correlation trace of the transform-limited pulses.

This oscillator has 20-MHz repetition rate and delivers 39-mW ultrashort pulses centered at 1026 nm. The optical spectrum has 24-nm bandwidth (Fig. 3.3(a)) and can support 59-fs FTL pulse (red curve in Fig. 3.3(c)). The measured auto-correlation (AC) trace (Fig. 3.3(b)) has 2.07-ps duration, a typical value for stretched-pulse mode-locking. A pair of transmission gratings (from LightSmyth, 1000 grooves/mm) de-chirps the output pulses and the AC trace of de-chirped pulses is depicted as the blue curve in Fig. 3.3(c). The compressed pulse duration is estimated to be 94 fs, which is almost twice the transform-limited pulse duration of 59 fs. Such a deviation and the large pedestal in the measured AC trace are due to the uncompensated higher-order dispersion. For example, the intra-cavity fibers and diffraction gratings have opposite sign of GDD and the same positive sign of TOD. When we use negative dispersion of a grating-pair to compensate for the positive dispersion introduced by fibers, the total TOD adds up, resulting in the large pedestal of the compressed pulses.

As seeding source to the following high power fiber amplifiers, the oscillator stability becomes the top priority. We intentionally blocked the laser cavity from time to time to see whether the mode-locking can be restored or not. The laser was self-starting and robust for the first two weeks, but unfortunately the slow drift of the fiber coupling and some unknown noise destroyed the mode-locking in the third week. In order to obtain a stable mode-locked seed oscillator, we shortened the total cavity fiber from 10 m to 6 m and the repetition rate is increased from 20 MHz to 30 MHz.

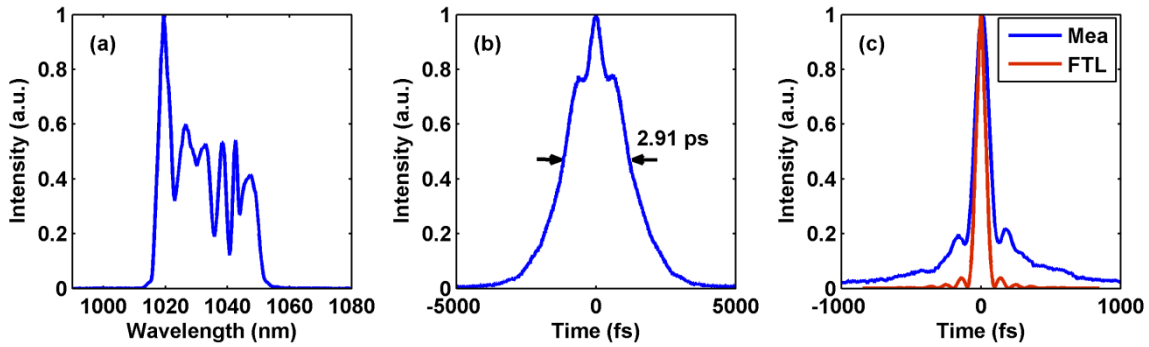

Fig. 3. 4. Characterization of 30-MHz Yb-fiber oscillator. (a) Spectrum of the mode-locked oscillator; (b) Measured auto-correlation trace of output pulses; and (c) Blue curve: measured auto-correlation trace of the compressed pulses, Red curve: calculated auto-correlation trace of the transform-limited pulses.

This oscillator delivers 26-mW ultrashort pulses centered at 1034 nm. Figure 3.4(a) plots the optical spectrum with 22-nm bandwidth, which supports 76-fs transform-limited pulse. Figure 3.4(b) shows the measured AC trace of output pulses, which has a duration of 2.91 ps. A pair of transmission gratings compresses the pulse down to 125 fs (Fig. 3.4(c)). During the following experiments, mode-locking of this oscillator never drops.

3.3 Design of fiber stretcher

Ultrashort pulses can be nonlinearly or linearly amplified to ~15-W average power. For nonlinear amplification, strong self-phase modulation (SPM) dramatically broadens the optical spectrum [48-52]. After the amplification, a diffraction-grating based compressor can dechirp the amplified pulses and result in much shorter pulse duration [53-55]. Linear amplification is normally implemented using CPA technique. The concept of CPA was first introduced in microwave region to increase the available power in radar in 1960 [56]. In 1985, CPA was introduced by Gérard Mourou and Donna Strickland into optical amplifiers, which since then has become a standard technique to amplify ultrashort pulses. In a CPA system, the short pulses prior to amplification are stretched to a much longer duration to avoid detrimental nonlinearity inside the amplifier, and the linearly amplified pulses are then compressed by a pulse compressor. A Martinez-type grating pair and a Treacy-type grating pair can provide opposite dispersions, and thus are normally used as the stretcher and compressor [40, 58]. To construct a compact Yb-fiber CPA system, diffraction-grating based stretcher may be replaced by a fiber stretcher. Conventional single-mode fibers provide both

positive GDD and TOD while a Treacy-type diffraction-grating compressor provides negative GDD and positive TOD. The positive TOD obtained from both fiber stretcher and the grating compressor will add up together while GDD cancels each other. To eliminate the TOD mismatch that may degrade the pulse compression, the refractive index of optical fiber can be engineered such that the resulting fiber exhibits positive GDD and negative TOD [57].

We obtained such stretcher fiber from OFS. This fiber has the core diameter of 2.6 μm, much smaller than the conventional single-mode fibers (e.g., 5.3 μm diameter for fiber HI-1060). To minimize the splicing loss between the OFS fiber and conventional single-mode fiber, we introduce bridge fibers in between. As depicted in Fig. 3.5, several tests are performed. The output of the 30-MHz Yb-fiber oscillator is coupled into a PM-980 fiber using an adjustable aspheric collimator (CFC-5X-B, Thorlabs Inc.) with 78% coupling efficiency. The direct output power from 1.5-m PM-980 is 20.5 mW. Two different bridge fibers are used in the test: 980-HP and UHNA-1, both commercially available from Thorlabs Inc. The mode-field diameter (MFD) diameter of PM-980, 980-HP and UHNA-1 is 6.6 μm, 4.2 μm, and 2.9 μm, respectively.

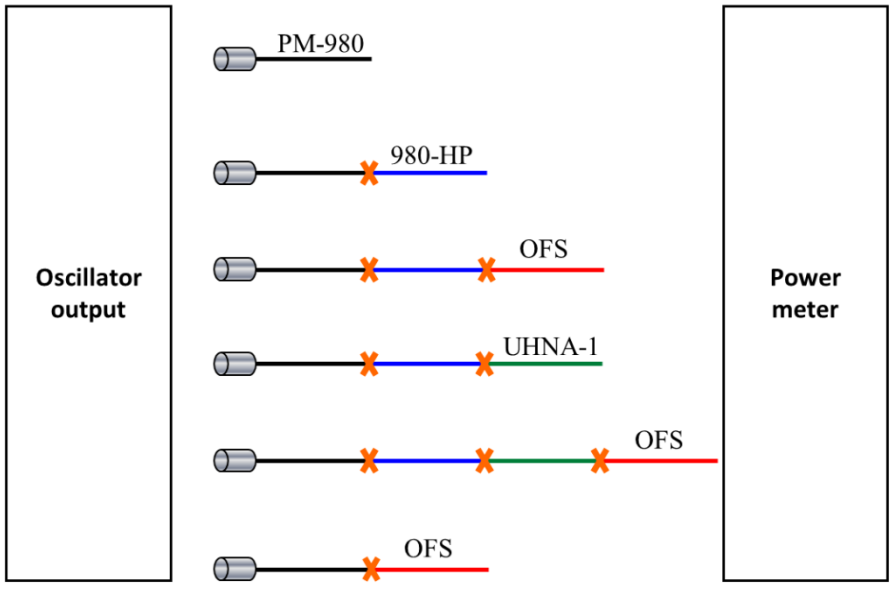

Fig. 3. 5. Schematic of bridge fiber test. The oscillator output pulse is coupled into PM-980 by a home-built APC connector and an adjustable aspheric collimator. Black line: PM980 fiber, blue line: 980-HP fiber, green line: UHNA-1 fiber, and red line: OFS fiber.

Table 3.1 summarizes our test results for a combination of different splicing modes and different bridge fibers. For the splicing mode SM-125, using bridge fibers introduces ~20 dB

loss. For SM-80 splicing mode, the loss is significantly reduced. For example, 2.85-mW average power is measured with both bridge fibers were spliced on, corresponding to 8.6 dB loss. The difference between these two splicing modes is the time of electrical discharge: the SM-80 discharges shorter time than SM-125 because SM-80 is used to splice single-mode fiber with 80-μm cladding diameter while SM-125 is utilized to splicing fiber with 125-μm cladding diameter. These experimental results seem to suggest that the splicing mode (discharge time) matters far more than the effect of bridge fibers. With many trials, we found that direct splicing between PM-980 and OFS fiber using PCF-PCF mode works quite well; 13.9-mW average power is measured at the output of OFS fiber, corresponding to an acceptable loss of 1.7 dB.

Table 3. 1. Summary of OFS bridge fiber splicing test

Splicing mode	Start fiber	Bridge fiber #1	Bridge fiber #2	Target fiber	Residual power
SM-125	PM-980	-	-	-	20.5 mW
	PM-980	980-HP	-	-	15.9 mW
	PM-980	980-HP	-	OFS	0.38 mW
	PM-980	980-HP	UNHA-1	-	15.5 mW
	PM-980	980-HP	UNHA-1	OFS	0.18 mW
SM-80	PM-980	980-HP	-	OFS	2.16 mW
	PM-980	980-HP	UNHA-1	OFS	2.85 mW
PCF-PCF	PM-980	980-HP	UNHA-1	OFS	9.4 mW
	PM-980	-	-	OFS	13.9 mW

Another concern is the fiber length ratio between PM-980 fiber and OFS fiber. The compressor of the CPA is constructed using a pair of transmission gratings (LightSmyth Technologies, Inc., with 1000 grooves/mm density). The size of the grating is 32 mm × 12 mm × 0.675 mm. Limited by the length (32 mm) of the transmission grating, the pulse to be amplified can be chirped at most to 60-ps duration.

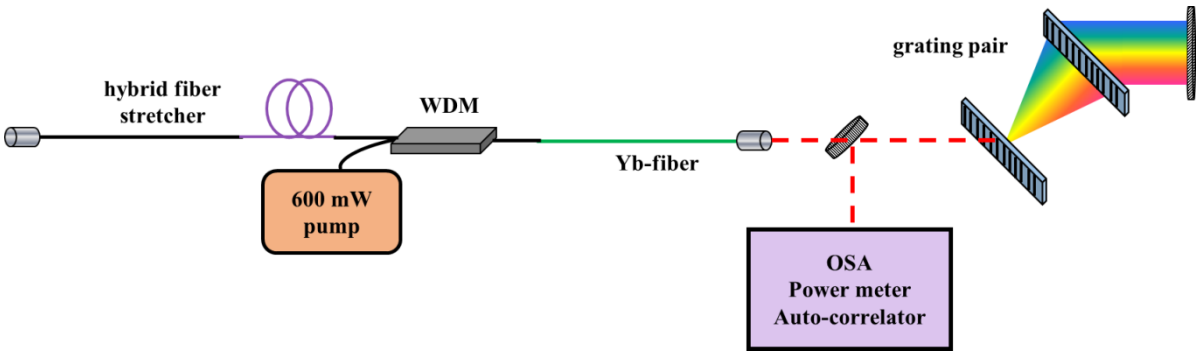

Fig. 3. 6. OFS/PM-980 ratio test system. WDM: wavelength division multiplexer. OSA: optical spectrum analyzer. Purple solid line represents OFS fiber.

To precisely compensate for the TOD in the fiber CPA system, the length ratio between PM-980 fiber and OFS fiber needs to be experimentally determined. We use the setup shown in Fig. 3.6 to optimize this hybrid fiber stretcher. The seed pulse produced by the 30-MHz oscillator is first stretched by the fiber stretcher, then amplified by a single-mode fiber amplifier, and compressed by a pair of transmission gratings. The seed pulse is calculated as 4.4 ps long according to auto-correlation trace shown in Fig. 3.7(b), and the transform-limited pulse duration is 51 fs according to the seed spectrum (Fig. 3.7(a)). After 1-m OFS fiber, the pulse was stretched from 4.4 ps to 8.4 ps, calculated according to auto-correlation trace shown in Fig. 3.7(c).

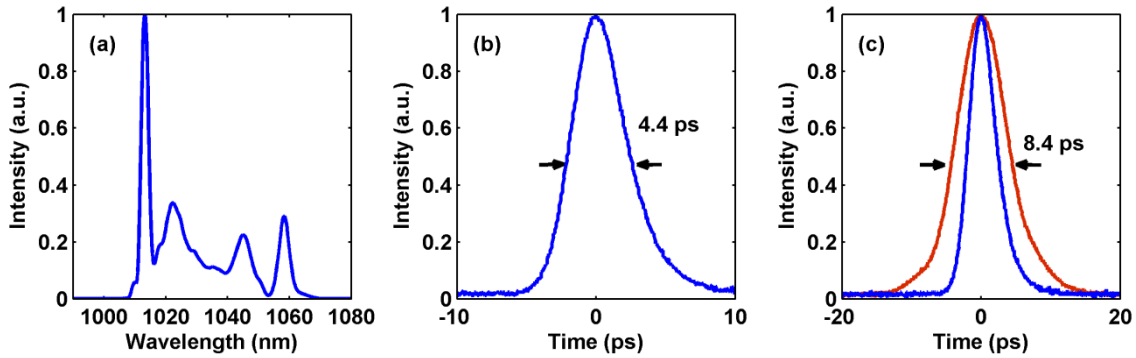

Fig. 3. 7. (a) Laser spectrum, (b) Measured auto-correlation trace of direct output pulse duration, (c) Measured auto-correlation trace after 1-m OFS fiber.

The GVD of PM-980 and transmission grating-pair can be found on datasheet, and TOD can be calculated. The GVD and TOD of OFS fiber is calculated by the experimental test. Table 3.2 shows the estimated value of GVD (β_2) and TOD (β_3) of OFS fiber, PM-980 fiber, and transmission-grating pair. In order to accumulate less nonlinearity in the amplification

process, a fiber stretcher including 2.63-m OFS fiber and 30.14-m PM-980 fiber leads to 50-ps stretched pulses. 26.5-cm grating-pair distance is required to fully compress these stretched pulses.

Table 3. 2. Summary of OFS/PM-980/Transmission grating-pair test

Dispersive element	$\beta 2$ (fs^2/m)	$\beta 3$ (fs^3/m)
OFS	7.358 × 104	-5.665 × 105
PM-980	2.139 × 104	4.278 × 104
Transmission-grating pair	3.169 × 106	7.749 × 105

3.4 Design of pre-amplifier

The stretched pulses after the fiber stretcher are then amplified in an Yb-fiber pre-amplifier. As shown section 3.3, the OFS fiber is not polarization maintaining (PM). To match the PM performance of the pre-amplifier and the power amplifier, an in-line polarization controller (PLC-900, Thorlabs Inc.) is used to improve the polarization extinction ratio at the input of the pre-amplifier. A HWP and a PBS are placed at the fiber output of the pre-amplifier. Figure 3.8 shows how to optimize the polarization extinction ratio (PER). A power meter measures the average power of horizontal polarization (p-polarization) light. Rotating the HWP can either maximize or minimize the average power of p-polarization light after PBS. The calculated PER is about 12 dB, acceptable for the subsequent amplification.

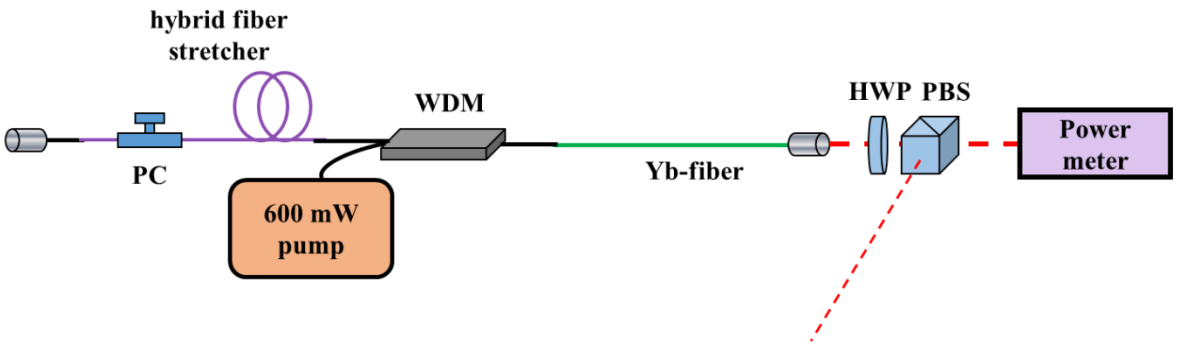

Fig. 3. 8. Optimization of polarization extinction ratio. WDM: wavelength division multiplexer, HWP: half-wave plate, PBS: polarization beam splitter

The pre-amplifier is comprised of a 600-mW pump diode at 976 nm (JDSU), a 976/1030 PM-WDM, and 65-cm Yb-fiber (Yb-401-PM, CorActive). The output fiber is angle polished at 8 degrees to avoid detrimental back reflection. The output of the pre-amplifier is collimated by an aspheric adjustable collimator (CFC-5X-B, Thorlabs). The output power versus pump power is shown in Fig. 3.9. The maximum average power after pre-amplifier is 379 mW, corresponding to a 16-dB gain given the 9.4-mW signal power. The pulse energy is about 12 nJ. An isolator (IO-5-1030-VLP, Thorlabs) is placed between the pre-amplifier output and the power amplifier input. The isolator blocks the backward amplified spontaneous emission generated by the power amplifier and improves the PER of the pre-amplified pulse from 12 dB to above 18 dB. The isolator has a transmission efficiency of 87%.

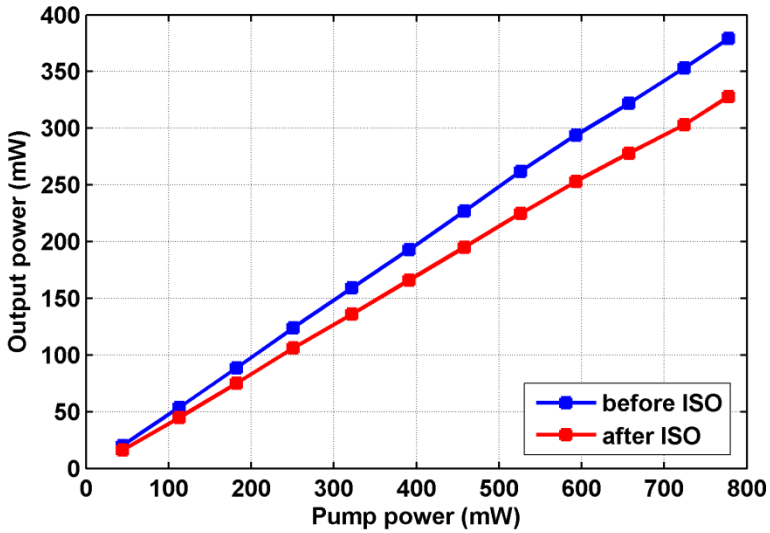

Fig. 3. 9. Output power of pre-amplifier versus pump power before isolator (blue squares) and after isolator (red squares).

Figure 3.10 shows the optical spectra before and after pre-amplifier. The intensity of shorter wavelength part is much stronger than the longer wavelength part, indicating the gain peak of the Yb-fiber is located at shorter wavelength.

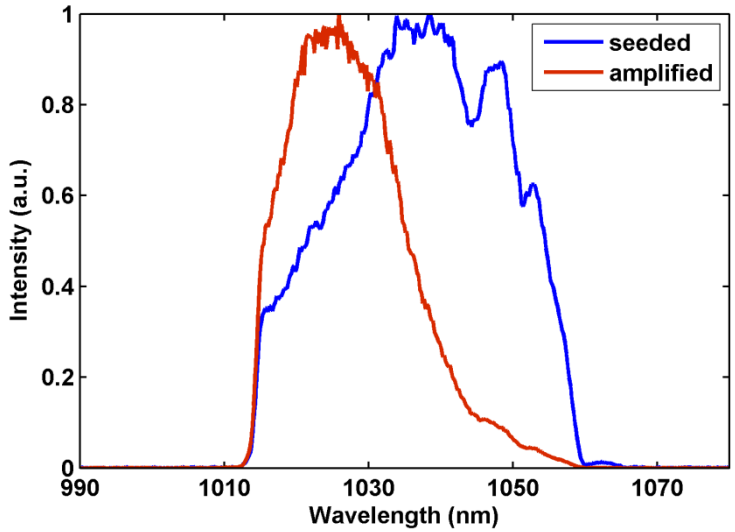

Fig. 3. 10. Optical spectra before (blue) and after (red) the Yb-fiber pre-amplifier.

3.5 Design of power amplifier

The high power Yb-fiber laser system aims to producing <200-fs pulses with 500-nJ pulse energy. To avoid the nonlinearity in the power amplifier, PLMA-YDF-25/250-VIII—a commercially available Yb-doped double-clad fiber from Nufern—is used as the gain fiber. This fiber has 25-μm core diameter and 250-μm cladding diameter. The 976-nm pump light is guided in the cladding while the 1030-nm signal light is guided in the core. The cladding absorption near 976 nm is 5.1 dB/m. As Fig. 3.11 shows, the power amplifier consists of a (2 + 1) × 1 beam combiner, a 976-nm MM pump diode, 2.6-m Yb-gain fiber, and coupling lenses for input and output. The beam combiner combines the 976-nm pump light with 1030-nm signal light and the combined light is sent into the Yb-gain fiber. The input signal fiber and output signal fiber are both 25/250-μm passive fiber. There are two pump fibers, which are traditional 105/125-μm multi-mode fiber. The end-face of input signal fiber is cleaved by 8 degrees to avoid back reflection.

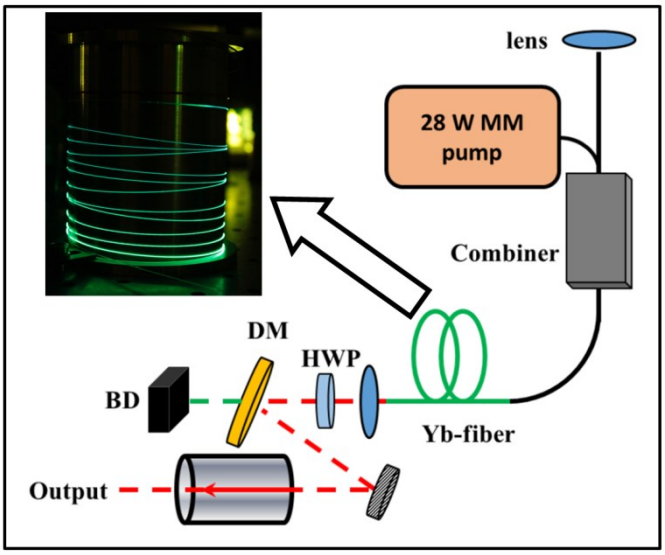

Fig. 3. 11. Schematic setup of the power amplifier. HWP: half-wave plate, DM: dichroic mirror, BD: beam dumping. Power amplifier's fiber is coiled to a post with 10-cm diameter. Inset shows the coiled gain fiber under optical pumping.

The large core size (25 μm) of the gain fiber allows several spatial modes (e.g., LP01, LP11, LP02 etc.) propagating inside the power amplifier. To simply estimate the single mode operation of an optical fiber, an important parameter, V, is defined as

$$V = \frac{2\pi a}{\lambda}(n_{core}^2 - n_{clad}^2)^{1/2} = \frac{2\pi a}{\lambda} NA, \tag{3.1}$$

where a is the fiber core radius, n_{core} the core refractive index, n_{clad} the cladding refractive index, λ the optical wavelength, and NA the numerical aperture. The single mode operation requires V number below 2.405. According to the equation and fiber parameter, one can calculate the cut-off wavelength. This V number is often used by the fiber manufacture as a guidance to design the optical fiber. Given that the core NA of fiber PLMA-YDF-25/250-VIII is ~0.07, calculated V number is ~5.1. Efficient suppression of higher-order spatial modes may be achieved by properly bending the fiber to introduce differential loss; that is, LP01 mode—the fundamental mode—experiences much less loss than other higher-order modes (such as LP02, LP11 etc.). A coiling post made of aluminum with 10-cm diameter is machined. Inset of Fig. 3.11 shows the gain fiber coiling to the post when in operation. The coiling introduces sufficient losses to remove the higher-order modes inside the multi-mode fiber. Consequently only the fundamental mode is guided and amplified in the power amplifier.

At the initial design, a fiber-pigtailed high-power collimator was employed to output the laser pulses. However, the amplified pulses reach >500-nJ pulse energy and cause strong nonlinearities in the collimator fiber. The autocorrelation of the compressed pulses exhibits

significant pedestal. Therefore we remove the high power collimator and free-space coupled out the amplified pulses. The output end-face of the Yb-fiber is 8-degree angle cleaved followed by a spherical lens (LA1560-B-ML, Thorlabs) to collimate the laser beam.

The red line in Fig. 3.12(a) shows the output power of power amplifier as a function of pump power with 76.4% slope efficiency. The pump-current threshold of the power amplifier is 2000 mA, corresponding to pump power of 4.35 W. The maximum output average power is obtained under the 12-A pump current, corresponding to 28.9-W pump power. The pump and the signal are propagating in the same direction. A dichroic mirror (DM) is utilized to separate the residual pump and signal light. The measured residual pump is 1.71 W, while the measured signal power is 20.3W. The average power may be further increased if more pump power is available. The TEC temperature (blue curve in Fig. 3.12(a)) was finally set at 27 ˚C to maximize pump absorption at the highest pump power. The TEC temperature needs to be adjusted with respect to pump power such that the emitting wavelength of the multi-mode pump diode is fixed at 976 nm to maximize the pump absorption in the gain fiber (i.e., PLMA-YDF-25/250-VIII).

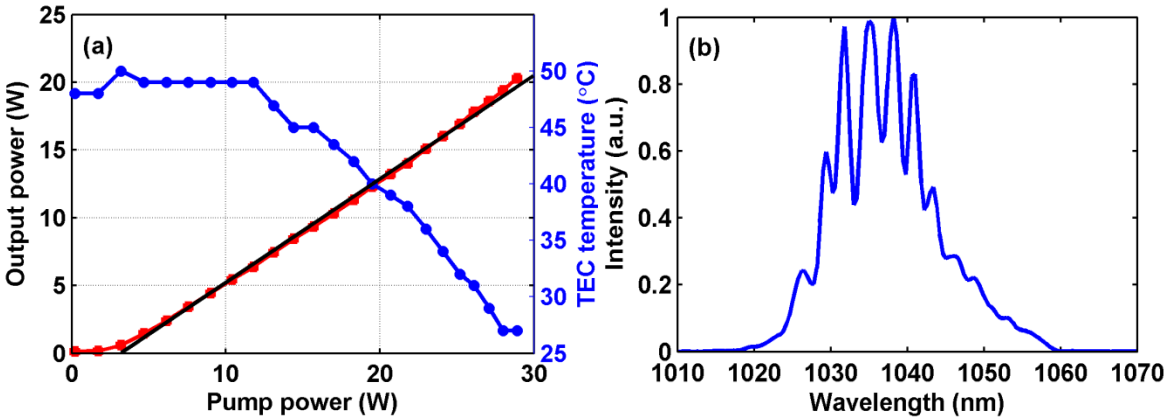

Fig. 3. 12. Characterization of the power amplifier. (a) Red line: output power versus pump power; blue line: TEC temperature versus pump power for the pump wavelength fixed at 976 nm. (b) Optical spectrum at the 20.3-W maximum output power.

Figure 3.12(b) shows the optical spectrum of the amplified pulses at the maximum average power of 20.3 W. The spectral bandwidth (FWHM) is 12 nm. The PER of the amplified pulses drops to 9.1 dB is mainly due to the amplified spontaneous emission in the power

amplifier. In the end, amplified pulses with >20-W average power centered at 1035-nm are obtained, corresponding to >660-nJ pulse energy.

3.6 Design of grating compressor

The amplified pulses are de-chirped using a transmission-grating pair compressor. The compressor includes two fused-silica transmission gratings (1000 grooves/mm line density, from LightSmyth Technologies) with a maximum diffraction efficiency of >94% under Littrow conditions at 1040 nm. The incident angle is set at 31 degrees. To avoid any PER degradation after compressor, the laser light is adjusted to be p-polarization by a HWP placed before the gratings. The overall efficiency of the compressor at double-pass configuration is ~78%.

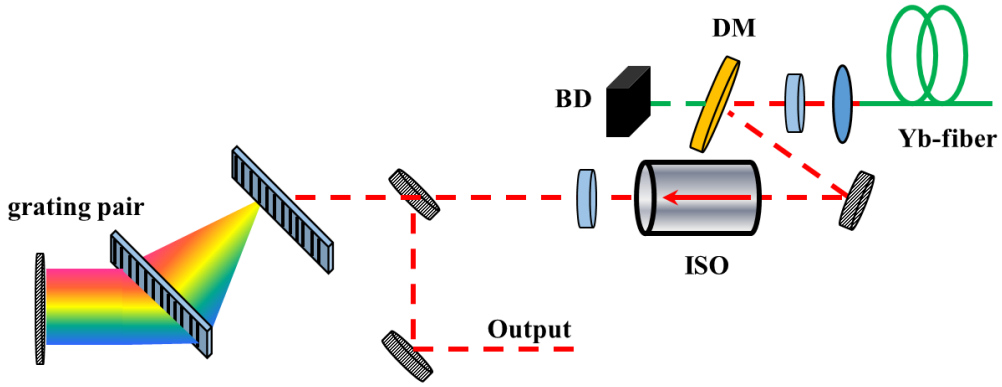

Fig. 3. 13. Schematic setup of transmission-grating pair compressor. DM: dichroic mirror, BD: beam dumping.

Figure 3.13 shows the schematic setup of the compressor, including part of the power amplifier. The dichroic mirror (DM) (LAYERTEC) separates the residual pump and the amplified signal; it has 99.9% reflectivity in 1020-1200 nm and <3% reflectivity in 900-985 nm at the incident angle of 22.5 degrees. A high-power free-space optical isolator with 5-mm clear aperture is placed right after the DM. The minimum isolation is 22 dB, well enough to prevent small back reflection. A HWP is set after the isolator to fine tune the polarization of the amplified pulses. The two gratings are separated by ~35 cm. Two dielectric mirrors are combined to form a roof mirror reflecting the dispersed pulses back through the grating pair for a second pass.

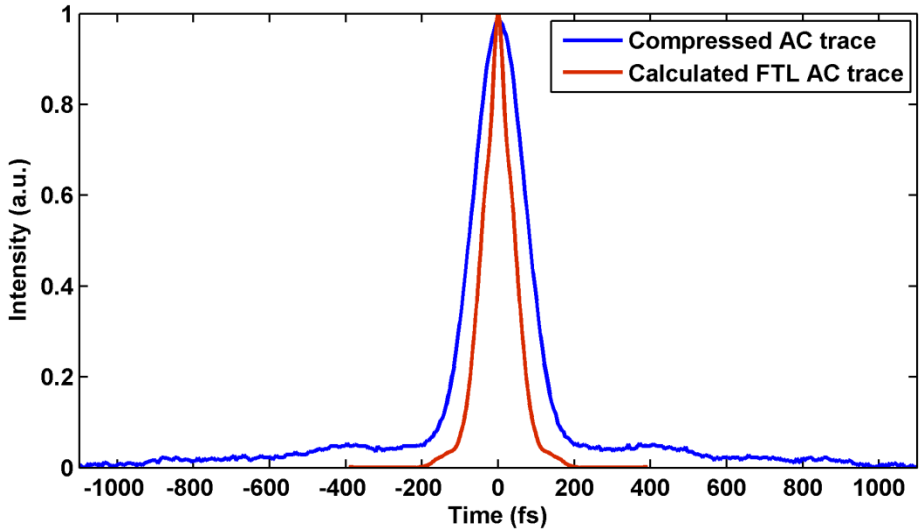

Fig. 3. 14. Blue curve: Measured auto-correlation trace of compressed pulses. Red curve: calculated autocorrelation trace of the transform-limited pulses.

Figure 3.14 depicts the auto-correlation (AC) trace of the compressed pulse. The blue curve shows the AC trace for the compressed pulses at the maximum average power of 14.5 W. Calculated FWHM is 165 fs using a deconvolution factor of 1.41 by assuming that the compressed pulses are in Gaussian profile. For a comparison, we plots in the same figure the calculated auto-correlation trace of the transform-limited (red curve). The duration of the transform-limited pulse is 90 fs. As we can see from the figure, the compressed pulse has a pedestal extending from -1000 fs to 1000 fs. This pedestal is caused by the uncompensated nonlinear spectral phase. To minimize the pedestal of the compressed amplified pulses, a band-pass filter (NB-1050-020 nm, Spectrogon) is placed between the free-space output of oscillator and the single-mode pre-amplifier. The filter is centered at 1050 nm with 20-nm bandwidth. Fine tuning the filter can manipulate the input spectrum to the pre-amplifier. Consequently the output spectra of the pre-amplifier and the power amplifier are both changed, which can be used to further optimize the quality of the compressed pulses.

3.7 Conclusion

We demonstrate a high power Yb-fiber laser system that emits ultrashort pulses centered at 1035 nm with 30-MHz repetition rate. The average power is 14.5 W corresponding to 483-nJ pulse energy. The optimized compressed pulse duration is 165-fs. Figure 3.15 shows the whole experimental setup of the high power Yb-fiber laser system. The oscillator and stretcher parts are constructed on a 600 mm × 600 mm breadboard; the pre-amplifier, the power amplifier, and the grating-pair compressor are placed on a 600 mm × 900 mm breadboard. This high power laser system is beneficial for generation of high-power mid-infrared femtosecond pulses based on difference-frequency generation.

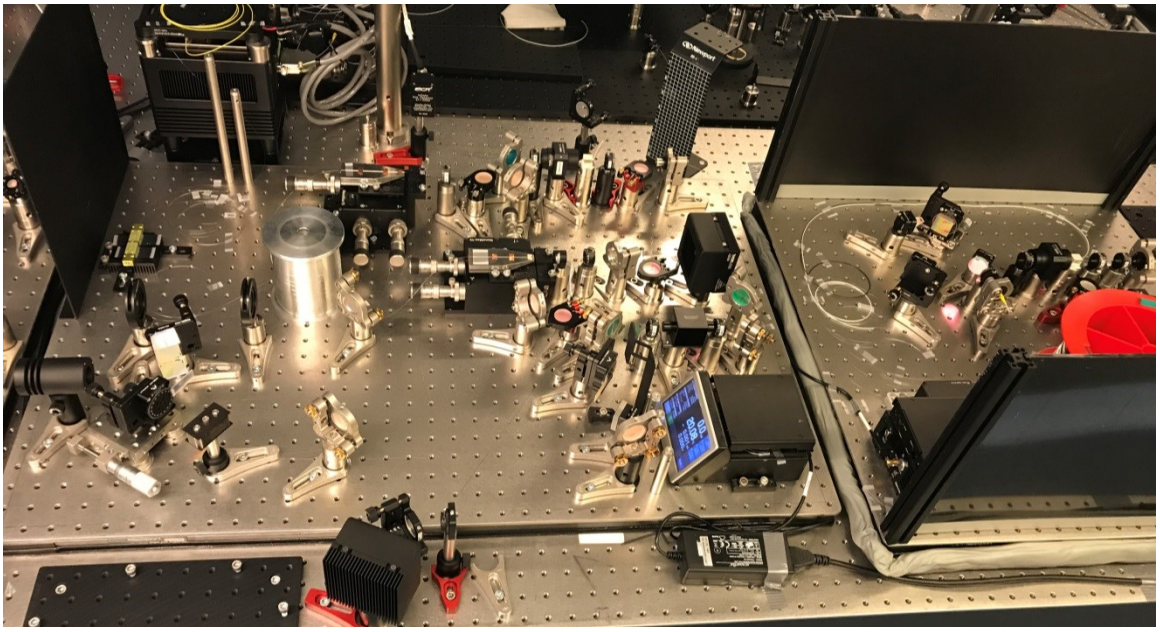

Fig. 3. 15. Picture of the high power Yb-fiber laser system.

Chapter 4

Self-phase modulation enabled tunable ultrafast fiber laser source towards 1.3 μm

4.1 Introduction

Femtosecond sources operating in the 800-1300 nm wavelength range have received a lot of attention because they are an enabling technology to drive multiphoton microscopy for biomedical imaging [59-62]. The wavelength range at the longer wavelength side (e.g., 1150-1300 nm) is of particular importance for deep tissue imaging thanks to an optimal combination of low water absorption and reduced light scattering [63]. Meanwhile, less photon energy at longer wavelengths causes less potential photo-damage to the sample. Due to the loss from microscope optics, femtosecond pulses with >10-nJ pulse energy are usually desired in the range 1100-1300 nm. The state-of-the-art Cr:forsterite oscillator based on Kerr-lens mode-locking can directly emit femtosecond pulses with 16.5-nJ pulse energy [64]. Unfortunately, the gain bandwidth of Cr:forsterite crystals limits the emitted pulses to the wavelength range of 1230-1250 nm. Optical parametric oscillators pumped by solid-state lasers can fulfill the requirements on wavelength coverage as well as pulse energy; however, high complexity, high cost, and large size of such solid-state laser solutions has limited their deployment mostly to research laboratories.

As we have discussed in Chapter 2, output pulses from an ultrafast fiber laser can be continuously wavelength red-shifted using soliton self-frequency shift (SSFS) inside an optical fiber—a phenomenon that originates from stimulated Raman scattering. To form Raman soliton, SSFS requires negative group-velocity dispersion (GVD). Because standard single-mode fibers (SMFs) have the typical zero-dispersion wavelength (ZDW) around ~1300 nm for the fundamental mode, generation of Raman soliton needs the center wavelength of input pulses larger than ~1300 nm. In order to obtain Raman soliton from an

ultrafast Yb-fiber laser at 1030 nm, PCFs with a small (< 3μm) mode-field diameter (MFD) are usually employed to shift the ZDW below 1030 nm [65, 66]. As we have shown in Chapter 2, these PCFs feature strong nonlinearity, which limits the resulting wavelength-converted pulses to <1 nJ in pulse energy [12, 13, 15]. With a careful design, a multi-mode optical fiber may accommodate robust higher-order-modes (HOMs) that exhibit both negative GVD in the wavelength range of 1000-1300 nm and much large MFD than the fundamental mode. These two unique features benefit SSFS pumped by Yb-fiber lasers producing 200-fs pulses tunable between 1064 and 1200 nm with 1-2 nJ pulse energy [21]. Recently, a Raman soliton source at 1317 nm with 30 nJ pulse energy was demonstrated employing $LP_{0,9}$ mode [67]. However, excitation of the $LP_{0,9}$ mode required a spatial light modulator, and an axicon was used at the fiber output to convert the $LP_{0,9}$ mode to a Gaussian-like beam profile, which significantly increases the system complexity.

Recently, self-phase modulation (SPM) enabled ultrafast fiber laser sources are demonstrated featuring a wide wavelength tuning range from 825 nm to 1210 nm with >1 nJ pulse energy [54]. SPM inside a short passive fiber broadens an input optical spectrum and generates isolated spectral lobes. Using optical band-pass filters to select the leftmost or rightmost spectral lobes produces nearly transform-limited pulses with ~100 fs duration. In the previous demonstration, the employed photonic crystal fiber (PCF) exhibits a dispersion of <18 ps/nm/km in the 900-1200 nm wavelength range, which results in a remarkable tuning range of 825-1210 nm for the SPM-enabled source [54]. However, such a low-dispersion PCF possesses a small mode-field diameter (MFD) of only 2.2 μm and the resulting strong nonlinearity limits the pulse energy in 1150-1210 nm to be ~3 nJ. Recently, our group demonstrated the use of a large mode-area (LMA) fiber with a 7.5-μm MFD for this process to dramatically increase the pulse energy beyond 10 nJ [68]. Limited by the available laser power and the zero-dispersion wavelength (ZDW) of the LMA fiber, this energy scaling only succeeds for the wavelength below 1200nm; at 1150 nm, the pulse energy is still less than 10 nJ.

In this chapter, we employ the high-power Yb-fiber laser system developed in Chapter 3 as the driving source and derive a widely tunable source delivering femtosecond laser pulses wavelength toward 1.3 μm with up to 16.5-nJ pulse energy. Such a source will be used in Chapter 5 to provide the signal pulses for difference-frequency generation to obtain high-power ultrafast mid-infrared pulses.

4.2 Schematic of experimental setup

Figure 4.1 illustrates the experimental setup of SPM enabled fiber laser source beyond 1.2 μm. The home-built high-power Yb-fiber laser produces 165-fs pulses with 14.5-W average power, corresponding to 480-nJ pulse energy. More details are given in Chapter 3 on the implementation of this Yb-fiber laser system.

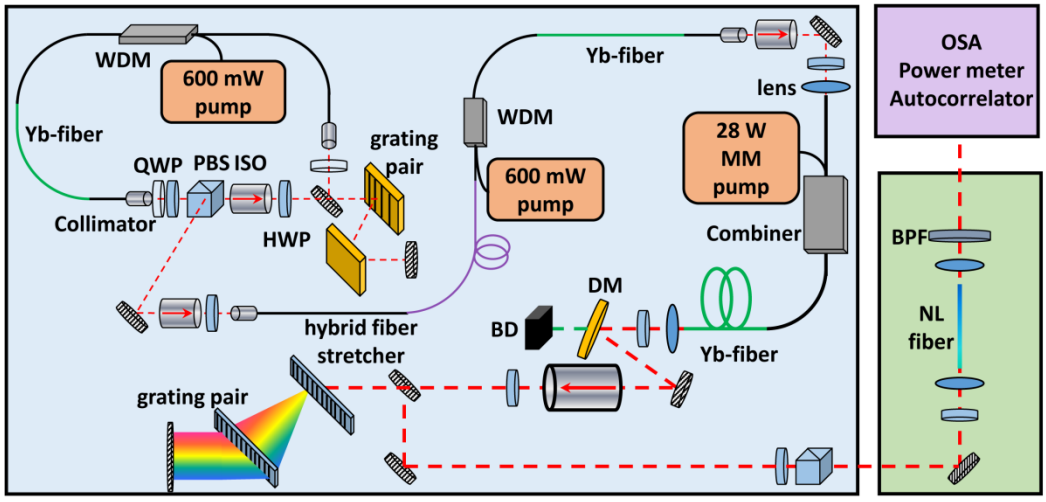

Fig. 4. 1. Schematic setup of SPM-enabled tunable ultrafast fiber laser source. WDM: wavelength division multiplexer, QWP: quarter wave plate, HWP: half wave plate, PBS: polarization beam splitter, ISO: isolator, DM: dichroic mirror, BD: beam dumper, BPF: bandpass filter, OSA: optical spectrum analyzer.

We use a half-wave plate (HWP) together with a polarization beam splitter (PBS) to continuously adjust the power coupled into a short piece of optical fiber for spectral broadening. Both ends of the fiber are 8-degree angle cleaved. A 10X Eye Loupe (Thorlabs, Inc.) is utilized to adjust the fiber position placed in the V-groove fiber holder (HFV001). The oblique plane of cleaved fiber is kept vertical to improve the coupling efficiency. Several aspheric lenses are employed to maximize coupling efficiency. The output pulses are collimated by an aspheric lens (8-mm focal length). We use a wedged window (made of UV fused silica) to split the output pulses. Reflected pulses with 4% of total output power are utilized to monitor the SPM-enabled spectral broadening. We use an optical bandpass filter to select the rightmost spectral lobe of the transmitted pulses; the resulting pulse train is diagnosed by an optical spectrum analyzer (OSA), a power meter, and an autocorrelator.

4.3 Generation and characterization of filtered pulses

Propagation of an ultrashort pulse inside an optical fiber can be well modeled by the generalized nonlinear Schrödinger (GNLS) equation.

$$\frac{\partial A}{\partial z}+\frac{\alpha}{2}A+\frac{i\beta_2}{2}\frac{\partial^2 A}{\partial T^2}-\frac{\beta_3}{6}\frac{\partial^3 A}{\partial T^3}=i\gamma\left(|A|^2A+\frac{i}{\omega_0}\frac{\partial}{\partial T}(|A|^2A)-T_RA\frac{\partial|A|^2}{\partial T}\right) \tag{4.1}$$

A is short for $A(z,t)$, which denotes the propagating pulse envelope. β_n represents the n-th order fiber GVD and γ accounts for the nonlinear coefficient. The nonlinear coefficient is given by

$$\gamma(\omega_0)=\frac{\omega_0 n_2}{cA_{eff}}, \tag{4.2}$$

where ω_0 is pulse center frequency, c light speed in vacuum, and n_2 the nonlinear-index coefficient of fused-silica material. The typical value of n_2 is $2.4\times10^{-20}\ m^2W^{-1}$. A_{eff} denotes the effective mode-field area defined as

$$A_{eff}=\pi w^2. \tag{4.3}$$

The MFD w depends mainly on the V parameter of the fiber. T_R is the Raman response defined as

$$T_R=\int_0^\infty tR(t)dt. \tag{4.4}$$

$R(t)$ is given by

$$R(t)=(1-f_R)\delta(t)+f_R\frac{(\tau_1^2+\tau_2^2)}{\tau_1\tau_2^2}\exp\left(\frac{-t}{\tau_2}\right)\sin\left(\frac{t}{\tau_1}\right). \tag{4.5}$$

$R(t)$ describes the nonlinear response, including both electronic and nuclear contributions. Typical values for these parameters are $f_R=0.18$ fs, $\tau_1=12.2$ fs, and $\tau_2=32$ fs, respectively [8]. The GNLS equation is a nonlinear partial differential equation and can be numerically solved by the split-step Fourier method [8]. Since we only focus on the SPM effect, we neglect other effects such as dispersion, self-steepening, and stimulated Raman scattering and simplify Eq. (4.1) as

$$\frac{\partial A}{\partial z}=i\gamma|A|^2A \tag{4.6}$$

Equation (4.6) has an analytical solution $A(z, t) = A(0, t)exp(i\gamma|A|^2z)$, which shows that the pulse envelope remains unchanged along the propagation distance. However, the pulse acquires a phase term proportional to the pulse power $|A|^2$ and propagation length z. Such a nonlinear phase leads to a broadened optical spectrum with well-isolated spectral lobes [54].

As a Kerr nonlinearity effect, SPM was discovered in 1967 during the investigation of self-focusing of optical pulses propagating in CS_2-filled cell [8]. However, the first time to observe SPM in optical fiber was in1978 during the study of pulse propagating inside optical fibers with core filled with CS_2 liquid [8]. In this chapter, we test seven different fibers for SPM-enabled spectral broadening followed by spectral filtering. The properties of these fibers (such as ZDW, dispersion, MFD, and nonlinear coefficient γ) are all listed in Table 4.1. All the parameters are given at the wavelength of 1064 nm.

Table 4. 1 Properties of optical fibers used in spectra broadening

Fiber type	ZDW nm	MFD μm	γ $W^{-1}km^{-1}$
HI-1060	1310	5.8	5.3
SMF-28	1313	8.0	2.8
LMA-8	1160	7.5	3.2
LMA-PM-10	1180	8.6	2.4
ESM-12B	1215	10.3	1.7
LMA-PM-15	1230	12.6	1.1
LMA-20	1243	16.5	0.7

We first use HI-1060 and SMF-28 for the preliminary test. In the previous simulation shown in [54], the broadened spectrum is proportional to the propagating fiber length. As a result, two different fiber lengths, 9-cm and 4-cm, are chosen to compare. A 3-Axis NanoMax Flexure Stage (Thorlabs Inc.) and an aspheric lens are utilized to couple the excitation 1030-nm pulses into the fiber. Several aspheric lenses are employed to maximize the coupling efficiency at relative low average power of 100 mW. The aspheric lens with 8-mm focus length gives the maximum coupling efficiency of 72%. Both of the fiber ends are cleaved with an 8-degree angle.

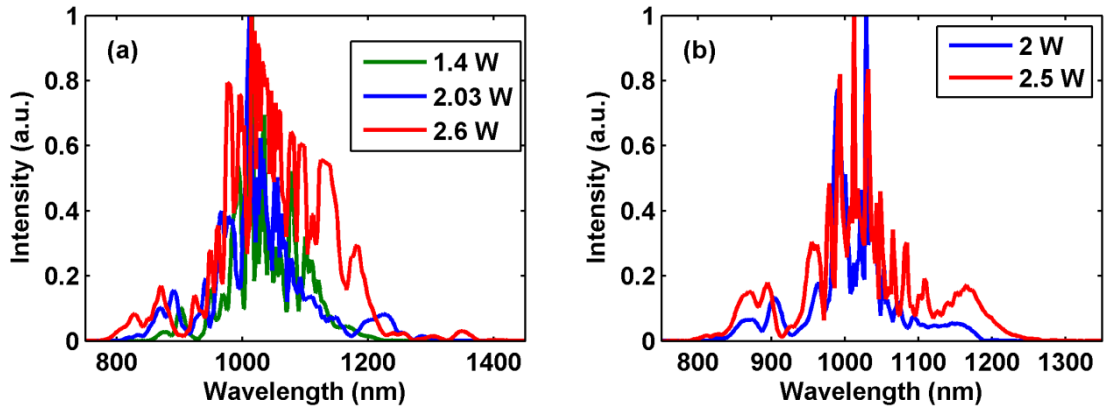

Fig. 4. 2. (a) Spectra generated by 9-cm HI-1060 at different coupled power. (b) Spectra generated by 4-cm HI-1060 at different coupled power.

As shown in Fig. 4.2, the output spectrum is significantly broadened with the increase of coupled average power. We experimentally found that the fiber input facet is damaged once the coupled power exceeds 2.7 W. As a result, the coupled power into the fiber core drops dramatically, which destroys spectra broadening. Under the same amount of coupled power, 9-cm HI-1060 fiber leads to much broader spectrum than 4-cm fiber can generate. However, shorter fiber has less dispersion such that SPM becomes a more dominant mechanism for spectral broadening. As a result, the broadened optical spectra using the shorter fiber are less structured.

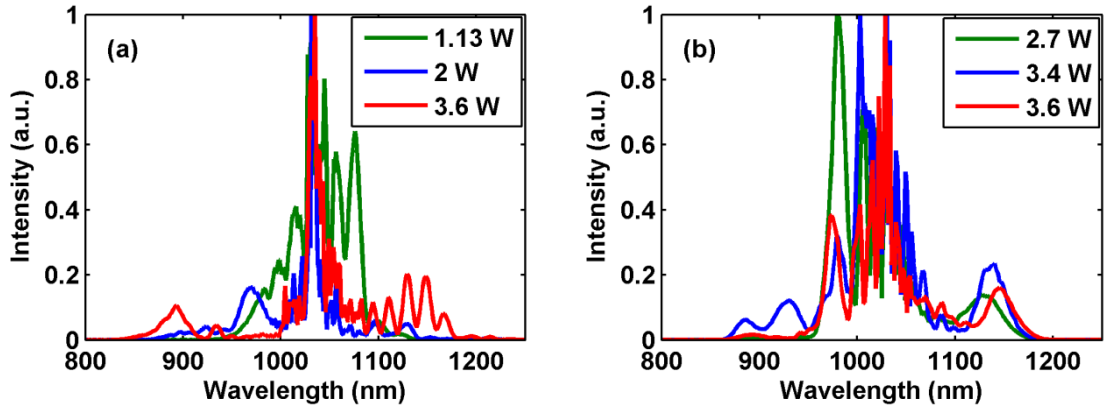

Fig. 4. 3. (a) Broadened spectra by 9-cm SMF-28. (b) Broadened spectra by 4-cm SMF-28.

Figure 4.3(a) and (b) show the broadened spectra from 9-cm and 4-cm SMF-28, respectively. Using the aspheric lens with 8-mm focus length, the maximum coupling efficiency is 71%. The maximum average power coupled into SMF-28 is 3.6 W to prevent fiber damage.

Apparently the damage threshold is higher for SMF-28 compared with HI-1060 because the former has a larger MFD.

The experimental results from HI-1060 and SMF-28 suggest that larger MFD fibers are preferred for energy scaling the SPM-enabled spectral broadening. We then test large-mode-area (LMA) fibers: LMA-8 and LMA-PM-10. Both of these two fibers (from Thorlabs) are 4 cm long.

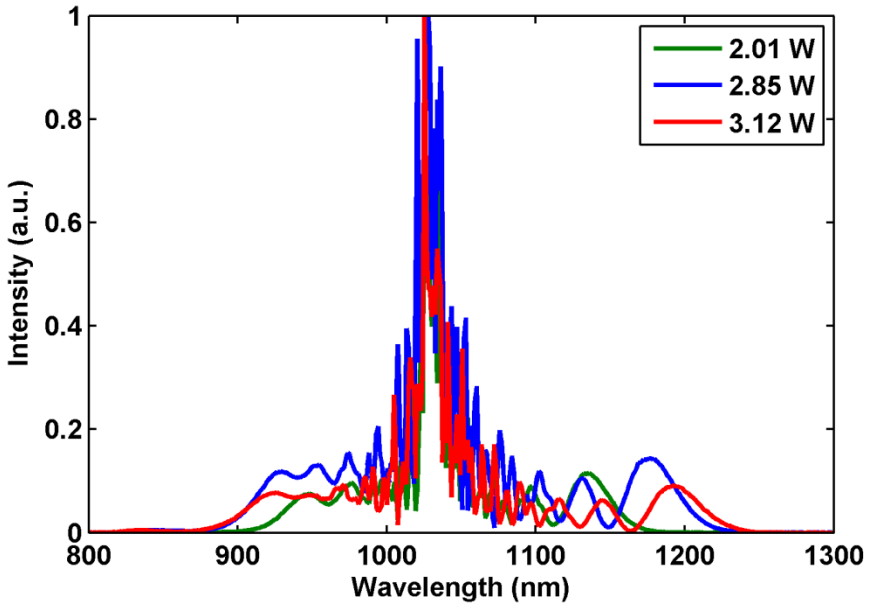

Fig. 4. 4. Broadened spectra given by 4-cm LMA-8.

Figure 4.4 plots the broadened spectra in 4-cm LMA-8 fiber at the coupled power of 2.01 W, 2.85 W, and 3.12 W. The maximum coupling efficiency of 76.1% is obtained by utilizing aspheric lens with 11-mm focal length. More power leads to broader spectrum. The rightmost spectral lobe can be continuously tuned from 1100 nm to 1200 nm. With 3.12-W coupled power, the broadened spectrum has the rightmost spectral lobe peaking at 1195 nm. We use a band-pass filter to filter the rightmost spectral lobe and measure its average power. The band-pass filter (Edmund Optics Ltd) has the center wavelength at 1225-nm with 25-nm bandwidth and >90% transmission. By carefully tuning the incident angle on the band-pass filter, the center wavelength of transmission can be tuned from 1225 nm to 1250 nm. The filtered spectrum lobe peaking at 1195 nm has 30-nm bandwidth and 311-mW average power, corresponding to 10 nJ pulse energy. Given that the coupled power is 3.12 W, ~10% conversion efficiency is achieved.

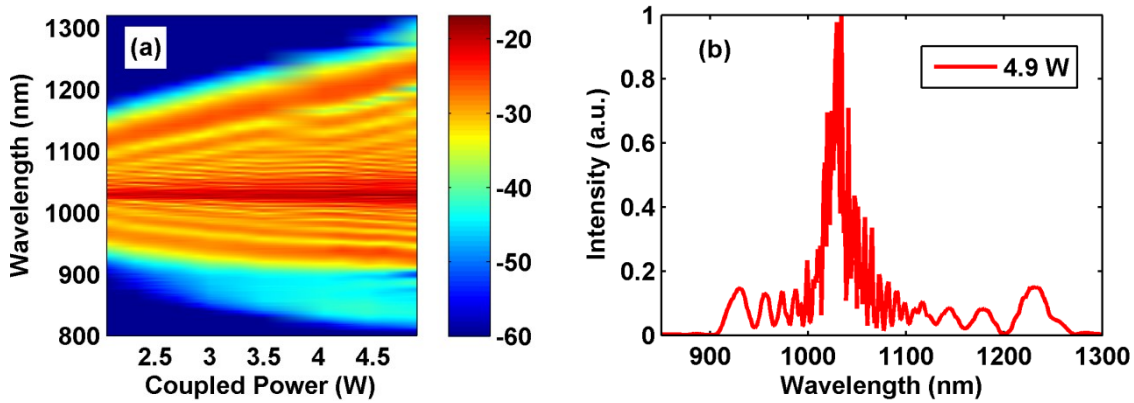

Fig. 4. 5. SPM-enabled spectral broadening in 4-cm LMA-PM-10. (a) Spectra versus coupled average power. Spectral intensity is shown on a logarithm scale. (b) Broadened spectrum at 4.9-W coupled power.

LMA-PM-10 fiber has larger MFD than LMA-8 and therefore requires a coupling lens with longer focal length. The maximum coupling efficiency is 62.6%, obtained employing aspheric lens C260TMD-B (15.29-mm focal length and 0.16 NA). Because LMA-PM-10 is a polarization-maintaining fiber, a HWP is placed in front of the input of the fiber to adjust the polarization of coupling pulses. An OSA is employed to monitor the output spectrum of 4-cm LMA-PM-10 fiber. We rotate the HWP to generate the broadest spectrum and the associated coupling efficiency may drop a bit. As shown in Fig. 4.5(a), the center wavelength of the leftmost spectral lobe can be shifted to 920 nm, which is exactly the desired wavelength for the two photon absorption bio-imaging of biomedical samples labeled by green fluorescent proteins [69-71]. The distinct structure of multi spectral lobes indicates that SPM constitutes the main broadening mechanism. The rightmost spectral lobes can fully cover the wavelength range from 1100 nm to 1230 nm.

The same filter utilized in LMA-8 fiber study is also employed to filter the spectral lobes. At 3.5-W coupled power, the filtered spectral lobe centers at 1170-nm with a bandwidth of 36 nm and 380-mW average power, corresponding to 13 nJ pulse energy. As the coupled power is increased to 4.6 W, the rightmost spectral lobe shifts to 1207-nm, which after filtering exhibits 35-nm bandwidth with 360-mW average power, corresponding to 12 nJ pulse energy. At the coupled power of 4.9 W, the entire spectrum spans from 920 nm to 1230 nm, which is depicted in Fig. 4.5(b). Fiber input facet is damaged as the coupled power exceeds 5 W.

The results from LMA-8 and LMA-PM-10 fibers indicate that using fibers with larger diameter and shorter length benefit this SPM-enabled spectral selection (SESS) approach to generate tunable femtosecond pulses. To systematically study the effect of mode area and fiber length, we further compare three fibers: LMA-PM-10, ESM-12B, and LMA-PM-15, all commercially available from Thorlabs, Inc. MFDs of these three fibers at 1064 nm are 8.6 μm, 10.3 μm, and 12.6 μm, respectively. The fiber length is set to be 4 cm and 6 cm.

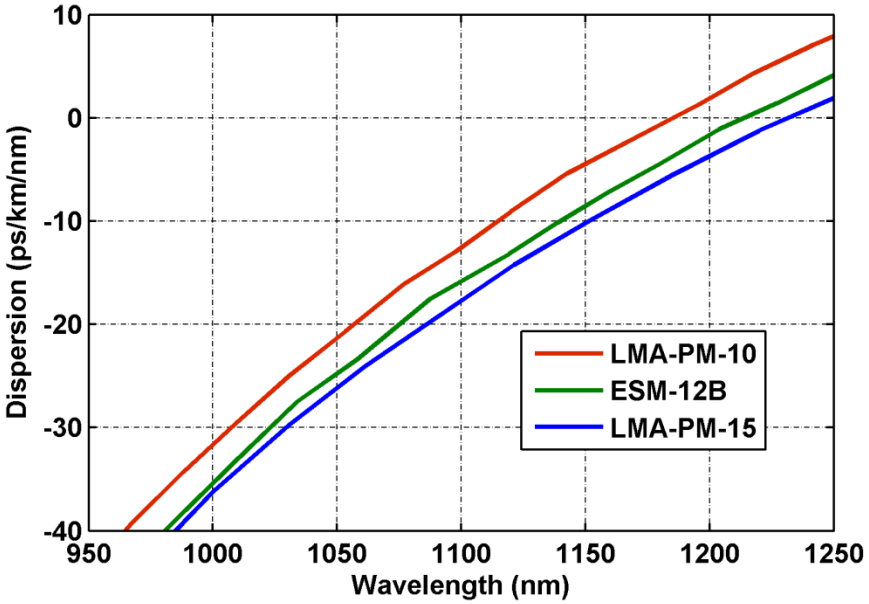

Fig. 4. 6. Dispersion curves of three LMA fibers: LMA-PM-10, ESM-12B, and LMA-PM-15.

Figure 4.6 shows the dispersion curves of these three fibers. LMA-PM-15 has the largest dispersion among three LMA fibers. These fibers have different ZDWs: 1180 nm for LMA-PM-10, 1215 nm for ESM-12B, and 1230 nm for LMA-PM-15. A band-pass filter is placed after the collimated beam. Slightly tuning the incident angle on the band-pass filter could shift the center wavelength of the filtered spectrum. To compare the energy scaling performance of these fibers, all the three fibers are chosen to be 6 cm long at the beginning. We vary the coupling power into each fiber such that the rightmost spectral lobe roughly peaks at 1200 nm or 1225 nm. The rightmost spectra lobe is filtered and measured by a power meter and an intensity autocorrelator (FR-103XL, Femtochrome Research, Inc.).

Figure 4.7 summarizes the experimental results using 6-cm LMA-PM-10. The blue curve and the red curve in Fig. 4.7(a) plot the measured overall spectra at the coupled power of 2.49 W and 2.73 W, respectively; the filtered rightmost spectral lobes are shown in Fig. 4.7(b). These

two filtered spectral lobes peak at 1200 nm and 1225 nm with the average power of 315 mW (5.1 nJ pulse energy) and 335 mW (5.6 nJ pulse energy), respectively. The conversion efficiency is 12%. Figure 4.7(c, d) plot the measured auto-correlation traces for the filtered spectra center at 1200 nm and 1225 nm. The black curves in these two figures represent the calculated autocorrelation traces for the transform-limited pulses corresponding to the filtered spectra. The filtered pulse duration of pulse centered at 1200 nm and 1225 nm is 114 fs and 162 fs. Corresponding transform-limited pulse duration is estimated to be 83 fs and 85 fs, respectively. The pulse centered at 1200 nm is slightly longer than the transform-limited pulse while the pulse at 1225 nm has a duration nearly twice the transform-limited pulse.

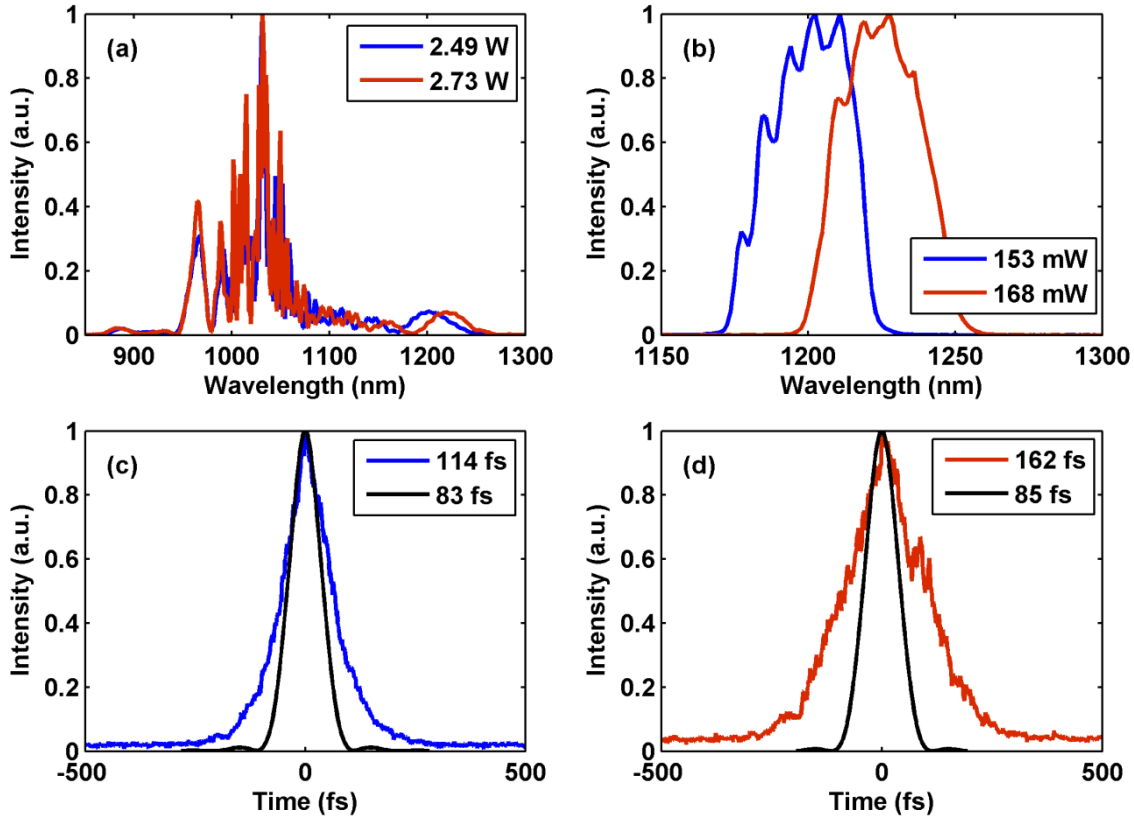

Fig. 4. 7. (a) Output optical spectra from 6-cm LMA-PM-10. (b) Filtered spectra peaking at 1190 nm and 1225 nm. (c, d) Autocorrelation traces for the filtered spectra. Black curves: calculated autocorrelation traces of the transform-limited pulses allowed by the filtered spectra.

We continue to characterize the filtered pulses generated by 6-cm fiber ESM-12B. Figure 4.8(a) plots the measured overall spectra at the coupled power of 3.75 W and 4.37 W, respectively. The filtered rightmost spectral lobes peak at 1200 nm and 1225 nm (Fig. 4.8(b)) with an average power of 230 mW (7.7-nJ pulse energy) and 240 mW (8.0-nJ pulse energy), respectively. The pulse energy obtained from 6-cm fiber ESM-12B is larger than acquired

from 6-cm fiber LMA-PM-10 for the pulse peaking at the same center wavelength. As Fig. 4.8(c, d) shows, the pulse duration at 1200 nm (1225 nm) is 92 fs (177 fs).

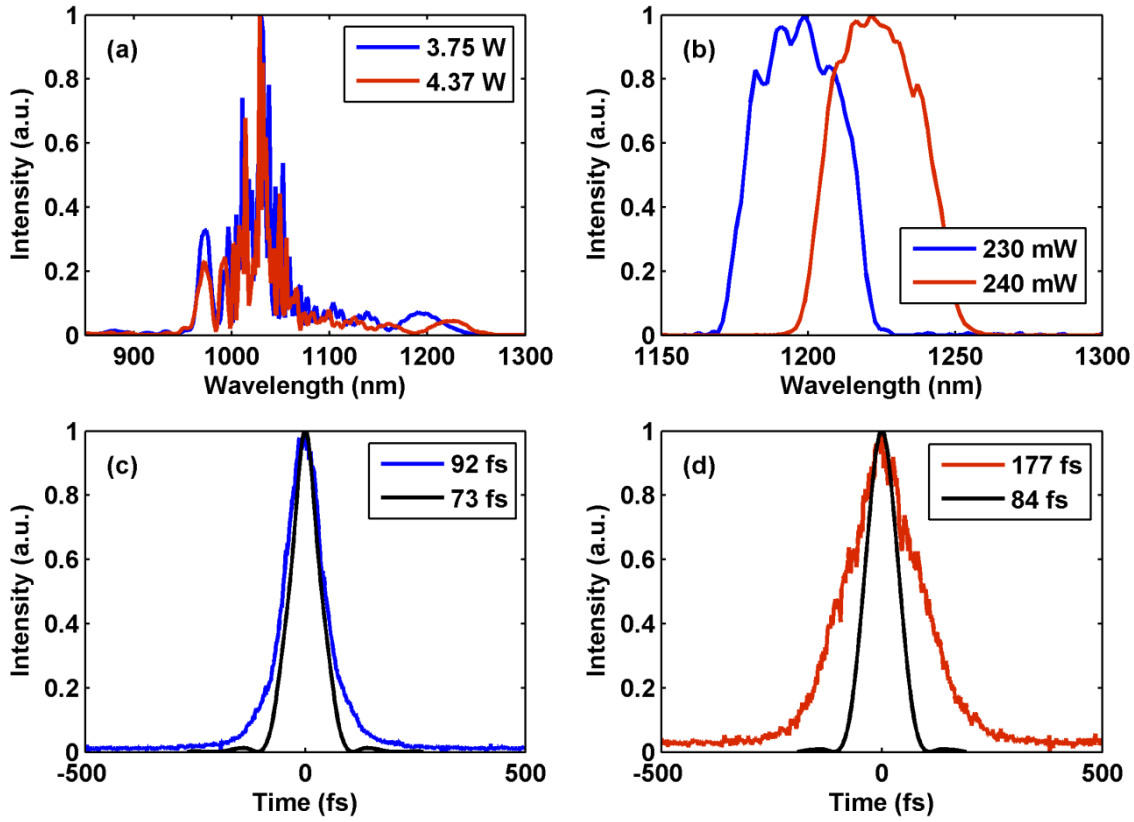

Fig. 4. 8. (a) Output optical spectra from 6-cm ESM-12B. (b) Filtered spectra peaking at 1190 nm and 1225 nm. (c, d) Autocorrelation traces for the filtered spectra. Black curves: calculated autocorrelation traces of the transform-limited pulses allowed by the filtered spectra.

Figure 4.9 summarizes the experimental results using 6-cm LMA-PM-15. More power (5.54 W and 6.5 W) is required to broaden the spectrum such that the generated rightmost spectral lobes peak at 1200 nm and 1225 nm (Fig. 4.9(a)). The filtered spectral lobe (Fig. 4.9(b)) has an average power of 315 mW at 1200 nm and 335 mW at 1225 nm, corresponding to pulse energy of 10.5 nJ and 11.2 nJ, respectively. The measured duration is 88 fs and 160 fs for pulses centered at 1200 nm and 1225 nm (Fig. 4.9(c,d)).

A comparison of experimental results shown in Fig. 4.7-4.9 concludes that higher pulse energy is achieved for the filtered spectral lobe generated by a fiber with larger MFD. More specific, the pulse energy for the spectra lobe peaking at 1200 nm (1225 nm) is 5.1 nJ (5.6 nJ) for LMA-PM-10, 7.7 nJ (8.0 nJ) for ESM-12B, and 10.5 nJ (11.2 nJ) for LMA-PM-15.

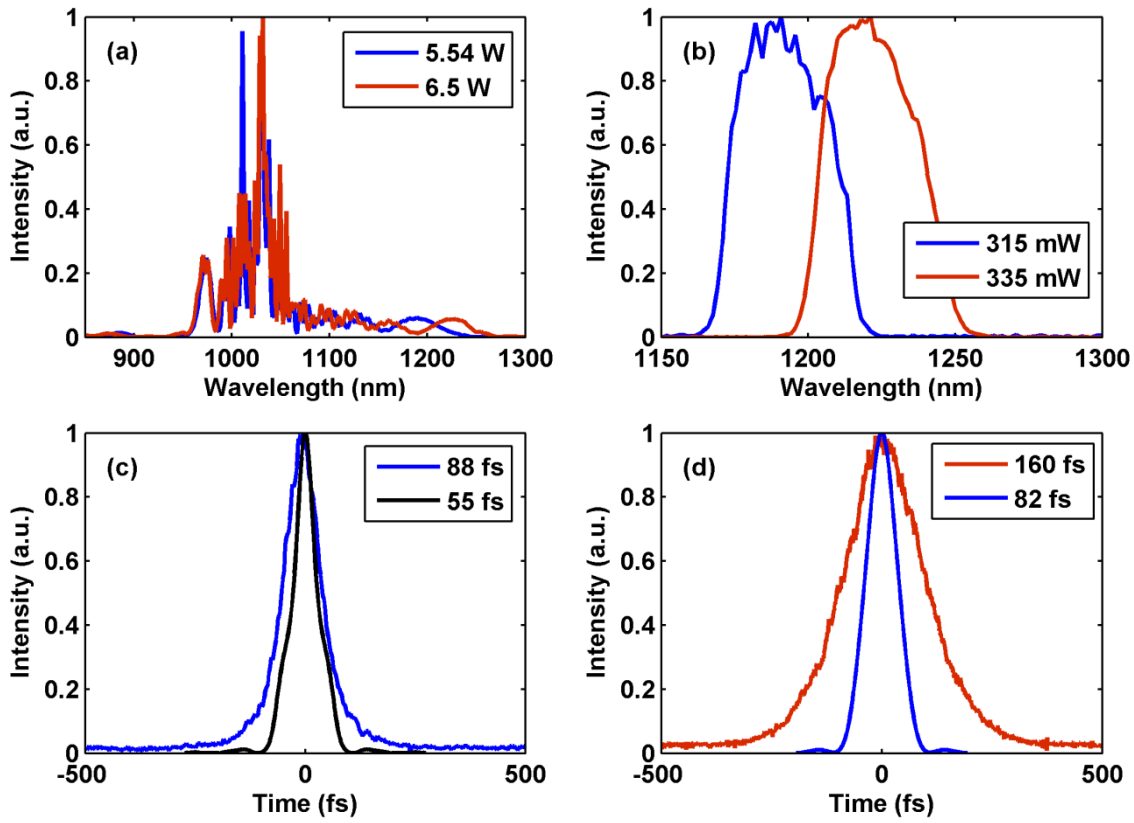

Fig. 4. 9. (a) Output optical spectra from 6-cm LMA-PM-15. (b) Filtered spectra peaking at 1200 nm and 1225 nm. (c, d) Autocorrelation traces for the filtered spectra. Black curves: calculated autocorrelation traces of the transform-limited pulses allowed by the filtered spectra.

For further scale the pulse energy, we reduced the fiber length from 6 cm to 4 cm. Consequently, more power needs to be coupled into the fiber to achieve the same amount of spectra broadening. As a result, the filtered spectral lobe has more pulse energy. The experimental results obtained from 4-cm LMA-PM-10, ESM-12B, LMA-PM-15 are presented in Fig. 4.10, Fig. 4.11, and Fig. 4.12, respectively. More specific, the pulse energy for the spectra lobe peaking at 1200 nm (1225 nm) is 10.5 nJ (10.9 nJ) for LMA-PM-10, 13.7 nJ (14.3 nJ) for ESM-12B, and 16 nJ (16.5 nJ) for LMA-PM-15. From the measured autocorrelation traces, we notice that the filtered pulses are always noticeably longer than the transform-limited pulses. A possible explanation is that the initial pump pulse is not pedestal-free, and some nonlinear phase is inherited by the filtered pulses.

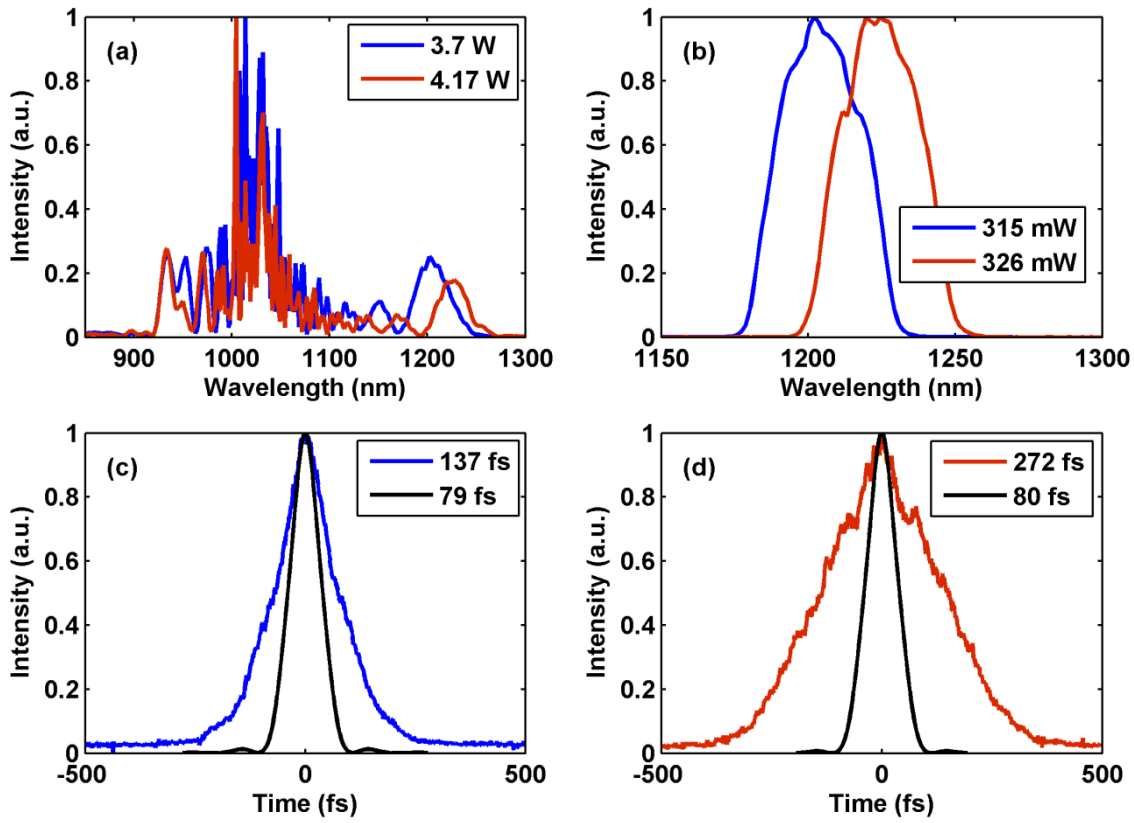

Fig. 4. 10. Experimental results from 4-cm LMA-PM-10. (a) Output optical spectra at different power. (b) Filtered spectra peaking at 1200 nm and 1225 nm. (c, d) Autocorrelation traces for the filtered spectra. Black curves: calculated autocorrelation traces of the transform-limited pulses allowed by the filtered spectra.

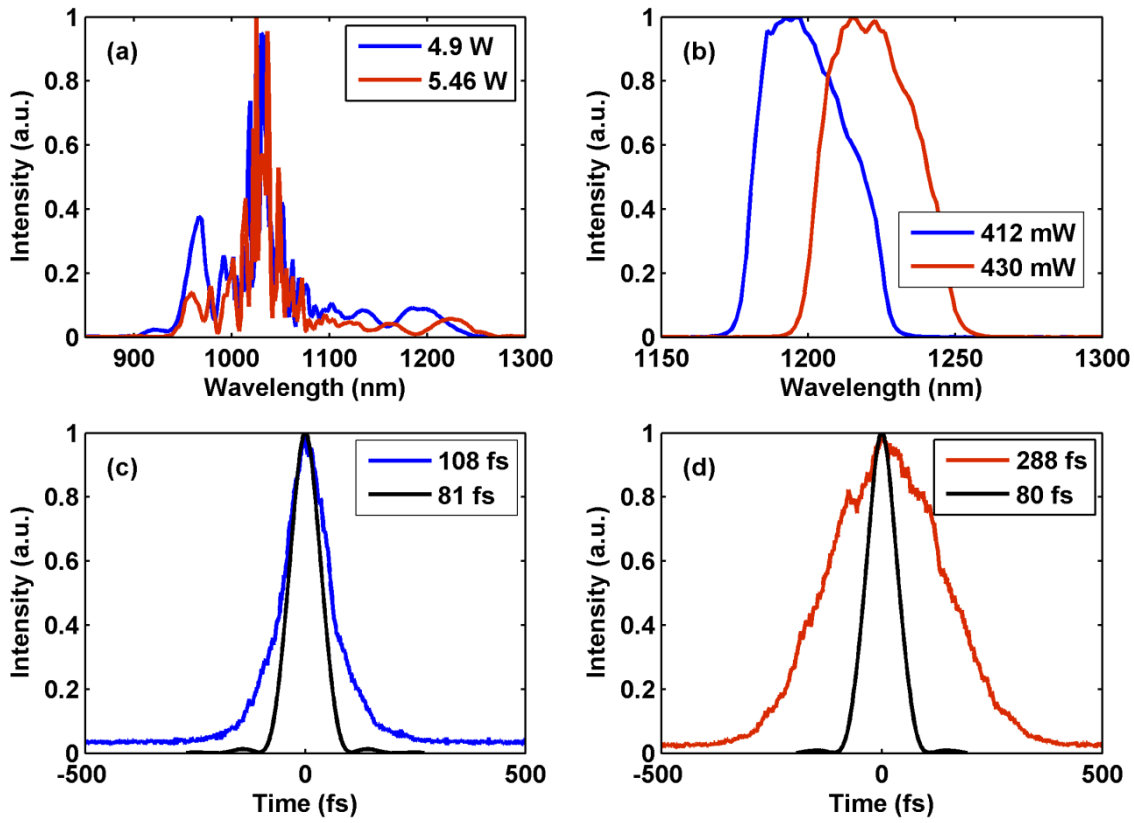

Fig. 4. 11. Experimental results from 4-cm ESM-12B. (a) Output optical spectra at different power. (b) Filtered spectra peaking at 1200 nm and 1225 nm. (c, d) Autocorrelation traces for the filtered spectra. Black curves: calculated autocorrelation traces of the transform-limited pulses allowed by the filtered spectra.

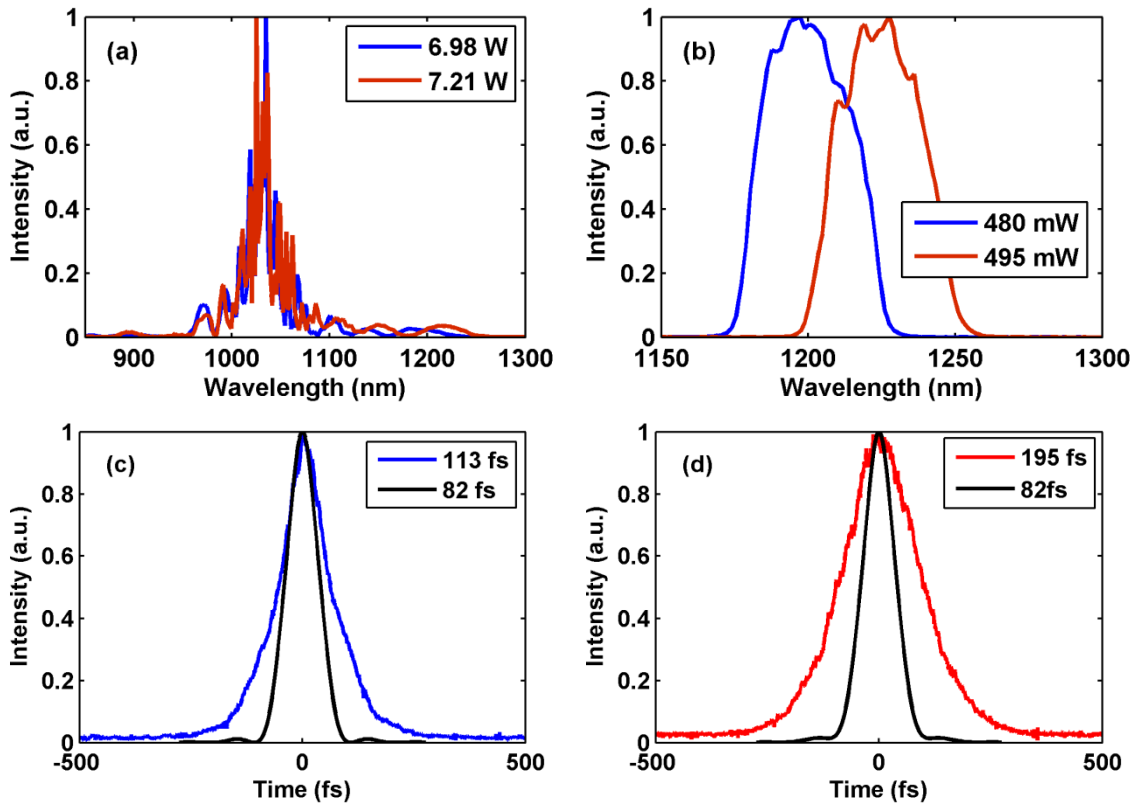

Fig. 4. 12. Experimental results from 4-cm LMA-PM-15. (a) Output optical spectra at different power. (b) Filtered spectra peaking at 1200 nm and 1225 nm. (c, d) Autocorrelation traces for the filtered spectra. Black curves: calculated autocorrelation traces of the transform-limited pulses allowed by the filtered spectra.

4.4 Conclusion

We construct a high power Yb-fiber laser system to investigate the energy scalability of SPM-enabled ultrafast sources. Using LMA fibers, we show that SPM-enabled spectral broadening followed by spectral filtering can generate ultrashort pulses with up to 16.5-nJ pulse energy at the wavelength of 1225 nm. The source can be further red shifted to a wavelength beyond 1250 nm. We believe that >20 nJ femtosecond pulses with wavelength tunable over the entire 1200-1300 nm band can be achieved.

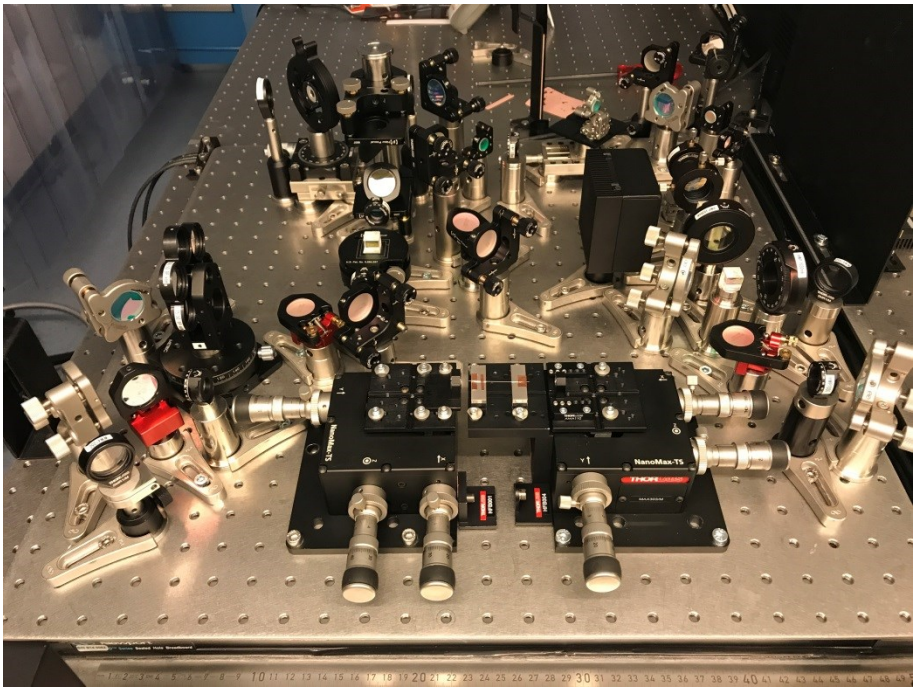

Fig. 4. 13. The experimental setup of SPM-enabled tunable ultrafast sources.

Figure 4.13 shows the whole experimental setup of the SPM enabled tunable ultrafast fiber laser source. The whole setup is placed on a 600 mm × 600 mm size breadboard.

Chapter 5

High average power, widely tunable, DFG-based mid-IR source

5.1 Introduction

Difference frequency generation (DFG) between two synchronized femtosecond pulses that are derived from the same ultrafast near-IR source is another popular approach to generated ultrafast mid-IR pulses. For instance, 4.3-mW mid-IR pulses centered at 13.2 μm are obtained through DFG between two OPO generated signals in a 3-mm $AgGaSe_2$ [72]. DFG between the outputs of a two color Yb: fiber chirped-pulse amplifier in 1-mm GaSe crystal produces 1.5-mW mid-IR pulses at 18 μm [73]. The wavelength tunability of generated mid-IR pulses is determined by the wavelength difference between the signal pulse and the pump pulse. The pump pulse is normally obtained from ultrafast mode-locked lasers and consequently the center wavelength of the pump pulse is fixed by the gain material in these lasers. Therefore a signal pulse with its center wavelength widely tunable is necessary to implement a widely tunable mid-IR source via DFG. Such a signal pulse can be obtained using fiber-optic stimulated Raman scattering (SRS) [74]. As we have shown in Chapter 2, SRS continuously red-shifts an input pulse's center wavelength with increasing the input power when the pulse propagates inside an optical fiber with negative group-velocity dispersion (GVD). The resulting Raman soliton source is tightly synchronized with its pumping pulse. SRS preserves the carrier-envelope phase offset and hence renders the red-shifted Raman soliton pulse train to share the same frequency offset f_{CE} with its pumping pulses. DFG between these two-color pulse sources cancels the frequency offset f_{CE}, leaving

only one degree-of-freedom— f_R (i.e., pulse repetition rate)—to determine the resulting mid-IR frequency comb.

Many groups have used Raman soliton as the signal pulse for DFG to implement tunable mid-IR sources [75-78]. Raman solitons with the wavelength tuning from 1.15 μm to 1.6 μm have been generated in a 25-cm highly nonlinear suspended-core fiber pumped by a 2.2-W, 151-MHz Yb-fiber laser comb source. DFG between the Raman soliton pulses and the residual pump pulses in a 0.5-mm GaSe crystal and a 4-mm PPLN crystal generates mid-IR pulses tunable from 3 μm to 10 μm with the average power up to 1.5 mW (10 pJ pulse energy) [78]. Limited by the nonlinearity and dispersion, a Raman soliton pulse normally has the pulse energy less than 1 nJ; as a result, the pulse energy of the generated mid-IR pulse is limited to tens of pico-joule level.

In Chapter 3, we demonstrated a 14.5-W Yb fiber CPA system centered at 1.03 μm. The femtosecond pulses emitted by this laser source were coupled into a short piece of large mode-area (LMA) fiber for SPM-enabled spectral selection (SESS). In this chapter, we employ the 1.03-μm pulse as the pump and the SESS source as the signal, and implement a DFG-based mid-IR source. The mid-IR source can be tuned from 7.4 μm to 16.8 μm with up to 5-mW (~170 pJ pulse energy) at 11 μm. To the best of our knowledge, this mid-IR system delivers the highest pulse energy at such high repetition rate among all reported DFG-based mid-IR sources.

5.2 Schematic of the experimental setup

Figure 5.1 illustrates the experimental setup that includes two major parts: the high power Yb-fiber CPA system and the mid-IR generation system. As discussed in Chapter 4, the Yb-fiber CPA system delivers 165-fs pulses with 14.5-W average power at 30-MHz repetition rate, corresponding to 480-nJ pulse energy. The laser output is split into two arms by a half-wave plate (HWP) together with a polarization beam splitter (PBS). The pulses at one arm are coupled into a piece of LMA fiber for SPM-enabled spectra broadening, followed by a band-pass filter to generate tunable femtosecond signal pulses. The pulses at the other arm serve as the pump pulses for the following DFG in a GaSe crystal. A HWP together with a PBS continuously adjust the optical power employed in DFG. An optical delay line and a

telescope ensure both temporal and spatial overlap between the pump pulses and the signal pulses in the GaSe crystal.

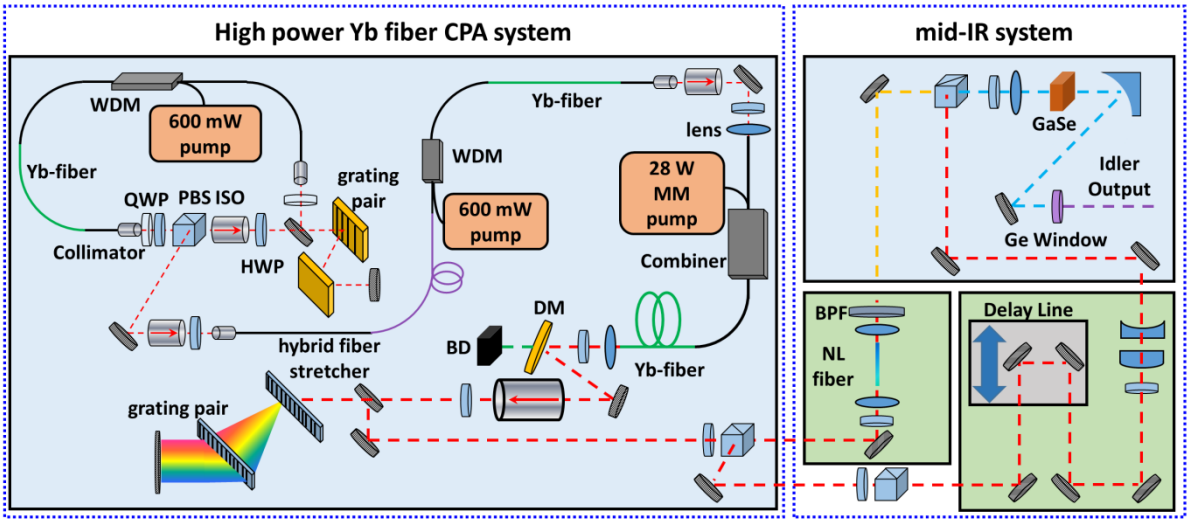

Fig. 5. 1. Schematic setup of high-power, widely tunable DFG-based mid-IR source. WDM: wavelength division multiplexer, QWP: quarter-wave plate, HWP: half-wave plate, PBS: polarization beam splitter, ISO: isolator, DM: dichroic mirror, BD: beam dumper, NL fiber: nonlinear fiber, BPF: bandpass filter.

The pump pulses and signal pulses are collinearly combined by a broadband PBS. An achromatic HWP (1000 – 1700 nm) is employed to adjust the polarization of both signal and pump pulses. The combined pulses are focused into the GaSe crystal (GaSe-2000H1, EKSMA OPTICS) by a plano-convex lens (LA1251-C, Thorlabs Inc.) with 100-mm focal length. The focal spot size is estimated to be around 200 μm in diameter. After collimated by a parabolic mirror (MPD229-M01, Thorlabs Inc.), the generated mid-IR pulses pass through a 5-mm thick Germanium window (WG91050-G, Thorlabs Inc.) that blocks the residual pump pulses and signal pulses. A calibrated thermopile detector (3A P/N 7Z02621, Ophir-Spiricon, LLC) measures average power of the mid-IR pulses and their optical spectrum is characterized by a FT-IR scanner (MODEL: 80350, Newport Corporation).

5.3 Generation of the widely tunable signal pulses

As described in Chapter 4, our Yb-fiber laser based, SPM-enabled source can be wavelength tuned from 1.1 μm to 1.25 μm. The resulting pulses are nearly transform-limited. Figure 5.2(a) shows the measured output spectra from 4-cm LMA-PM-10 as we continuously increased the

coupled power. The distinct multiple spectral lobes (see Fig. 5.2(b)) indicate that SPM constitutes the main broadening mechanism. The rightmost spectral lobe continuously shifts towards longer wavelength with the increased power. At the coupled power of 3.24 W, the rightmost spectral lobe is centered at 1200 nm. It is noteworthy that the leftmost spectral lobe peaks at 920 nm, an important wavelength for two-photon florescence microscopy [71, 79]. In this chapter, we focus on the rightmost spectral lobe and use it as the signal to obtain mid-IR pulses via DFG.

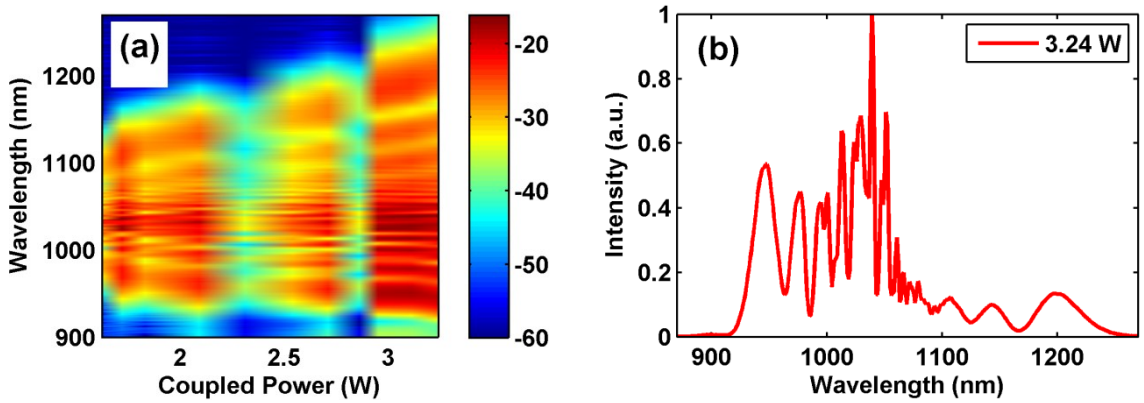

Fig. 5. 2. SPM-enabled broadened spectra in 4-cm long LMA-PM-10. (a) Measured spectra versus coupled average power. Spectral intensity is shown on a logarithm scale. (b) Output spectrum at coupled power of 3.24 W.

Filtered tunable spectral lobes are plotted in Fig. 5.3 with a 10-nm wavelength step. The tunability is achieved by slightly tuning the incident angle on five bandpass filters with different center wavelengths: 1100 nm, 1125 nm, 1150 nm, 1175 nm, and 1200 nm. The full width at half maximum (FWHM) of the pass band is about 50 nm ± 5 nm, and the transmission efficiency is up to 90%. The filtered spectra have a bandwidth of ~40 nm with the profile close to Gaussian shape.

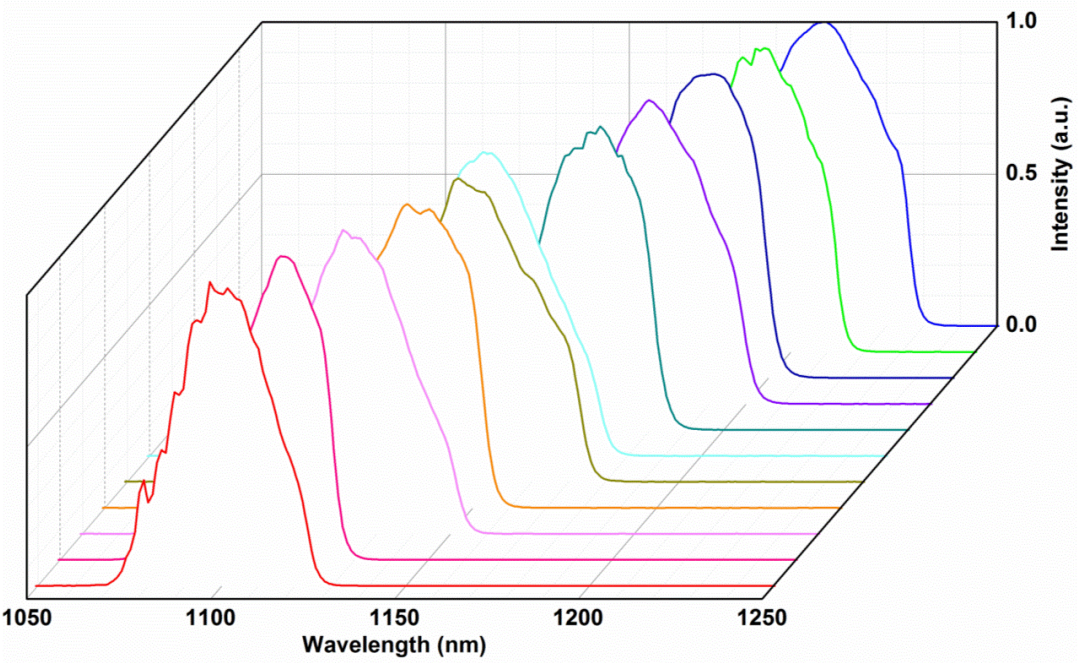

Fig. 5. 3. Filtered spectral lobe centered from 1100 nm to 1200 nm with 10-nm wavelength step.

Measured pulse energy corresponding to the filtered spectra varies from 9.2 nJ to 11.2 nJ, as illustrated by the black curve in Fig. 5.4. We also calculated the energy conversion efficiency from the coupled pulse to the filtered pulse. The blue curve in Fig. 5.4 shows that the conversion efficiency monotonically decreases from 17% to 8% as the center wavelength of the filtered spectrum increases from 1100 nm to 1200 nm.

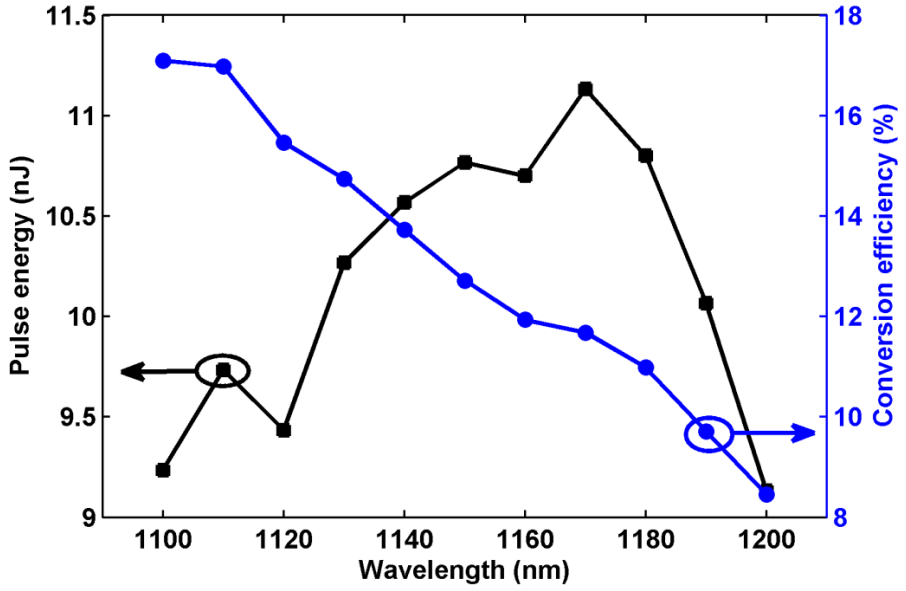

Fig. 5. 4. Measured pulse energy and conversion efficiency of the filtered spectral lobes. Black solid squares: measured pulse energy. Blue solid circles: conversion efficiency.

An intensity auto-correlator (FR-103XL, Femtochrome Research, Inc.) is utilized to measure the pulse duration. Figure 5.5 plots the spectrum and auto-correlation trace of filtered rightmost spectral lobe at 1200 nm. The filtered spectrum shown in Fig. 5.5(a) has a bandwidth (FWHM) of 42-nm. The blue curve in Fig. 5.5(b) shows the measured intensity autocorrelation trace. The pulse duration is estimated to be 117 fs while a deconvolution factor of 1.41 assuming a Gaussian pulse profile. The calculated autocorrelation trance of the transform-limited pulse is also plotted in Fig. 5.5(b) as the black solid curve. The transform-limited pulse duration is 78 fs. The fact that the filtered pulse is about 40-fs longer than the transform-limited pulse might be caused by the initial chirp of the input pulse [76].

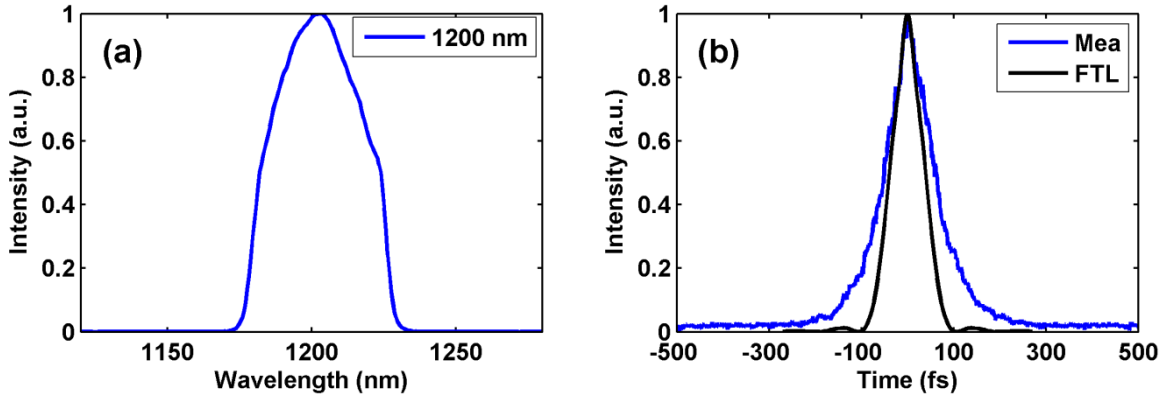

Fig. 5. 5. Filtered spectrum and autocorrelation trace generated from 4-cm LMA-PM-10 fiber. (a) Filtered rightmost spectral lobe at 1200 nm. (b) Blue solid curve: measured autocorrelation trace. Black solid curve: calculated autocorrelation trace corresponding to the transform-limited pulse given by the filtered spectrum. Mea: measured. FTL: Fourier Transform-limited.

As demonstrated in Chapter 4, the pulse energy given by the filtered spectrum can be scaled up using fibers with larger mode area. Figure 5.6(a) shows the spectral broadening versus the coupled power into 4-cm ESM-12B fiber. At the coupled power of 4.77 W, the 8-degree cleaved facet of the ESM-12B fiber is damaged. As a consequence, the center wavelength of the filtered spectrum ends at 1170 nm. Compared with 4-cm LMA-PM-10 fiber, more power is required to shift the rightmost spectral lobe to the same center wavelength, which results in more pulse energy contained in the filtered spectrum. The measured pulse energy and the corresponding conversion efficiency are plotted in Fig. 5.6(b). The filtered spectrum at 1150 nm has the maximum pulse energy of 15 nJ and the one at 1170 nm has the minimum pulse energy of 10 nJ. The conversion efficiency drops from 16% to 6% when the peak wavelength of the filtered spectrum shifts from 1100 nm to 1170 nm. A comparison between Fig. 5.4 and Fig. 5.6(b) shows that fiber ESM-12B produces nearly 1.4 times more pulse energy for the

filtered spectra at the same wavelength than generated by fiber LMA-PM-10. This is consistent with the fact that fiber ESM-12B has a mode-field diameter about 1.2 times larger than fiber LMA-PM-10.

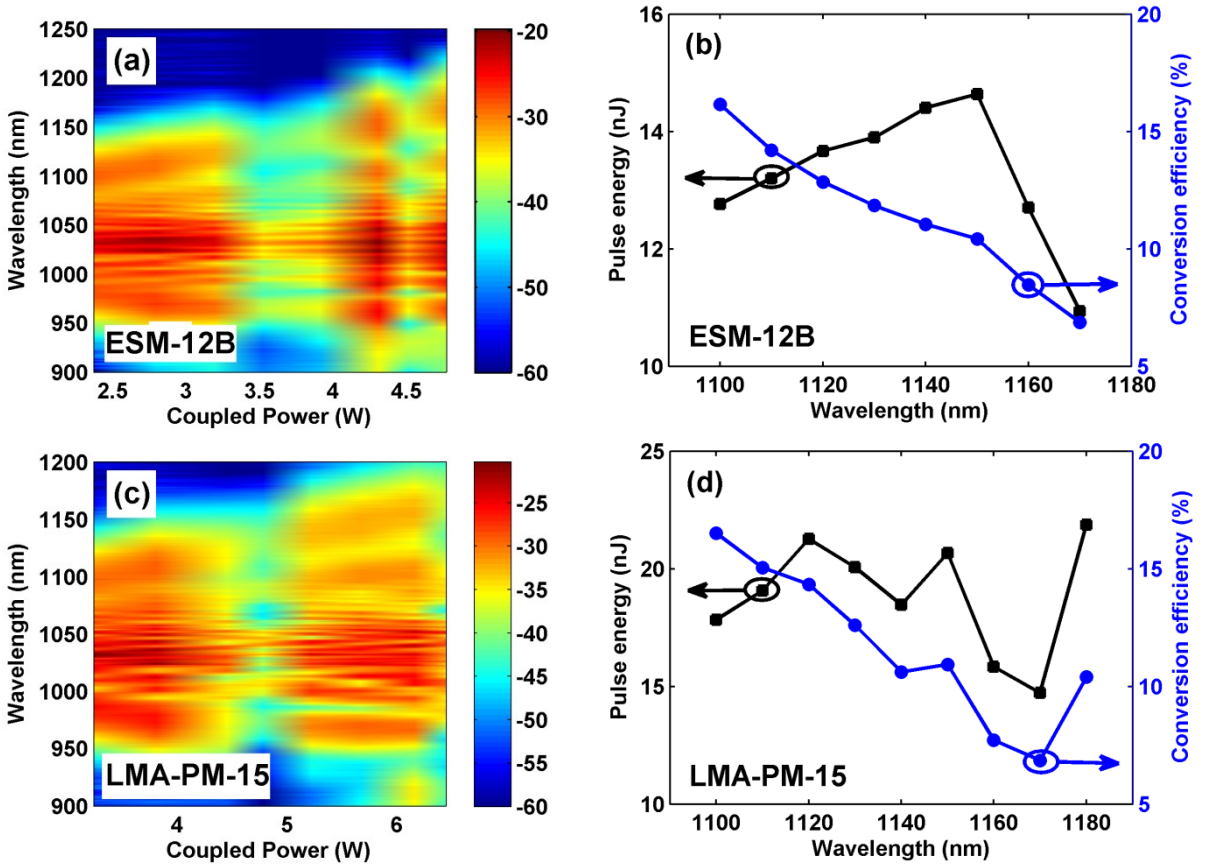

Fig. 5. 6. Spectral broadening and filtering for 4-cm fiber ESM-12B and 4-cm fiber LMA-PM-15 fiber. (a) and (c) show the spectral broadening versus coupled power for fiber ESM-12B and fiber LMA-PM-15, respectively. (b) and (d) plot the corresponding pulse energy and conversion efficiency.

Figure 5.6(c) shows the spectral broadening versus coupled power into 4-cm fiber LMA-PM-15. To avoid fiber surface damage, the coupled power is kept below 6.5 W, and therefore the center wavelength of the filtered spectrum ceases at 1180 nm. Fiber LMA-PM-15 has a mode-field diameter larger than fiber ESM-12B (12.6 μm versus 10.3 μm), more pulse energy is achieved. The maximum pulse energy is ~22 nJ at 1180 nm and the minimum is ~14 nJ at 1170 nm. The blue curve in Fig. 5.6(d) shows that the conversion efficiency varies between 6% and 17%. The generated pulse energy at the same wavelength is almost 2.2 times larger than the one obtained by LMA-PM-10 and 1.5 times larger than the one obtained by ESM-12B fiber.

5.4 Generation and characterization of mid-IR pulses

Mid-IR pulses are obtained by Type-I phase matching ($e - o = o$) DFG in a GaSe crystal with collinear beam geometry. Widely used for DFG, GaSe has a large nonlinearity of 54 pm/V and a broad wavelength-transparency range of 0.65 μm to 18 μm, making it unique for generating mid-IR pulses beyond 10 μm. The remarkably high birefringence in GaSe provides possible phase matching for nearly any combination of signal and idler pulses. However, GaSe also exhibits following drawbacks:

(1) It has a low optical damage threshold. We experimentally found that 30-MHz 165-fs pulses at 1.03 um with ~200-nJ pulses energy can damage a GaSe crystal even the optical beam is loosely focused to ~150-um spot diameter.
(2) The large birefringence results in a strong spatial walk-off between the ordinary wave (o-wave) and extraordinary wave (e-wave). For Type-I phase matching this strong spatial walk-off occurs between the pump pulse and the signal pulse.
(3) The crystal's large dispersion causes considerable group-velocity mismatch between the pump pulse and the signal pulse, which leads to temporal walk-off between these two pulses and weakens the DFG process.
(4) The large dispersion rapidly broadens the pump pulse and signal pulse, and lowers their peak power, and thus reduces the DFG efficiency.
(5) GaSe crystal cannot be cut along at arbitrary angle due to the material structure. The cleave plane is 001 plane and anti-reflection (AR) coating cannot be applied. Due to the high refractive index ($n_o = 2.801$, $n_e = 2.470$), Fresnel loss is about 25%.

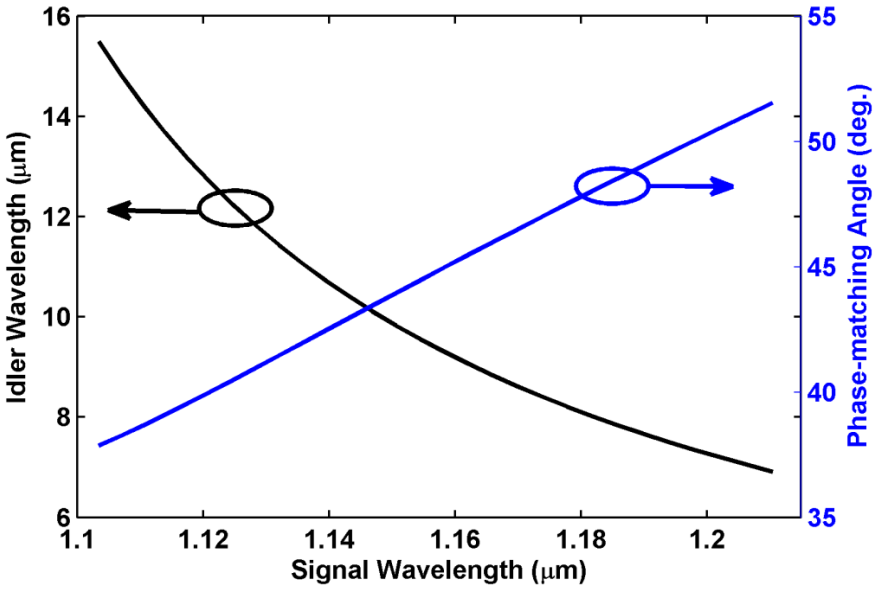

Fig. 5. 7. Calculated idler wavelength and phase-matching angle for the signal pulse centered between 1.1 μm and 1.2 μm. Black curve: corresponding idler wavelength. Blue curve: external phase-matching angle.

Figure 5.7 shows the calculated external phase-matching angle between the pump pulse at 1.032 μm and the signal pulse tunable in the wavelength range of 1.1-1.2 μm. The external phase-matching angle is in the range of 38-52 degrees, and the generated idler pulse has the wavelength tuning range of 7-16 μm.

5.4.1 Spatial and temporal overlap between the signal pulse and the pump pulse

Spatial overlap between the pump pulse and the signal pulse is achieved by visualization of both beam profiles using a CCD camera (SP620U, Ophir Spiricon). The pixel spacing is about 4.4 μm × 4.4 μm, which can distinguish a laser beam with the diameter above 20 μm. Figure 5.8(a) shows the profile of the pump beam after the telescope; the diameter is about 0.893 mm. To mode match with the pump beam, several aspheric lenses are employed to collimate the signal beam (centered at 1.15 μm) at the output of the 4-cm LMA fiber. Figure 5.8(b) shows the signal beam profile after collimation with an 8-mm focal length aspheric lens (C240TME-C, Thorlabs, Inc.); the diameter is about 0.526 mm.

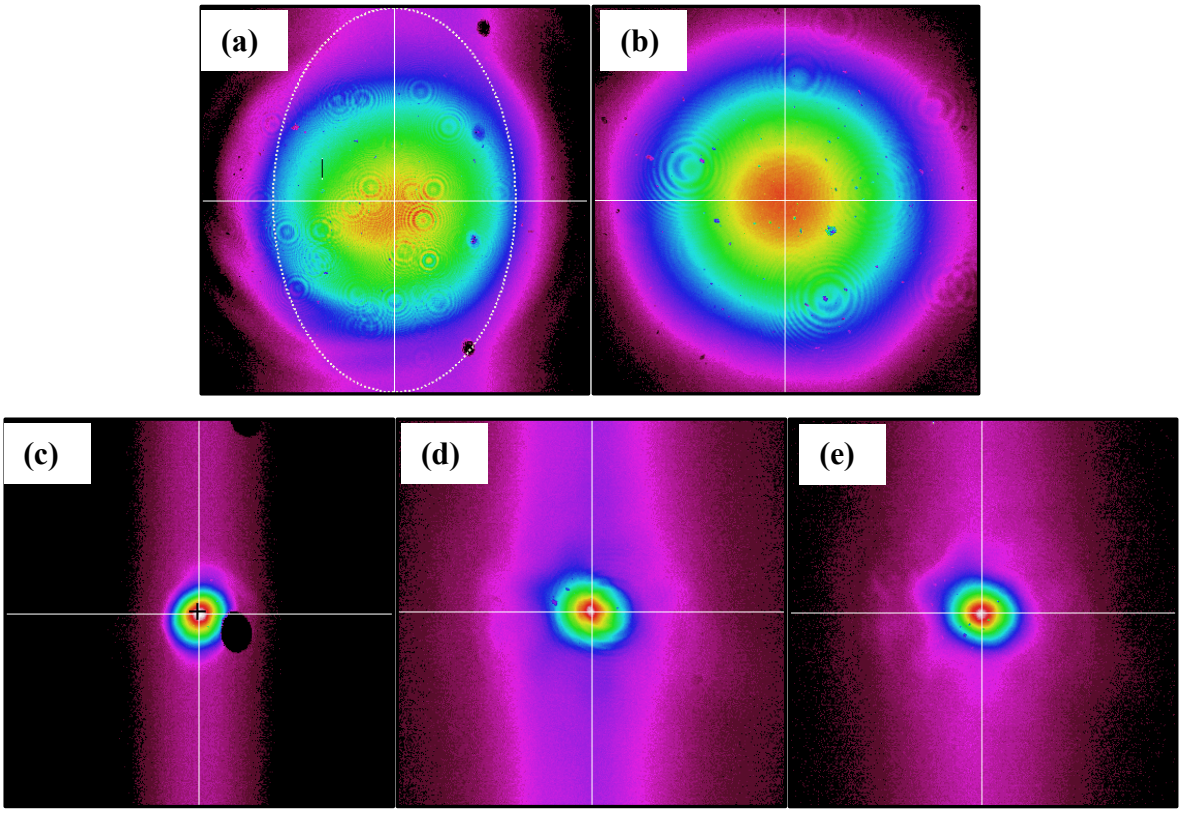

Fig. 5. 8. Pump and signal beam profile before and after focus. (a) Pump beam after telescope. (b) Signal beam after 8-mm focal length aspheric collimation lens. (c) Pump beam at the focus after 100-mm focal length Plano-convex lens. (d) Signal beam at the focus after 100-mm focal length Plano-convex lens. (e) Combined beam at the focus.

GaSe crystal has a bandgap of 2.1 eV, corresponding to one-photon absorption at 650 nm. Therefore two-photon absorption (TPA) becomes severe if the pump pulse at 1.03 μm is too strong. Additionally, tight focusing of both beams suffers from strong spatial walk-off and leads to lower DFG efficiency, as discussed in detail in [78]. We use a plano-convex lens with 100-mm focal length to focus the pump beam and the signal beam into the GaSe crystal. Figure 5.8 (c, d) show the pump beam and the signal beam at the focus with a diameter of 145 μm and 167 μm, respectively. The black dot and purple dots in Fig. 5.8(c, d) are some damage points on the CCD camera. Figure 5.8(e) shows the combined beam at the focus.

We then overlap the pump pulse and the signal pulse in time by using them to generate sum-frequency generation (SFG) in a 10-mm thick Beta Barium Borate (BBO) crystal (type-I phase-matching, cut at 21.9°). Generation of green light indicates a temporal overlap. The delay line at the pump arm is carefully tuned to maximize the SFG power. The spatial and temporal overlap is routinely optimized for DFG as we tune the signal pulse wavelength.

5.4.2 DFG in GaSe crystal

Two GaSe crystals with different thickness—0.5 mm and 2 mm—are employed. Signal pulses obtained from 4-cm LAM-PM-10 fiber are combined with the pump pulses to generated mid-IR pulses in the 0.5-mm thick GaSe crystal. Figure 5.9 plots the measured mid-IR spectra and their average power as the center wavelength of the signal pulses is tuned in 1100-1200 nm with 10-nm wavelength step. The center wavelength of generated mid-IR pulses varies from 7.4 μm to 15.6 μm with a spectral bandwidth (FWHM) about 1.0-1.4 μm. The maximum bandwidth of 1.4 μm is obtained for the mid-IR pulse centered at 15.6 μm. The blue circles connected by the blue dashed line show the average power for each mid-IR spectrum measured by a calibrated thermopile detector (3A P/N 7Z02621, Ophir-Spiricon). The maximum measured power is 1.25 mW for the mid-IR pulses at 7.7 μm as a result of DFG between the pump pulses at 1.03 μm and the signal pulses at 1.19 μm. The minimum measured power is 0.34 mW for the mid-IR pulses at 15.6 μm (DFG between the 1.03-μm pump and the 1.10-μm signal). The fine structures in mid-IR spectrum that peaks at 7.4 μm (red curve in Fig. 5.9) are caused by the water absorption in the environmental air [80]. CO_2 in the atmosphere exhibits strong absorption at 14.62 μm, which generates a deep spectral valley in the mid-IR spectra that cover this wavelength [81].

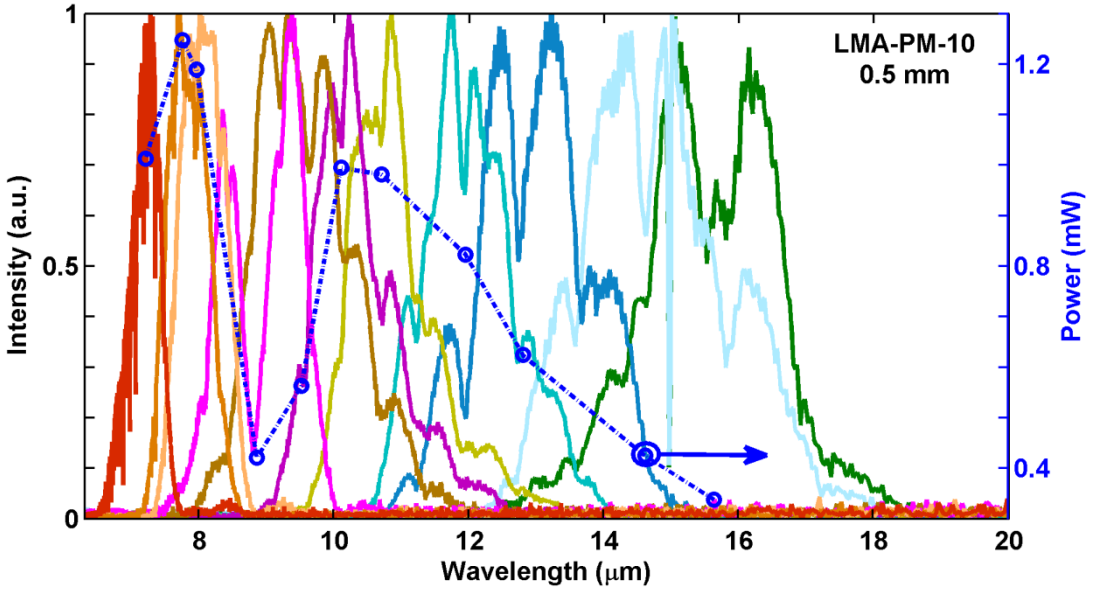

Fig. 5. 9. Measured spectra and average power for the mid-IR pulses generated in a 0.5-mm long GaSe crystal. The signal pulses tuned from 1100-1200 nm were generated by 4-cm LMA-PM-10 fiber.

We then replace the 0.5-mm thick GaSe by a 2-mm thick one and redo the experiments. The measured spectra and their average power are recorded in Fig. 5.10. Since a thicker crystal permits smaller phase-matching bandwidth, the mid-IR spectra generated by 2-mm thick GaSe possess a narrower spectral bandwidth of 0.3-1.12 μm compared with those generated by 0.5-mm thick crystal. At the expense of phase-matching bandwidth, a thicker GaSe crystal increases the power of mid-IR pulse yield by a factor of ~3. The maximum average power is 3.31 mW for the mid-IR pulses at 8.22 μm and the minimum is 0.91 mW at 16.7 μm.

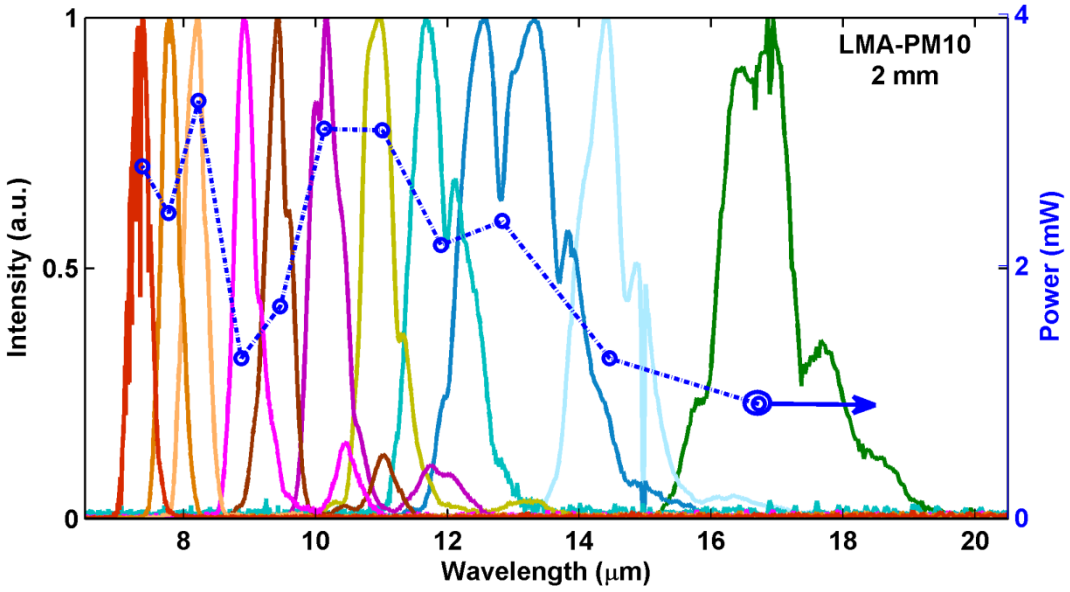

Fig. 5. 10. Measured spectra and average power for the mid-IR pulses generated in a 2-mm long GaSe crystal. The signal pulses tuned from 1100-1200 nm were generated by 4-cm LMA-PM-10 fiber.

We also employ either 4-cm ESM-12B fiber or 4-cm LMA-PM-15 to obtain the tunable signal pulses. We then combine these signal pulses with the pump pulses to perform DFG in both GaSe crystals. The experimental results corresponding to the ESM-12B fiber are presented in Fig. 5.11. The employed signal pulse energy varies from 10.9 nJ (at 1170 nm) to 14.6 nJ (at 1150 nm). As we expect, the mid-IR spectra obtained from 0.5-mm thick GaSe has a broader bandwith of 1.1 μm to 2.1 μm. Maximum bandwidth of 2.1 μm is obtained at 16.7 μm. The mid-IR pulses generated by 2-mm thick GaSe have higher average power. For example, 5.04-mW mid-IR pulses are obtained at 11 μm, corresponding to 168-pJ pulse energy.

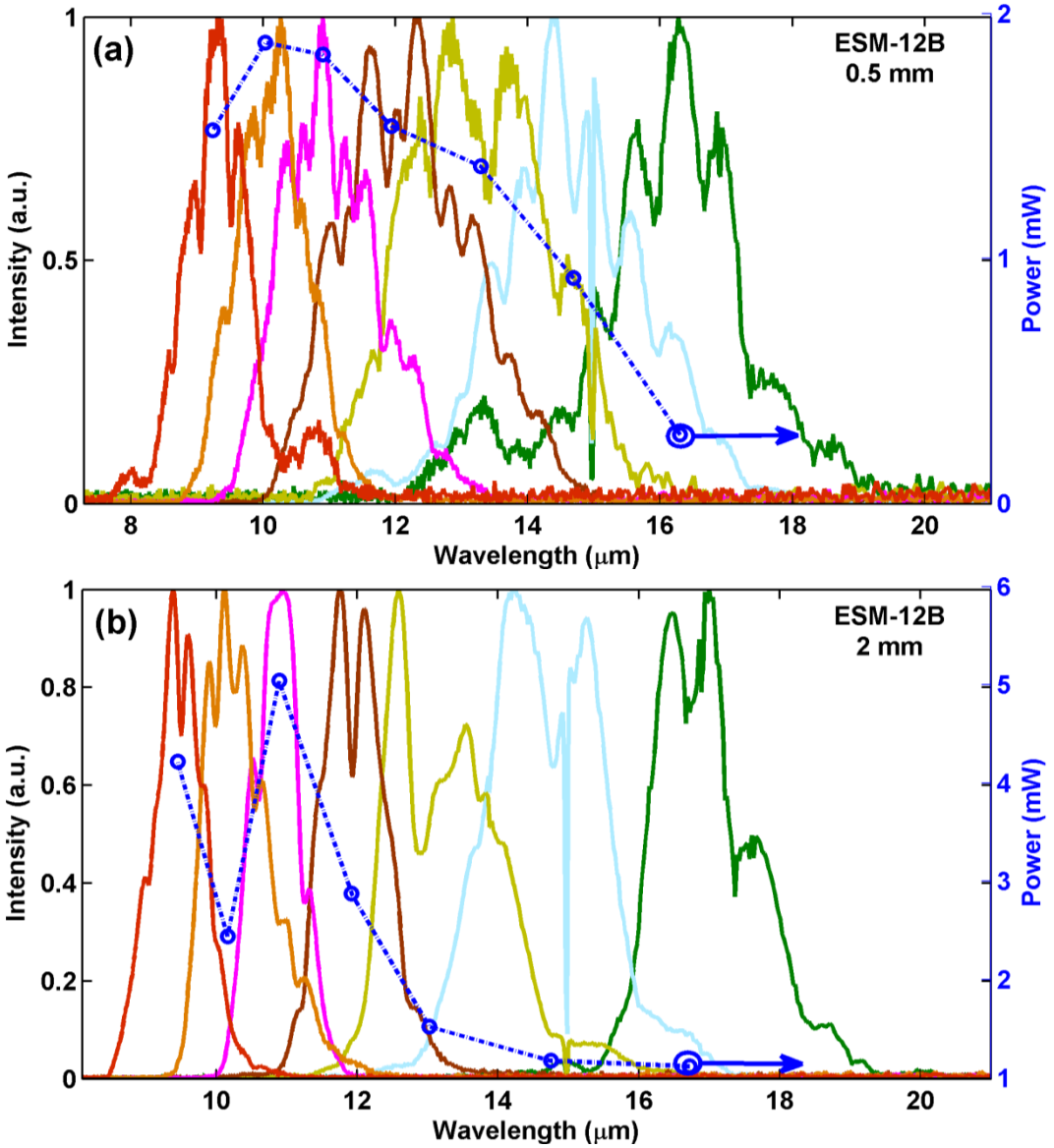

Fig. 5. 11. Measured spectra and average power for the mid-IR pulses generated in GaSe crystal with different thickness: (a) 0.5 mm and (b) 2 mm. The signal pulses tuned from 1100-1200 nm were generated by 4-cm ESM-12B fiber.

The experimental results with the signal pulses generated by the LMA-PM-15 fiber are presented in Fig. 5.12. A comparison of Fig. 5.11 and Fig. 5.12 shows that the mid-IR pulses share similar average power though the signal pulses obtained from LMA-PM-15 fiber are stronger than those pulses obtained from ESM-12B fiber. This is caused by the fiber dispersion, which plays a critical role in the SPM-dominated spectral broadening. LMA-PM-15 fiber has a larger dispersion and the resulting filtered pulses are more chirped with a narrower spectral bandwidth. As a result, the DFG efficiency is compromised.

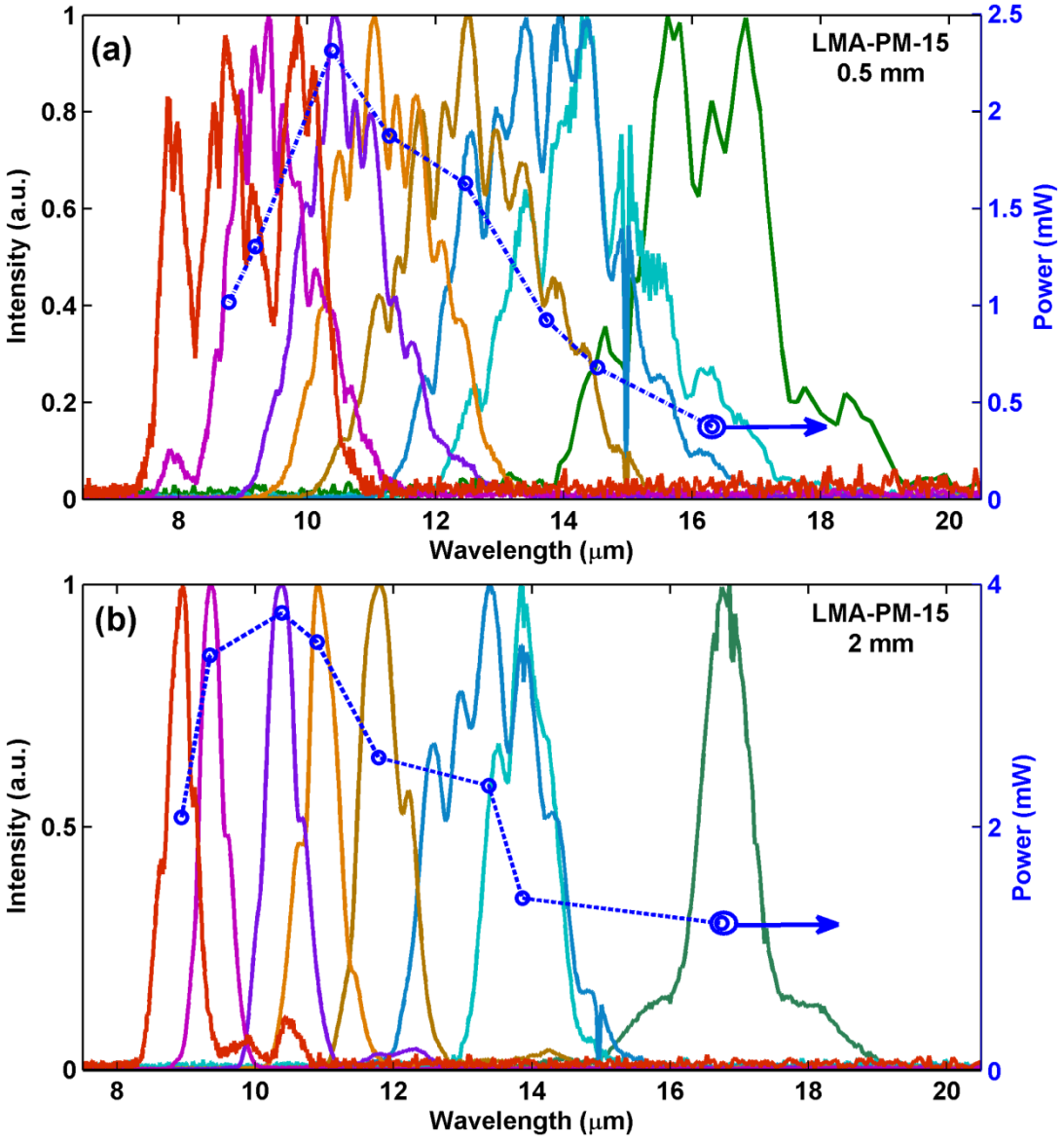

Fig. 5. 12. Measured spectra and average power for the mid-IR pulses generated in GaSe crystal with different thickness: (a) 0.5 mm and (b) 2 mm. The signal pulses tuned from 1100-1200 nm were generated by 4-cm LMA-PM-15 fiber.

To investigate the power scalability of the mid-IR pulses as the function of the pump power and the signal power, we fix the signal wavelength at 1150 nm generated by the 4-cm LMA-PM-15 fiber. The 1150-nm signal beam has an average power of >600 mW. A metallic neutral density step-variable filter (NDC-100S-4M, Thorlabs) is placed in the signal arm to adjust the launched signal power onto the crystal. Pump power can be continuously adjusted by the combination of a HWP and PBS in the pump arm. The neutral density filter in the signal arm introduces an extra temporal delay for the signal pulse, which requires minor delay compensation by fine adjusting the translation stage in the pump arm. We then

separately vary the power of both the pump beam and the signal beam and measure the average power of the resulting mid-IR pulses (centered at 9.8 μm) generated by DFG in the 2-mm thick GaSe.

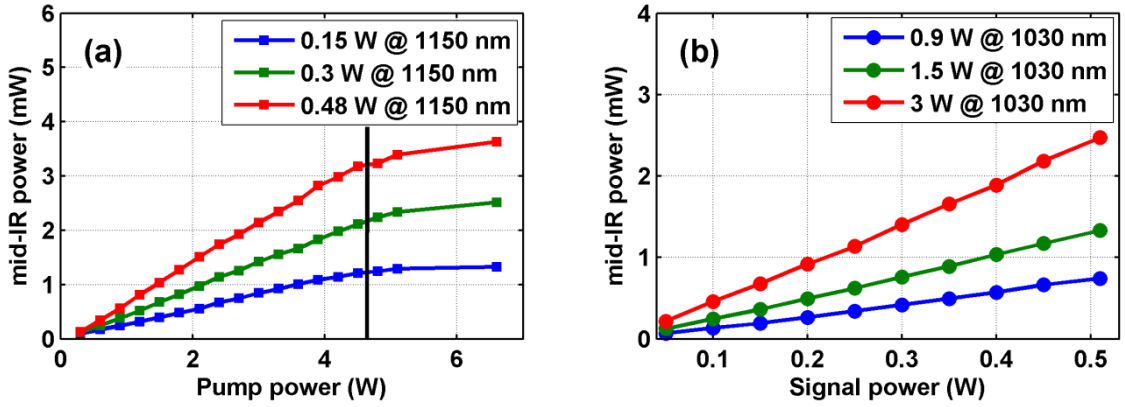

Fig. 5. 13. Power scaling of the mid-IR pulses as a function of pump power and signal power. The signal pulses at the wavelength of 1150 nm are derived from 4-cm LMA-PM-15 fiber. Mid-IR pulses are generated by DFG in the 2-mm thick GaSe crystal. (a) Dependence of mid-IR power as a function of pump power for the signal beam at different power: 0.15 W (blue curve), 0.3 W (green curve), and 0.48 W (red curve). The black vertical line indicates that pump power >4.5 W leads to power saturation of the generated mid-IR pulses. (b) Dependence of mid-IR power as a function of signal power for the pump beam at different power: 0.9 W (blue curve), 1.5 W (green curve), and 3 W (red curve).

Figure 5.13(a) shows the mid-IR power as a function of pump power for the signal beam at different power of 0.15 W (blue curve), 0.3 W (green curve), and 0.48 W (red curve). Clearly for a fixed signal power, the mid-IR power linearly increases with the increased pump power until saturation occurs when the pump power reaches 4.5 W (corresponding to 150-nJ pulse energy). This saturation is caused by the onset of two-photon absorption in GaSe. Further increasing the pump power to ~7 W leads to crystal damage. The same power of generated mid-IR pulses can be achieved by using different power combinations of the pump beam and the signal beam. For example, 1-mW mid-IR pulses can be obtained using the following pump-signal power combinations: (1.5-W pump, 0.48-W signal), (2.4-W pump, 0.3-W signal), and (3.6-W pump, 0.15-W signal). These results immediately suggest that increasing the signal power constitutes an efficient approach for power scaling the generated mid-IR pulses. This is of particular importance given that the pump power is not limited by the Yb-fiber laser system, but by the GaSe's two-photon absorption and damage threshold, which impose a maximum value allowed for the pump power onto the GaSe crystal. In this scenario, further improvement of the mid-IR power can be achieved by increasing the signal power. Figure 5.13(b) shows the mid-IR power as a function of signal power for the pump beam at

different power of 0.9 W (blue curve), 1.5 W (green curve), and 3 W (red curve). For a fixed pump power, the mid-IR power linearly increases with the increased signal power without noticeable saturation. Note that the last data point in the blue curve corresponds to 900-mW pump power and 510-mW signal power; that is the pump and the signal are at the similar power level. This represents a significant deviation from the conventional DFG configuration in which the pump beam is 2-3 orders magnitude stronger than the signal beam.

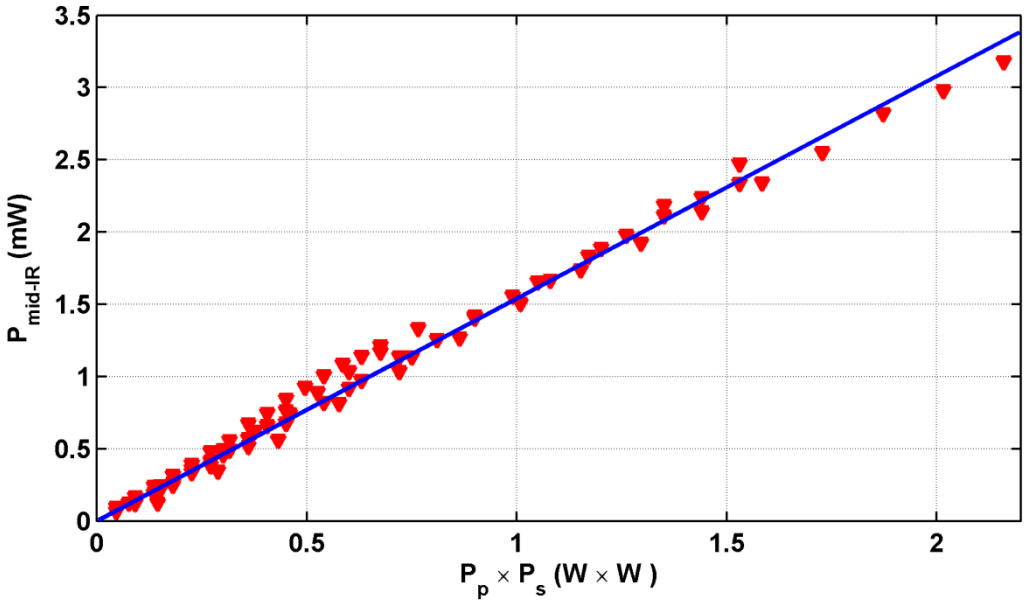

Fig. 5. 14. Mid-IR power versus the power product between the pump beam and the signal beam. Red triangles: experimental data. Blue line: linear fit.

The linear dependence of the mid-IR power on both the signal power and the pump power—which is valid for the pump power below 4.5 W—implies that the mid-IR power scales up with the power product between the pump beam and the signal beam. To better illustrate this point, we re-plot the experimental data in terms of the mid-IR power versus the power product of the pump beam and the signal beam. The red triangles in Fig. 5.14 represent these data points. Note that the data points corresponding to the pump power >4.5 W are intentionally left out to avoid the saturation effect caused by GaSe's two-photon absorption.

The blue curve in Fig. 5.14 is linear fit of the data and confirms the linear dependence of the mid-IR power on the pump-signal power product.

5.5 Conclusion

We employ the high-power Yb-fiber laser system described in Chapter 3 to implement a high-power ultrafast mid-IR laser source based on DFG in GaSe crystals. The powerful signal pulses are obtained by filtering the rightmost spectral lobes of optical spectra broadened by SPM-dominated nonlinearity inside an optical fiber. The resulting mid-IR pulses are tunable from 7.4 μm to 16.8 μm. We experimentally investigate the power scaling of this DFG source and demonstrate that increasing the signal power is an efficient approach for generating high power mid-IR pulses. Up to 5.04-mW mid-IR pulses centered at 11 μm is achieved. The corresponding pulse energy is 167 pJ, representing a nearly one order of magnitude improvement compared with the reported DFG-based mid-IR source at this wavelength.

Chapter 6

Conclusion and Outlook

Ultrafast mid-IR sources have been rapidly developed over the past decade. Difference-frequency generation (DFG) between a pump pulse with fixed center wavelength and a signal pulse with the center wavelength widely tunable constitutes the only means to generate mid-IR femtosecond pulses in the wavelength range of 8-20 μm. Required to be synchronized, the pump pulse and the signal pulse are normally derived from the same ultrafast laser source in a way such that they share the same carrier-envelope offset frequency f_{CE}; as a result, the resulting mid-IR source has its f_{CE} automatically set at zero. In other words, the carrier-envelope phase of the mid-IR source is passively stabilized. These DFG-based mid-IR femtosecond sources with the repetition rate at 10s of MHz (or even higher) are of particular importance for spectroscopy applications. It is noteworthy that simply stabilizing the repetition rate of the source laser—from which both the pump pule and the signal pulse are derived—leads to a mid-IR frequency comb, a powerful enabling tool for high-speed and high sensitivity sensing and spectroscopy.

Soliton self-frequency shift (SSFS) in an optical fiber has become a popular method to generate the signal pulse. The resulting Raman soliton source is wavelength tunable and produces transform-limited pulses. In Chapter 2, we present a detailed study of the noise performance of such a Raman soliton source. We show—both numerically and experimentally—that the relative intensity noise of the excitation pulse translates into the relative timing jitter (RTJ) between the Raman soliton pulse and the excitation pulse. The RTJ results in increased relative intensity noise and timing jitter of the mid-IR source implemented by the DFG between the Raman soliton pulse and the excitation pulse. Besides the large RTJ, Raman soliton source that is derived from an ultrafast Yb-fiber laser exhibits low pulse energy (normally <1 nJ) and is unsuitable to serve as the signal pulse in the DFG process.

To implement a high repetition-rate, high power ultrafast mid-IR source, we first need a powerful ultrafast laser source. In Chapter 3, we present a detailed design of a high power Yb-fiber laser system employing chirped-pulse amplification. The Yb-fiber laser system operates at 30-MHz repetition rate and emits 165-fs pulses with 14.5-W average power.

Limited by the nonlinear crystal's damage threshold, the pump pulse energy has to be kept under a certain value. Therefore increasing the signal pulse energy is an efficient way of power scaling the ultrafast mid-IR source. We demonstrate a new type of fiber-optic ultrafast source derived from the high-power Yb-fiber laser developed in Chapter 3. This wavelength widely tunable source is achieved by optically filtering the rightmost spectral lobe of an optical spectrum broadened largely due to self-phase modulation (SPM). Such an SPM-enabled spectral selection (SESS) in a short large-mode-area (LMA) fiber generates high-energy and widely tunable femtosecond pulses. In Chapter 4, we focus on generating femtosecond pulses in the wavelength range of 1200-1300 nm, an important wavelength range for driving multiphoton microscopy. For example, using 4-cm LMA-PM-15 fiber, we obtained ultrashort pulses with up to 16.5-nJ pulse energy at the wavelength of 1225 nm.

In Chapter 5, we employ SESS to produce high-energy (up to 20 nJ) femtosecond pulses that are wavelength tunable in 1100-1200 nm. We then use this SESS source as the signal pulse and the rest power from the Yb-fiber source laser as the pump pulse; the DFG between these two pulses results in an ultrafast mid-IR source that can be wavelength tuned from 7.4 um to 16.8 um. The power dependence of the mid-IR source on the pump pulse and the signal pulse is carefully investigated, indicating that increasing the signal pulse energy can efficiently improve the power yield of the resulting mid-IR source. We obtain >5-mW mid-IR pulses at 11 μm via DFG in 2-mm thick GaSe, corresponding to ~170-pJ pulse energy.

Figure 6.1 summarizes published results of high repetition-rate ultrafast mid-IR sources with the carrier-envelope phase passively stabilized. These sources are based on DFG in CSP, AGS, and GaSe crystals. Each colored line represents the whole tunable spectral range; the height of the line only denotes the maximum pulse energy in this wavelength range. Reference 8 reports 150-pJ pulse energy, but the wavelength tunability is only from 6.2 – 7.4 μm. My work is also shown in the Fig. 6.1 as the red line. For the mid-IR wavelength range of 7 – 17 μm, my results represent nearly one order of magnitude improvement over the published results.

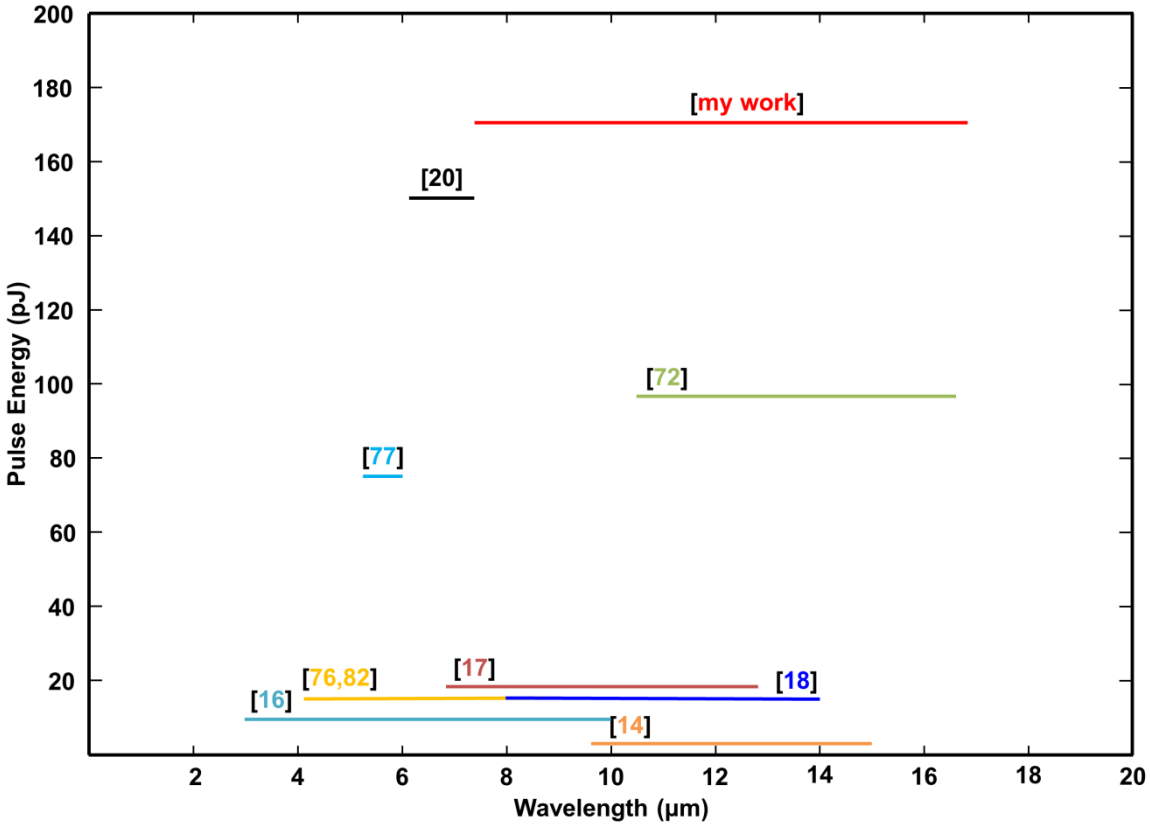

Fig. 6. 1 Summary of recent mid-IR source obtained by DFG in CSP, GaSe, and AGS crystals.

In our current setup, our signal pulse energy is about 20 nJ. Using a fiber with even larger mode area, we can further increase the signal pulse energy. We believe that nJ-level mid-IR pulses are possible. In combination with high repetition rate, ultrafast mid-IR sources with sub-Watt level average power are within the reach. By stabilizing the repetition rate f_R of Yb-fiber laser system, mid-IR laser frequency combs with unprecedented line power can be implemented, which will open new avenues for many potential spectroscopy applications.

References

[1] F. Tittel, D. Richter, and A. Fried, “Mid-infrared laser applications in spectroscopy solid-state mid-infrared laser sources,” in Solid-State Mid-Infrared Laser Sources I. Sorokina, and K. Vodopyanov, eds. (Springer 2003).

[2] A. Schliesser, N. Picque, and T. W. Hansch, “Mid-infrared frequency combs,” Nat. Photonics 6(7), 440–449 (2012).

[3] R. P. Prasankumar and A. J. Taylor, Optical techniques for solid-state material characterization, Taylor & Francis, 2012.

[4] J. Ye and S. T. Cundiff (eds), Femtosecond optical frequency comb: principle, operation, and applications, (Springer, 2005).

[5] M. J. Thorpe, D. Balslev-Clausen, M. S. Kirchner, and J. Ye, “Cavity-enhanced optical frequency comb spectroscopy: application to human breath analysis,” Opt. Express 16, 2387 (2008).

[6] H. Pires, M. Baudisch, D. Sanchez, M. Hemmer, J. Biegert, “Ultrashort pulse generation in the mid-IR,” Prog. Quant. Electron. 43, 1 (2015).

[7] R. W. Boyd, *Nonlinear optics*. Academic press, 2008.

[8] G. P. Agrawal, *Nonlinear fiber optics*. Academic press, 2007.

[9] https://en.wikipedia.org/wiki/Soliton

[10] F. M. Mitschke and L. F. Mollenauer, "Discovery of the soliton self-frequency shift," Opt. Lett. 11, 659-661 (1986).

[11] J. P. Gordon, "Theory of the soliton self-frequency shift," Opt. Lett. 11, 662-664 (1986).

[12] H. Lim, J. Buckley, A. Chong, and F. W. Wise, “Fibre-based source of femtosecond pulses tunable from 1.0 to 1.3 μm,” Electron. Lett. 40, 1523 (2004).

[13] J. Takayanagi, T. Sugiura, M. Yoshida, and N. Nishizawa, “1.0–1.7-μm wavelength-tunable ultrashort-pulse generation using femtosecond Ybdoped fiber laser and photonic crystal fiber,” IEEE Photon. Technol. Lett. 18, 2284 (2006).

[14] David G. Winters, Philip Schlup, and Randy A. Bartels, "Subpicosecond fiber-based soliton-tuned mid-infrared source in the 9.7–14.9 μm wavelength region," Opt. Lett. 35, 2179-2181 (2010).

[15] Tyler W. Neely, Todd A. Johnson, and Scott A. Diddams, "High-power broadband laser source tunable from 3.0 μm to 4.4 μmbased on a femtosecond Yb:fiber oscillator," Opt. Lett. 36, 4020-4022 (2011).

[16] Axel Ruehl, Alessio Gambetta, Ingmar Hartl, Martin E. Fermann, Kjeld S. E. Eikema, and Marco Marangoni, "Widely-tunable mid-infrared frequency comb source based on difference frequency generation," Opt. Lett. 37, 2232-2234 (2012).

[17] C. R. Phillips, J. Jiang, C. Mohr, C. Langrock, M. Snure, D. Bliss, M. Zhu, I. Hartl, J. S. Harris, M. E. Fermann, and M. M. Fejer, "Widely tunable midinfrared difference frequency generation in orientation-patterned GaAs pumped with a femtosecond Tm-fiber system," Opt. Lett. 37, 2928 (2012).

[18] Alessio Gambetta, Nicola Coluccelli, Marco Cassinerio, Davide Gatti, Paolo Laporta, Gianluca Galzerano, and Marco Marangoni, "Milliwatt-level frequency combs in the 8–14 μm range via difference frequency generation from an Er:fiber oscillator," Opt. Lett. 38, 1155-1157 (2013).

[19] Nicola Coluccelli, Marco Cassinerio, Alessio Gambetta, Paolo Laporta, and Gianluca Galzerano, "High-power frequency comb in the range of 2–2.15 μm based on a holmium fiber amplifier seeded by wavelength-shifted Raman solitons from an erbium-fiber laser," Opt. Lett. 39, 1661-1664 (2014).

[20] D. Sánchez, M. Hemmer, M. Baudisch, K. Zawilski, P. Schunemann, H. Hoogland, R. Holzwarth, and J. Biegert, "Broadband mid-IR frequency comb with CdSiP2 and AgGaS2 from an Er,Tm:Ho fiber laser," Opt. Lett. 39, 6883-6886 (2014).

[21] J. van Howe, J. H. Lee, S. Zhou, F. Wise, C. Xu, S. Ramachandran, S. Ghalmi, and M. F. Yan, “Demonstration of soliton self-frequency shift below 1300 nm in higher-order mode, solid silica-based fiber,” Opt. Lett. 32, 340 (2007).

[22] M. E. Pedersen, J. Cheng, K. Charan, K. Wang, C. Xu, L. Gruner-Nielsen, and D. Jakobsen, “Higher-order-mode fiber optimized for energetic soliton propagation,” Opt. Lett. 37, 3459 (2012).

[23] V. Petrov, “Frequency down-conversion of solid-state laser sources to the mid-infrared spectral range using non-oxide nonlinear crystals,” Prog. Quant. Electron. 42, 1 (2015).

[24] C. Xu and F. W. Wise, “Recent advances in fibre lasers for nonlinear microscopy,” Nat. Photonics 7(11), 875–882 (2013).

[25] J. W. Walewski, M. R. Borden, S. T. Sanders, "Wavelength-agile laser system based on soliton self-shift and its application for broadband spectroscopy," Appl. Phys. B. 79, 937 (2004).

[26] A. A. Ivanov, A. A. Podshivalov, and A. M. Zheltikov, "Frequency-shifted megawatt soliton output of a hollow photonic-crystal fiber for time-resolved coherent anti-Stokes Raman scattering microspectroscopy," Opt. Lett. 31, 3318-3320 (2006).

[27] Nicholas G. Horton, Ke Wang, Demirhan Kobat, Catharine G. Clark, Frank W. Wise, Chris B. Schaffer & Chris Xu, "In vivo three-photon microscopy of subcortical structures within an intact mouse brain," Nat. Photon. 7, 205 (2013).

[28] T. R. Schibli, J. Kim, O. Kuzucu, J. Gopinath, S. N. Tandon, G. S. Petrich, L. A. Kolodziejski, J. G. Fujimoto, E. P. Ippen, and F. X. Kärtner, Opt. Lett. 28, 947 (2003).

[29] Youjian Song, Kwangyun Jung, and Jungwon Kim, "Impact of pulse dynamics on timing jitter in mode-locked fiber lasers," Opt. Lett. 36, 1761-1763 (2011).

[30] Andrew J. Benedick, James G. Fujimoto & Franz X. Kärtner, "Optical flywheels with attosecond jitter," Nat. Photon. 6, 97 (2012).

[31] Jungwon Kim, Jonathan A. Cox, Jian Chen & Franz X. Kärtner, "Drift-free femtosecond timing synchronization of remote optical and microwave sources," Nat. Photonics 2, 733 (2008).

[32] Ming Xin, Kemal Şafak, Michael Y. Peng, Patrick T. Callahan, and Franz X. Kärtner, "One-femtosecond, long-term stable remote laser synchronization over a 3.5-km fiber link," Opt. Express 22, 14904-14912 (2014).

[33] J. A. Cox, W. P. Putnam, A. Sell, A. Leitenstorfer, and F. X. Kärtner, "Pulse synthesis in the single-cycle regime from independent mode-locked lasers using attosecond-precision feedback," Opt. Lett. 37, 3579-3581 (2012).

[34] Podlipensky, P. Szarniak, N. Y. Joly, C. G. Poulton, and P.St.J. Russell, "Bound soliton pairs in photonic crystal fiber," Opt. Express 15, 1653-1662 (2007).

[35] Guoqing Chang, Li-Jin Chen, and Franz X. Kärtner, "Highly efficient Cherenkov radiation in photonic crystal fibers for broadband visible wavelength generation," Opt. Lett. 35, 2361-2363 (2010).

[36] C. Kerse, H. Kalaycıoğlu, P. Elahi, B. Çetin, D. K. Kesim, Ö. Akçaalan, S. Yavaş, M. D. Aşık, B. Öktem, H. Hoogland, R. Holzwarth, and F. Ö. Ilday, "Ablation-cooled material removal with ultrafast bursts of pulses," Nature 537, 84 (2016).

[37] R. J. Jones, K. D. Moll, M. J. Thorpe, and J. Ye, "Phase-coherent frequency combs in the vacuum ultraviolet via high-harmonic generation inside a femtosecond enhancement cavity," Phys. Rev. Lett. 94, 193201 (2005).

[38] A. Cingoz, D. C. Yost, T. K. Allison, A. Ruehl, M. E. Fermann, I. Hartl, and J. Ye, "Direct frequency comb spectroscopy in the extreme ultraviolet," Nature 482, 68 (2012).

[39] I. Pupeza, S. Holzberger, T. Eidam, H. Carstens, D. Esser, J. Weitenberg, P. Russbueldt, J. Rauschenberger, J. Limpert, T. Udem, A. Tünnermann, T. W. Hansch, A. Apolonski, F. Krausz, and E. Fill, "Compact high-repetition-rate source of coherent 100 eV radiation," Nat. Photonics 7, 608 (2013).

[40] D. Strickland and G. Mourou, "Compression of amplified chirped optical pulses," Opt. Commun. 56, 219 (1985).

[41] Y. Zhou, G. Chang, H. Chen, P. C. Chui, K. K. Y. Wong, and F. X. Kaertner, "Nonlinear-polarization-evolution mode-locking in a hybrid cavity: a route toward low repetition-rate fiber lasers," in Conference on Lasers and Electro-Optics 2012, OSA Technical Digest (online) (Optical Society of America, 2012), paper CF3L.3.

[42] C. Li, Y. Ma, X. Gao, F. Niu, T. Jiang, A. Wang, and Z. Zhang, "1 GHz repetition rate femtosecond Yb:fiber laser for direct generation of carrier-envelope offset frequency," Appl. Opt. 54, 8350–8353 (2015).

[43] M. Zhang, L. L. Chen, C. Zhou, Y. Cai, L. Ren, and Z. G. Zhang, "Mode-locked ytterbium-doped linear-cavity fiber laser operated at low repetition rate," Laser Phys. Lett. 6(9), 657–660 (2009).

[44] K. Tamura, H. A. Haus, and E. P. Ippen, "Self-starting additive pulse mode-locked erbium fiber ring laser," Electron. Lett. 28, 2226-2227 (1992).

[45] M Hofer, M.H. Ober, F. Haberl, M.E. Fermann, "Characterization of ultrashort pulse formation in passively mode-locked fiber lasers," IEEE J. Quantum Electron. 28, 720 (1992).

[46] V. J. Matsas, T. P. Newson, D. J. Richardson, and D. N. Payne, "Self-starting passively mode-locked fibre ring soliton laser exploiting nonlinear polarisation rotation," Electron. Lett. 28, 2226–2228 (1992).

[47] M. E. Fermann, M. J. Andrejco, Y. Silberberg and M. L. Stock, "Passive mode-locking by using nonlinear polarization evolution in a polarizing-maintaining erbium-doped fiber laser," Opt. Lett. 29, 447-449, (1993).

[48] D. N. Papadopoulos, Y. Zaouter, M. Hanna, F. Druon, E. Mottay, E. Cormier, and P. Georges, "Generation of 63 fs 4.1 MW peak power pulses from a parabolic fiber amplifier operated beyond the gain bandwidth limit," Opt. Lett. 32, 2520-2522 (2007).

[49] A. Chong, L. Kuznetsova, and F. W. Wise, "Theoretical optimization of nonlinear chirped-pulse fiber amplifiers," J. Opt. Soc. Am. B 24, 1815-1823 (2007).

[50] L. Kuznetsova and F. W. Wise, "Scaling of femtosecond Yb-doped fiber amplifiers to tens of microjoule pulse energy via nonlinear chirped pulse amplification," Opt. Lett. 32, 2671-2673 (2007).

[51] Y. Deng, C.-Y. Chien, B. G. Fidric, and J. D. Kafka, "Generation of sub-50 fs pulses from a high-power yb-doped fiber amplifier," Opt. Lett. 34, 3469–3471 (2009).

[52] B. Nie, D. Pestov, F. W. Wise, and M. Dantus, "Generation of 42-fs and 10-nJ pulses from a fiber laser with self-similar evolution in the gain segment," Opt. Express 19, 12074–12080 (2011).

[53] F. X. Kärtner and U. Keller, "Stabilization of solitonlike pulses with a slow saturable absorber," Opt. Lett. 20(1), 16–18 (1995).

[54] W. Liu, C. Li, Z. G. Zhang, F. X. Kärtner, and G. Q. Chang, "Self-phase modulation enabled, wavelength tunable ultrafast fiber laser sources: an energy scalable approach," Opt. Express 24(14), 15328–15340 (2016).

[55] G. Zhou, M. Xin, Y. Liu, F. X. Kaertner, and G. Chang, "SPM-enabled fiber laser source beyond 1.2 μm," in Lasers Congress 2016 (ASSL, LSC, LAC), OSA Technical Digest (online) (Optical Society of America, 2016), paper ATh1A.4.

[56] G. E. Cook, "Pulse compression-key to more efficient radar transmission," Proc. IRE 48, 310 (1960).

[57] L. Grüner-Nielsen, D. Jakobsen, K. G. Jespersen, and B. Pálsdóttir, "A stretcher fiber for use in fs chirped pulse Yb amplifiers," Opt. Express 18(4), 3768–3773 (2010).

[58] E. B. Treacy, "Optical pulse compression with diffraction gratings", IEEE J. Quantum Electron. 5 (9), 454 (1969).

[59] W. R. Zipfel, R. M. Williams, W. W. Webb, "Nonlinear magic: multiphoton microscopy in the biosciences," Nature Biotechnology 21, 1369 (2003).

[60] F. Helmchen, and W. Denk, "Deep tissue two-photon microscopy," Nat. Methods 2, 932-940 (2005).

[61] P. Theer, M.T. Hasan, and W. Denk, “Two-photon imaging to a depth of 1000 μm in living brains by use of a Ti: Al_2O_3 regenerative amplifier,” Opt. Lett. 28, 1022-1024 (2003).

[62] S. Sakadzić, U. Demirbas, T.R. Mempel, A. Moore, S. Ruvinskaya, D.A. Boas, A. Sennaroglu, F.X. Kaertner, and J.G. Fujimoto, “Multi-photon microscopy with a low-cost and highly efficient Cr:licaf laser,” Opt. Express 16, 20848-20863 (2008).

[63] D. Kobat, M. E. Durst, N. Nishimura, A. W. Wong, C. B. Schaffer, and C. Xu, “Deep tissue multiphoton microscopy using longer wavelength excitation,” Opt. Express 17, 13355 (2009).

[64] S. –H. Chia, T. –M. Liu, A. A. Ivanov, A. B. Fedotov, A. M. Zheltikov, M. –R. Tsai, M. –C. Chan, C. –H. Yu, and C. –K. Sun, “A sub-100 fs self-starting Cr:forsterite laser generating 1.4 W output power” Opt. Express 18, 24085 (2010).

[65] X. Liu, C. Xu, W. H. Knox, J. K. Chandalia, B. J. Eggleton, S. G. Kosinski, and R. S. Windler, “Soliton self-frequency shift in a short tapered air-silica microstructure fiber,” Opt. Lett. 26, 358 (2001).

[66] I. G. Cormack, D. T. Reid, W. J. Wadsworth, J. C. Knight, and P. S. J. Russell, “Observation of soliton self-frequency shift in photonic crystal fibre,” Electron. Lett. 38, 167 (2002).

[67] L. Rishoj, G. Prabhakar, J. Demas, and S. Ramachandran, “30 nJ, ~50 fs all-fiber source at 1300 nm using soliton shifting in LMA HOM fiber,” Conference on Lasers and Electro-Optics (Optical Society of America, 2016), paper STh3O.3.

[68] W. Liu, S. Chia, H. Chung, F. X. Kaertner, and G. Chang, "Energy scalable ultrafast fiber laser sources tunable in 1030-1200 nm for multiphoton microscopy," in Lasers Congress 2016 (ASSL, LSC, LAC), OSA Technical Digest (online) (Optical Society of America, 2016), paper ATh1A.5.

[69] W. R. Zipfel, R. M. Williams, and W. W. Webb, “Nonlinear magic: multiphoton microscopy in the biosciences,” Nat. Biotechnol. 21(11), 1369–1377 (2003).

[70] C. Xu and F. W. Wise, “Recent advances in fiber lasers for nonlinear microscopy,” Nat. Photonics 7(11), 875–882 (2013).

[71] X. Gao, W. Zong, B. Chen, J. Zhang, C. Li, Y. Liu, A. Wang, Y. Song, and Z. Zhang, “Core-pumped femtosecond Nd:fiber laser at 910 and 935 nm,” Opt. Lett. 39(15), 4404–4407 (2014).

[72] R. Hegenbarth, A. Steinmann, S. Sarkisov, and H. Giessen, “Milliwatt-level mid-infrared (10.5-16.5 μm) difference frequency generation with a femtosecond dual-signal-wavelength optical parametric oscillator,” Opt. Lett. 37(17), 3513–3515 (2012).

[73] M. Hajialamdari and D. Strickland, “Tunable mid-infrared source from an ultrafast two-color Yb:fiber chirpedpulse amplifier,” Opt. Lett. 37(17), 3570–3572 (2012).

[74] X. Liu, C. Xu, W. H. Knox, J. K. Chandalia, B. J. Eggleton, S. G. Kosinski, and R. S. Windeler, “Soliton selffrequency shift in a short tapered air-silica microstructure fiber,” Opt. Lett. 26(6), 358–360 (2001).

[75] Alaa M. Al-kadry and Martin Rochette, "Mid-infrared sources based on the soliton self-frequency shift," J. Opt. Soc. Am. B 29, 1347-1355 (2012).

[76] Y. Yao and Wayne H. Knox, "Broadly tunable femtosecond mid-infrared source based on dual photonic crystal fibers," Opt. Express 21, 26612-26619 (2013).

[77] Y. Yao and Wayne H. Knox, "Difference frequency generation of femtosecond mid infrared pulses employing intense Stokes pulses excitation in a photonic crystal fiber," Opt. Express 20, 25275-25283 (2012).

[78] A. Ruehl, A. Gambetta, I. Hartl, M. E. Fermann, K. S. E. Eikema, and M. Marangoni, “Widely-tunable mid-infrared frequency comb source based on difference frequency generation,” Opt. Lett. 37(12), 2232–2234 (2012).

[79] B. Chen, T. Jiang, W. Zong, L. Chen, Z. Zhang, and A. Wang, “910nm femtosecond Nd-doped fiber laser for in vivo two-photon microscopic imaging,” Opt. Express 24(15), 16544–16549 (2016).

[80] http://webbook.nist.gov/cgi/cbook.cgi?ID=C7732185&Type=IR-SPEC&Index=1#IR-SPEC

[81] http://webbook.nist.gov/cgi/cbook.cgi?ID=C124389&Type=IR-SPEC&Index=1#IR-SPEC

[82] Y. Yao and W. H. Knox, “Fiber laser driven dual photonic crystal fiber femtosecond mid-infrared source tunable in the range of 4.2 to 9 μm,” Proc. SPIE 8964, 89640Q (2014).

Appendix

Table A. 1 Coupling lenses utilized in LMA-8 fiber coupling

Coupling Lens	Coupling efficiency
C240TME-B f = 8 mm NA = 0.5	61.6%
C1711TMD-B f= 6.2 mm NA = 0.3	49.7%
C220TME-B f = 11 mm NA = 0.25	76.1%

Table A. 2 Coupling lenses utilized in LMA-PM-10 fiber coupling

Coupling Lens	Coupling efficiency	Coupling efficiency after adjusting polarization
C220TME-B f = 11 mm NA = 0.25	64.3%	60.5%
C560TME-B f= 13.86 mm NA = 0.18	69.6%	60.1%
C260TMD-B f = 15.29 mm NA = 0.16	67.4%	62.6%

Table A. 3 Summary of pre-amplifier of High power CPA system

Pump Current (mA)	Pump Power (mW)	Output power (mW)	Output after isolator (mW)
100	44.1	20.1	16.3
200	113	53.8	45
300	182	88.7	75
400	251	124	106
500	322	159	136
600	391	193	166
700	458	227	195
800	526	262	225
900	593	294	253
1000	657	322	278
1100	724	353	303
1200	778	379	328

Table A. 4 Summary of power amplifier of High power CPA system

TEC temperature (℃)	Pump Current (mA)	Pump Power (W)	Output Power (W)
48	500	0.2	0.117
48	1000	1.71	0.152
50	1500	3.20	0.585
49	2000	4.68	1.45
49	2500	6.14	2.39
49	3000	7.58	3.42
49	3500	9.01	4.44
49	4000	10.4	5.42
49	4500	11.8	6.38
46.93	5000	13.1	7.44
45	5500	14.4	8.44
45	6000	15.7	9.33
43.5	6500	17.0	10.3
42	7000	18.3	11.3
40	7500	19.5	12.3
39	8000	20.7	13.2
38	8500	21.8	14.0
36	9000	23.0	15.1
34	9500	24.1	16.0
32	10000	25.2	16.9
31	10500	26.1	17.8
29	11000	27.1	18.6
27	11500	28.0	19.4
27	12000	28.9	20.3